Co- and Post-seismic Deformation of the 1999 Chi-Chi Earthquake Revealed by Earth Observations

Marine Roger

Thesis submitted for the degree of
Doctor of Philosophy

School of Engineering
Newcastle University
Newcastle upon Tyne
United Kingdom

July 2021

Abstract

The Mw 7.6 Chi-Chi earthquake struck Central Western Taiwan in 1999. The rupture was complex with several dislocations along the 100-km long Chelungpu thrust fault. Revisiting this earthquake is a challenge, as the precision and coverage of the Earth observations available are quite poor, but it allows better understanding of regional fault properties. Furthermore, the topographic and vegetation coverage complexity of the area prevents coherent radar images. In this thesis, radar and optical images, and terrestrial geodetic measurements, were utilised to study the Chelungpu fault and more specifically the impact of the Chi-Chi earthquake.

First, five types of Earth observations were processed to investigate the co-seismic deformation. The Particle Swarm Optimization and Okada Inversion (PSOKINV) geodetic inversion package was used with the generalized Akaike's Bayesian Information Criterion (gABIC) to precisely determine the coseismic slip distribution and relative weighting of datasets. Differences in results using the data sets jointly or separately (e.g., under-estimation due to InSAR, inconsistencies in SPOT offsets, smoother slip distribution with gABIC weighting) are observable. Most of the energy was released in the northern part of the fault, where the strike veers toward the east, and mainly at depths of less than 4 km. The PSOKINV-gABIC approach is viable for the study of complicated cases such as the Chi-Chi earthquake (complex fault geometry and multi-source observations) and can substantially benefit the weight determination and physical (no overlap or gap) realism of the fault geometry.

Second, the post-seismic deformation of this event was observed using 20 years of time series from InSAR and GPS. Then, a model of the afterslip and viscoelastic relaxation was built. 11 years of ERS, 3 years of EnviSAT, 6 years of Sentinel-1A/B descending and 3 years of Sentinel-1A/B ascending images were processed using GAMMA-Remote Sensing software and atmospherically corrected using GACOS (Generic Atmospheric Correction Online Service for InSAR). Finally, InSAR time series were extracted and validated using GPS data. The modelling of the post-seismic deformation following the Chi-Chi earthquake was done using a power-law Burgers rheology to analyse the interplay between afterslip and viscoelastic flow. From the time series, a change in the ground displacement can be observed in 2004 showing a slow-down of afterslip deformation. The forward modelling of the post-seismic deformation showed that the maximum afterslip is observed on the southern part of the fault, on the decollement in depth (while the maximum slip was happening at shallow depth on the north section of the fault during the co-seismic deformation). Furthermore, the study of the strain enabled me to conclude that the interseismic phase has started over most of the area, most segments of the Chelungpu fault are now getting locked again. More data coverage and a longer monitoring of the Chelungpu fault will be needed to observe the entire earthquake cycle.

Acknowledgements

This work was funded by ESA-MOST DRAGON-4 project, grant number 32244. Part of the work was also supported by the UK NERC through the Centre for the Observation and Modelling of Earthquakes, Volcanoes and Tectonics (COMET, Ref.: come30001) and the LICS project (Ref. NE/K010794/1). An additional grant was obtained in 2019 enabling to realise a fieldtrip to Taiwan: The RGS-IBG Hong Kong research grant 2019.

First, I would like to express my sincere gratitude to my supervisors Prof. Peter Clarke, Prof. Zhenhong Li and Dr. Chen Yu and for their support, patience, advice and encouragement throughout the years of my thesis and that guided me to grow as a research scientist. Thank you for having faith in me. This thesis would not have been possible without your help and support. Their professional comments helping me to improve my scientific thinking, looking at the bigger picture and improve my scientific writing. They always kept a positive spirit and benevolent.

Thanks to all data providers. SPOT images were provided freely by Airbus Defence and Space. ERS, EnviSAT and Sentinel-1 images were provided freely by ESA's Sentinels Scientific Data Hub and ASF Alaska. GPS data and levelling were provided by National Taiwan University.

I would like to thank also the researchers that shared their modelling programs and helped with the use. A special thanks to Prof. James Moore for his time, explanation, positive mind and accessibility in running the postseismic model.

I would like to thank the entire Geospatial Engineering group at Newcastle University for making me feel at home in Newcastle even though Covid took us apart the last year. Dr. Ahmed Elsherif, Dr. Andreja Susnik, Dr. Achraf Koulali, James Goodyear, Martin Robertson, Dr. Nurten Akgun, Gauhar Meldekova, Chuang Song and many others for all the work related discussions but also for the good times, essential to go through the PhD (cycling to Tynemouth, playing tennis or Friday's evenings along the Tyne).

Special thanks to Dr. Katarina Vardic for the three years of laughter, relaxation times and motivation. Thanks to her advice, her perseverance. My time in Newcastle would have been completely different without her. I am thankful for meeting her and cannot wait to visit her and Vegard in Norway and Croatia. Another special thanks goes to my desk mate Leslee Davidson and her partner Nick which kindness and humour make it a pleasure to go to work each day. I enjoyed so much our Friday nights, leaving the PhDs in the office and enjoying the warmth of Newcastle. Also, a huge thanks for their help emptying my apartment while I was blocked in France due to Covid.

Finally, I reserve my most heartfelt appreciation and thanks for my family for their infinite support through my long years of studies and PhD. Thanks to my parents and grandparents that even thought they do not fully understand my passion for remote sensing, always supported me in my studies and pushed me to improve and keep going following my path, even if it was on another continent. To my brother Nicolas that always been an example of smartness, kindness and without whom my life would be completely different and finally, my cousin Alizée for her hard work and motivation to start a PhD.

Table of Contents

List of abbreviations

4D-Var ..... Four-dimensional variational

ABIC ..... Akaike's Bayesian Information Criterion

AEM ..... Atmospheric Estimation Model

ALOS ..... Advanced Land Observation Satellite

APS ..... Atmospheric Phase Screen

ASF ..... Alaska Satellite Facility

ASTER ..... Advanced Spaceborne Thermal Emission and Reflection Radiometer

CGS ..... Central Geological Survey

CNR-IREA .. Instituto per il Rilevamento Elettromagnetico dello Ambiente

COSI-Corr ... Co-registration of Optically Sensed Images and Correlation

CRAF ..... Chuoshui River Alluvial Fan

CSC ..... Coulomb Stress Change

CTF ..... Chelungpu Thrust Fault

CWB ..... Central Weather Bureau

DEM ..... Digital Elevation Model

DInSAR ..... Differential SAR Interferometry

DS ..... Distributed Scatterers

ECMWF ..... European Center for Medium-Range Weather Forecast

ENVI ..... Environment for Visualizing Images

EnviSAT ..... ENVIronment SATellite

EO ..... Earth Observation

EOF ..... Precise/restituted Orbit Files

ERS ..... European Remote-Sensing

ESA ..... European Space Agency

E-W-N-S ..... East-West-North-South

FFT ..... Fast Fourier Transformation

FFTW ..... Fastest Fourier Transform in the West

gABIC ..... Generalized Akaike's Bayesian Information Criterion

GACOS ..... Generic Atmospheric Correction Online Service

GBSAR ..... Ground-Based interferometric SAR

GCP ..... Ground Control Point

GDEM ..... Global Digital Elevation Model

GLONASS ... GLObal Navigation Satellite System

GNSS ..... Global Navigation Satellite System

GPS ..... Global Positioning System

HRES ..... High-RESolution

IDL ..... Interactive Data Language

IESAS ..... Institute of Earth Sciences, Academia Sinica

IGN ..... Institut National de l'Information Géographique et Forestière

InSAR ..... Interferometric Synthetic Aperture Radar

ITD ..... Iterative Tropospheric Decomposition

ITRF ..... International Terrestrial Reference Frame

Landsat ..... Land Satellite

LVF ..... Longitudinal Valley Fault

LOS ..... Line Of Sight

MCF ..... Minimum Cost Flow

MICMAC .... Multi-Images Correspondances par Méthodes Automatiques de Corrélation

MOEA ..... Ministry Of Economic Affairs

MOI ..... Ministry Of Interior

M-PSO ..... Multi-peak Particle Swarm Optimization

PNT ..... Position/Navigation/Time

PSHA ..... Probabilistic Seismic Hazard Assessment

PS ..... Persistent Scatterers

PSI ..... Persistent Scatterers Interferometry

PSOKINV ... Particle Swarm Optimization and Okada Inversion package

RGS-IBG .... Royal Geographical Society-Institute of British Geographers

RMS ..... Root Mean Square

SAR ..... Synthetic Aperture Radar

SBAS ..... Small BAseline Subsets

SLC ..... Single Look Complex

SNAP ..... Sentinel Application Platform

SNAPHU .... Statistical-cost, Network-flow Algorithm for Phase Unwrapping

SNR ..... Signal-To-Noise Ratio

SPOT ..... Satellite Pour l'Observation de la Terre

SRCMOD .... Earthquake Source Model Database

SRTM ..... Shuttle Radar Topography Mission

STD ..... Standard Deviation

THSR ..... Taiwan High Speed Railway

TP ..... Tie Point

TS ..... Time Series

TWD67 ..... Transverse Mercator Two-degree Grid 1967

USA ..... United States of America

USGS ..... United States Geological Survey

WGS84 ..... World Geodetic System 1984

ZTD ..... Zenith Tropospheric Delays

List of Figures

List of Tables

Chapter 1

Introduction

1.1 Background

Earthquake hazard is one of the major natural disasters. An earthquake hazard includes a seismic event that leads to human, economic and social damages and losses. The mitigation of these damages is done through an improvement of hazard assessment and disaster management which need a precise knowledge of physical processes of major active faults. Earthquake cycle is the general term used to encompass the main processes around the deformation of the solid Earth due to earthquakes. In this thesis, a focus will be on the coseismic phase, deformation of the event itself, followed by the study of the transient period corresponding to the postseismic phase.

Several geodetic techniques exist to study the different phases and processes involving from only millimeters of relative displacement on either side of a fault to tens of meters of displacement in a few seconds. Earth Observations for surface displacement (EO) (such as those from Interferometric Synthetic Aperture Radar (InSAR), Global Navigation Satellite System (GNSS), and optical satellite images) combined with other types of information (such as levelling, or seismology) can be used as inputs in geophysical models. InSAR and GNSS can detect several magnitudes of surface displacement. Optical imagery using the pixel offset technique is mainly used to study large offsets.

Large developments were made and are still improving in EO regarding accuracy and processing methodologies. Geophysical inverse models are used to better understand and visualize these processes. For coseismic and postseismic models, usually an elastic medium in a half-space is used to determine the geometry of the fault (Okada (1985)) and slip distribution. Other models are used to study the rheology such as the viscoelastic process during the postseismic phase. A combination of these processes gives information about the position and quantity of strain building up in the crust. Therefore, the aim of this thesis is to take advantage of the multitude of EO available nowadays (in majority with free access), build a methodology to use them jointly in models and study the different phases of deformation corresponding

to earthquake cycle. In this thesis, I will focus on the M_w 7.6 Chi-Chi earthquake, Taiwan, of 1999.

1.1.1 Earthquake cycle

The deformation of the Earth crust under tectonic strength is a phenomenon impacting a large volume of rock. The deformation is present on the surface but mainly at a deeper level.

The Earth's lithosphere is divided into approximately 15 major tectonic plates (`geology.com/plate-tectonics.shtml`) that move in relation to each other. Four main layers compose the Earth: crust, mantle, inner and outer core. The moving part of the Earth is rigid and defined by the lithosphere (crust and upper mantle), situated on top of the asthenosphere. The lithosphere is composed of rocks behaving elastically and its thickness varies from about 50 km in active areas and more than 100 km in stable continental parts. The asthenosphere is the ductile part of the upper mantle.

Reid (1910) explained the theory of elastic rebound as a basis of the earthquake cycle: a steady accumulation of stress leading to a sudden slip of the fault. The deformation is said to be elastic (at least on the upper part of the lithosphere) as rocks return to their original shape when the force applied is removed. The strained rocks are hence catching up with the far field rocks.

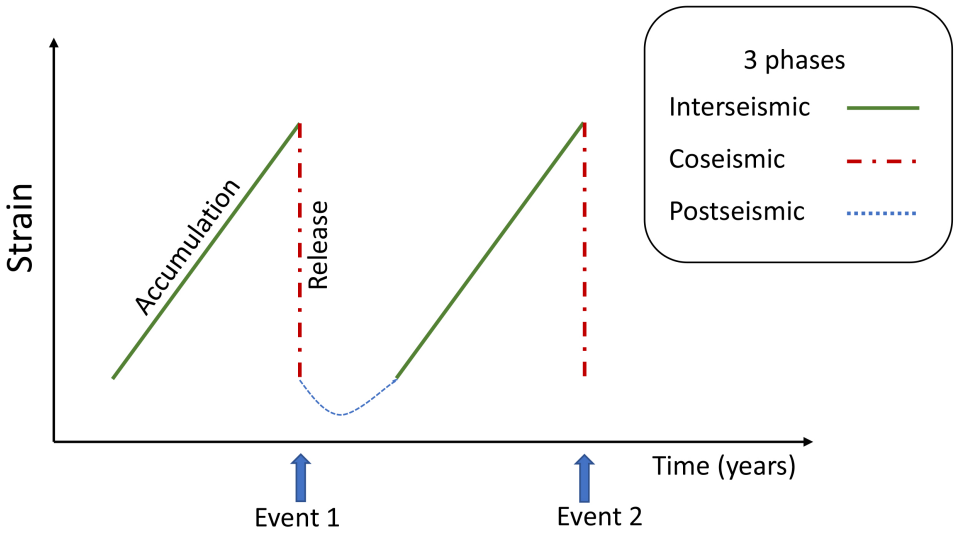

Figure 1.1: Simplified overview of the earthquake cycle: repetition of a strain accumulation period and a release of energy along a fault. The green lines represent interseismic phases; coseismic ruptures are showed by red dashed lines and blue dotted lines represent postseismic deformation.

The earthquake cycle is the repetition of an event in one area consisting of strain accumulation and a release of the energy. However, it is not always periodic as other

phenomenons are disturbing the fault. Three periods compose the earthquake cycle (Figure 1.1): interseismic, coseismic and postseismic.

The interseismic deformation (Elliott *et al.* (2020)) can last for several years or decades and occurs between two events. During this period, a slow accumulation of elastic strain occurs where a fault is locked due to friction, and strain builds up within the rocks. Indeed, a fault is a fracture in the crust across which blocks of rock (presenting asperities) are moving in different directions. In the context of tectonic plates at an extension zone, points next to the fault are blocked and accumulate a slip deficit in comparison to the rest in comparison to the rest of the plate. The term *elastic strain* is used to imply that the materials deformed have a memory. After the rupture, the materials will return to their original shape.

The earthquake is defined by a sudden rupture or a release of strain happening when the shear stress acting on the fault surface exceeds the force of friction. The fault is then able to slip and release the stored elastic potential energy. The rocks near the fault, that accumulated strain during a long period, can finally slide back to a less-strained state. The rupture starts when the stress due to the accumulation of strain during the interseismic phase overcomes the friction resisting it. This is the coseismic phase that usually last from a few seconds to minutes.

Finally, the postseismic deformation is a transient period which diminishes back to the long-term loading period known as the interseismic period (Bürgmann (2018)). The postseismic deformation can last from days to years for large earthquakes. It is due to a time-dependent relaxation of the stresses induced by the coseismic rupture. Three main processes are explaining this deformation period with different mechanisms at both temporal and spatial scales. Usually, they are to be combined to fully describe the postseismic deformation.

- Afterslip (Bürgmann *et al.* (2002)) is a continuous, aseismic slip surrounding the coseismic rupture area happening usually during a few years following the event.

- Viscoelastic relaxation is usually lasting longer than the afterslip and is covering a larger area. This deformation is dependent on the rheology of the fault area (Ryder *et al.* (2014)). It is the gradual flow of light materials due to the coseismic stress. The first $\sim$ 15 km of the continental crust is acting as an elastic solid. However, beneath this limit, materials move as fluids depending on the viscosity and hence the temperature. For large earthquakes, afterslip and viscoelastic flow mechanically interplay with each other. Mechanical coupling need to be considered while studying long postseismic deformation.

- Poroelastic rebound deformation (Fialko (2004)) are due to changes in the drainage conditions in the upper crust. The release of strain during the coseismic slip produces a change in pore fluid pressure in the brittle upper crust. (This deformation is not analysed in our study as its contribution is small in

comparison to afterslip and viscoelastic relaxation (about 10% of the observed amplitude according to Rousset *et al.* (2012))).

From plate velocity models, strain accumulated at plate boundaries can be estimated. However, earthquakes only account for about a third of fault slip occurring along plate boundaries. Even though, earthquakes are one of the main phenomena accommodating plate motion, other processes exist such as aseismic slip, fault creep (where the frictional forces are almost non-existent, for instance San Andreas fault) or slow-slip events not detectable with seismometers but now detectable thanks to the advances in geodetic measurements. Furthermore, part of the stress can be released during the interseismic period by aseismic slip or by small earthquakes. Their monitoring enables to detect which parts of faults are locked and accumulating more stress.

1.1.2 Earth observations for surface displacement

The increase in the number of EO satellites during the last 10-20 years, and the improvements of their characteristics (data coverage, revisit time, resolution, precision) and processing softwares have largely expanded the use of EO data in characterising earthquake deformation as well as studying other phenomena, especially thanks to the open data policy. In the radar domain, the launch of the Sentinel-1 constellation brought a clear improvement of precision and quality of satellite measurements. Before the use of EO satellites, seismological measurements and field observations were the main data used to constrain earthquake models. The combination of the multitude of EO data sets available nowadays is enabling to better constrain shallow continental earthquake ruptures and their complementarity is making the joint modelling easier to set up and more efficient.

Earthquake cycle comprises displacements of only millimeters, occurring over decades and large areas, as well as sudden release of energy generating meters of displacements over a few seconds. The variety of gradient of displacement to detect are requiring accurate and specific systems. InSAR and GNSS are applicable to study any phase of the earthquake cycle and optical imagery is predominantly useful for large displacement (such as offset happening during the coseismic phase).

GNSS data have a high temporal resolution and an accuracy of less than 1 mm/yr useful to study slow deformation such as the postseismic phase. It can also be used to study fast deformation such as the coseismic phase; however their spatial distribution is sparse. InSAR data have a high spatial density and sub-cm precision but a low temporal sampling rate depending on the satellite (for instance, 6 days for Sentinel-1 satellites but 35 days for ERS). Also, C-band (ERS, EnviSAT, Sentinel-1) and L-band (ALOS-1 & 2) satellites are available giving access to a variety of frequencies. Finally, SPOT images have a similar spatial density to SAR images, but can often provide useful measurements despite vegetation (where SAR images lose coherence) and at higher density than a pixel offset map estimated from the SAR amplitude would give.

The use of both optical and radar images is particularly interesting in an area as complex as Taiwan presenting dense vegetation, steep areas and extreme weather. InSAR and optical offsets are efficient to study strain rates over large areas. Small deformation signals over long wavelengths can be studied through time series. A continuity in the data is important and can be improved by using GNSS (data every few minutes or hours for GNSS against a minimum of 6 days for Sentinel-1). Using only one type of EO is unlikely to correctly constrain the geophysical process studied.

It is fundamental to precisely determine the location, depth and magnitude of an event, but also to identify which portions of the fault ruptured and to identify the portions that might break in the future.

1.2 Motivation

The Central Western part of Taiwan is an area with complex geological settings (see Chapter 2). The study of past seismic events and the monitoring of the present deformation is important to better understand the seismic hazard of the area. Especially for active faults such as the Chelungpu one which has a high probability to generate earthquakes with high risk for the population. Figure 1.2 presents a map of the active faults deforming Central Western Taiwan.

Several studies were conducted over Taiwan using different data sets (remote sensing, teleseismic or seismic data) giving a detailed background of Taiwan and its western side (Chen *et al.* (2017); Ching *et al.* (2011); Shyu *et al.* (2005)) as well as investigating the coseismic and postseismic displacements of the Chelungpu fault (Johnson & Segall (2004); Pathier *et al.* (2003); Tang *et al.* (2019)). However, the complexity of the area (topography and dense vegetation covering the hanging-wall which was the location of the main deformation) has left a lot of improvements necessary to precisely understand the tectonic of Central Western Taiwan. Over the past 20 years, several papers have been published on the modelling of the Chi-Chi earthquake, each of them focusing on specific aspects, using specific techniques and methods. Johnson & Segall (2004); Loevenbruck *et al.* (2001) & Zhang *et al.* (2008) inverted GPS and/or InSAR data to build dislocation models. Furthermore, studies based on optical images (Dominguez *et al.* (2003); Kuo *et al.* (2014)) have helped to understand the hanging-wall motion. However, no studies joined all these EO data to study the fault geometry and slip distribution. Moreover, very few papers were written during the last decade. Since then, many improvements were done on the correction of interferograms (especially atmospheric correction and phase closure for unwrapping errors) and in inversion packages. Therefore, the understanding of the Chelungpu fault can benefit from these improved techniques. Finally, few papers have been studying the postseismic phase of this specific event and more generally, earthquake cycle studies are quite rare. Thanks to the fact that we possess data from about 5 years before the event (data studied in the literature) to 20 years after, a large investigation is now possible.

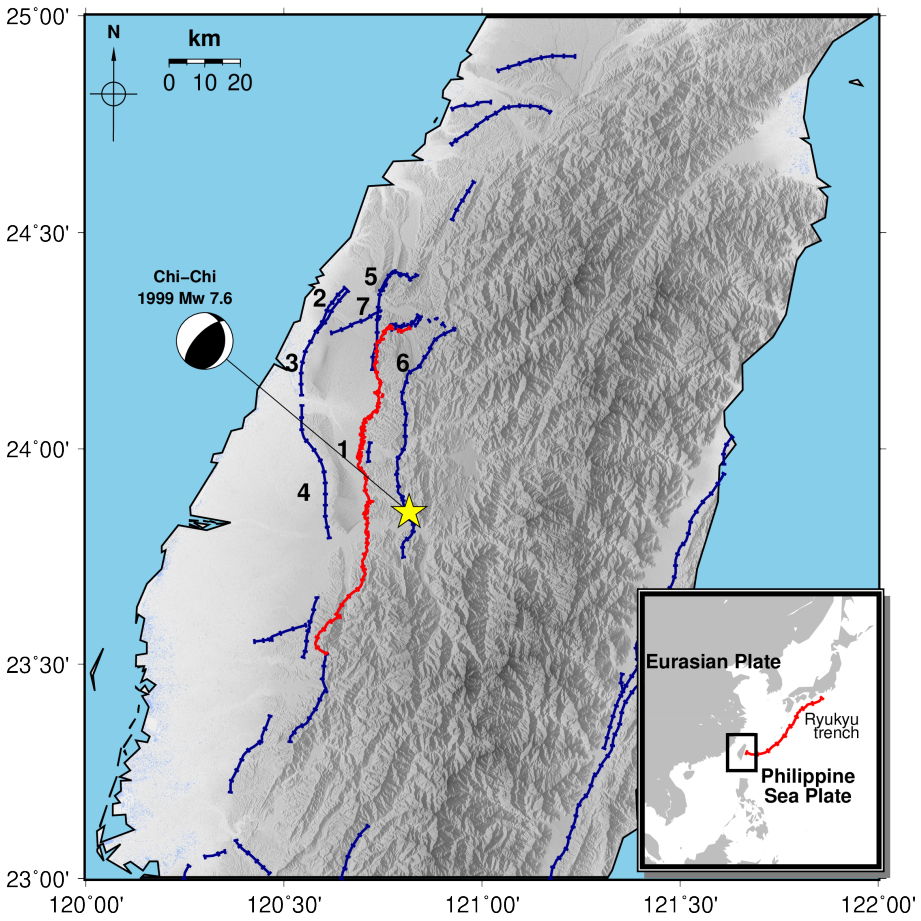

Figure 1.2: Taiwan map presenting the main faults of Central Western Taiwan (1-Chelungpu fault, 2-Tiehchanshan fault, 3-Tachia fault, 4-Changhua fault, 5-Sanyi fault, 6-Tamaopu-Shuangtung fault, 7-Tuntzuchiao fault). (Source: National Taiwan university.)

The interest of this thesis work lies in the combination of EO abilities to measure ground displacement and the tectonic uncertainties still present in Taiwan. The island is constantly under seismic risk and a rapid expansion of the population and human constructions is present over Taiwan. One of the main difficulty of EO based modelling is depending on the depth of the event. If the earthquake's rupture is deep, the surface displacement at the surface will be small which will complicate the analysis and inform mainly on the ruptured parts within the first kilometers of the lithosphere. However, shallow events have a direct influence on man and his constructions. Even though it is not the simplest case to study due to the complexity of the terrain and some restrictions of EO, it is essential to narrow down our knowledge of the deformation for hazard assessment. The main tectonic questions that remain unclear are the link between the different faults of the area, the impact of other mechanisms (such as poroelasticity) on stress accumulation and the precise geometry of the decollement in depth.

1.3 Aims and Objectives of the Thesis

The overall aim of this thesis is to focus the research on a well-known event that has a well-documented background in terms of geology and tectonics. The focus is on improving the understanding of the deformation of the Chelungpu fault, active fault situated in a densely populated area, and on improving the general knowledge on earthquake cycle phases by using EO. The aim is not to discuss consequences in terms of natural hazard assessment. However, it can help later studies focusing on earthquake cycle and hazard assessment. EO derived measurements are used as inputs for geophysical models for slip and fault geometry determination as well as rheology determination for viscoelastic processes.

The main objectives are summarized as follows:

O1. Develop a methodology for coseismic modelling integrating multiple data sets.
Integration of several types of EO (GPS, InSAR, optical images and levelling) to overcome topography and atmospheric conditions as well as to constrain the model. The goal is to show the efficiency of EO in constraining models and the possibility to use them jointly by estimating precisely relative weights.

O2. Model afterslip and viscoelastic relaxation induced by the Chi-Chi earthquake.
20 years after the earthquake, the island is monitored by a dense network of GPS stations and SAR satellites with open access. However, a continuity since the event is rare. The objective is to build a forward model to analyse the afterslip and viscoelastic flow mechanisms running the postseismic deformation and to estimate the cumulative strain in the lower-crust. The second goal of this objective is to analyse time series from GPS and InSAR to detect any modification of the postseismic deformation and estimate if the interseismic phase started again.

03. Analysis of the deformation of Central Western Taiwan during the Chi-Chi event of 1999 and since using Earth Observations.
The purpose is to combine the information extracted from the study of the co- and post-seismic phases combined with the knowledge of the interseismic phase obtained in the literature to get insights of the full earthquake cycle of this specific event. Specifically, to improve our knowledge of the active faults in Taiwan, and shallow crustal tectonics. An improved study of this earthquake will allow better understanding of regional fault properties and help monitor seismic hazard in an area where the demography is increasing and the cities expanding.

To fulfill the research objectives, the following questions will be addressed:

1. Is joint inversion of several Earth observations realistic? Will uncertainties of

each data set bias the joint inversion more than it is constraining the model and increasing the precision of a GPS-only model?

2. What can we learn from applying new techniques to events that happened decades ago?

3. Should postseismic mechanisms (afterslip and viscoelastic relaxation) be considered mechanically coupled in the case of the Chi-Chi earthquake?

4. From a time series analysis of the 20 years of deformation, can a return to the pre-earthquake rate be detected using EO, meaning a transition from postseismic to interseismic deformation?

1.4 Outline of the Thesis

The thesis is structured as follows:

Chapter 2 focuses on the deformation of Central Western Taiwan.
General geodynamic information about Taiwan will be discussed followed by a literature review of the Chi-Chi earthquake. Main coseismic studies and models using different data sets will be presented. Knowledge about the pre-earthquake deformation will be described as well as postseismic studies.

Chapter 3 introduces the main data and techniques used in this thesis.
SAR and InSAR principles will be described as well as major corrections required and time series analysis technique. Then, optical imagery will be presented based on SPOT imagery and sub-pixel correlation. Finally, GNSS system will be outlined.

Chapter 4 is concerned with the 1999 M_w 7.6 Chi-Chi earthquake in Taiwan.
Development of a methodology to jointly invert five EO with precise estimation of relative weights in order to take into account the strength and weaknesses of each data as well as the complexity of the topography. The fault geometry, slip distribution and seismic hazard are investigated. This work was published in Remote Sensing (Roger *et al.* (2020)).

Chapter 5 analyses the 20 years of postseismic deformation following the Chi-Chi earthquake.
20 years of deformation using InSAR and GPS time series will be analysed in order to determine the current state of the deformation. Modelling of the afterslip and viscoelastic relaxation will be realised using a forward model based on a power-law Burgers rheology.

Chapter 6 highlights the main contributions and conclusions of this thesis.

Chapter 2

Deformation in Central Western Taiwan

In the few seconds of shaking that lasted the Chi-Chi earthquake, thousands of people (over the 2.5 millions people living in the area of the Chelungpu fault) were killed or injured and buildings destroyed. 20 years after the event, researchers are still trying to understand precisely how the rupture happened and how the ground is deforming since then. Earthquake recordings are showing tens of disasters in the last decades with similar impact on the population all over the globe. A large quantity of earthquakes happen on continental grounds and sometimes on faults not previously mapped or with underestimated hazards. Assessing seismic hazard is challenging; continental earthquake study is focusing on one event and one fault, but earthquakes rarely strike the same area in less than decades or hundred years. In addition to the specific event deformation, plate boundary deformation is wide and complex, and other active faults are deforming in neighbouring areas. Furthermore, in contrast to volcanoes that usually show deformation prior an eruption, earthquakes usually occur without warning and pre-deformation.

Until now, seismic hazard is mainly assessed using Probabilistic Seismic Hazard Assessment (PSHA), method estimating the level of ground motion with the likelihood of exceedance for specific location and period based on past events (Reiter (1991); Roselli *et al.* (2017)). Therefore, recent techniques were designed based on ground deformation measurements such as GNSS or InSAR to study strain rate between earthquakes. The study of zones of release or accumulation of strain energy with sufficient accuracy by building models describing spatially and temporally the deformation of faults, enables to draw some estimations of area more likely to rupture in the future. GNSS and InSAR are the main technologies used nowadays to measure deformation at fault zones. GNSS networks have expanded significantly in the last decades even though it is still often insufficient to detect slow accumulation of strain or creeping due to spatial resolution. Similarly, InSAR can measure deformation with millimeter accuracy and with high spatial resolution. The combination of several interferograms is enabling to estimate tectonic strain (Hussain

et al. (2018)).

Several studies already used InSAR and GPS to study the tectonic of Taiwan (see Sections 2.2.1 to 2.2.3). Even though the techniques have some limitations (in addition to applying them on a complex topography such as Taiwan), the goal of this thesis is to show that Earth Observations (EO) are powerful data sets to study earthquake cycle deformations. Based on the knowledge of this area, techniques will be tested in the next chapters and analysis of the past and present deformation using EO will bring knowledge on the deformation of the Chelungpu fault and its surroundings.

The monitoring and analysis of the displacement is essential for the understanding of the tectonic (from collision and mountain formation to seismic event) but also for the estimation of natural hazard risk for the millions of people living on the island. In this chapter, a presentation of the geodynamic context of Taiwan will be introduced, followed by a description of the different phases of deformation of Central Western Taiwan, focusing on the Chelungpu fault and the Chi-Chi earthquake. The main studies available in the literature will be presented as well as research gaps remaining.

2.1 Tectonic background of Taiwan

Taiwan island, situated at the South-East of China, is the emerged part of an orogen formed by the collision (that started 3 million years ago (Suppe (1984))) between the Eurasian plate and the Philippine Sea plate (Ching *et al.* (2011)) entering in convergence at a rate of 82 mm/yr with an orientation of 310° (Chen *et al.* (2017)). Two subductions are consuming the island (see Figure 2.1): at the south, the oceanic crust (Eurasian plate) goes beneath the Luzon volcanic arc (Philippine sea plate) in the east direction at the Manila trench, and the Philippine Sea plate subducts towards the north near the Ryukyu trench at the east of the island. This subduction leads to the Ryukyu volcanic arc and the opening of the Okinawa basin. The convergence speed was estimated thanks to GPS measurements between the island of Lanhsu (South-East of the island on the Philippine Sea plate) and the one of Penghu (at the east, on the Eurasian plate) (Yu *et al.* (1997)). It is one of the faster convergence rate on the planet creating this complex tectonic system. Different deformations with high amplitude and several modes are deforming the island from earthquake to the formation of mountain range (Chamot-Rooke & Le Pichon (1999); Shyu *et al.* (2005); Yu *et al.* (1999)). The collision produces a fold and thrust belt in western Taiwan in which a series of thrust faults are deforming continental margin sediments (Lee *et al.* (2014)).

Taiwan is separated in six northeast-trending physiographic regions separated by major faults (Figure 2.1). Starting at the west by the Coastal Plain where a shortening is happening and with more deformation in the south than the north, and the Western Foothills at its east. These regions compose the Chinese continental margin with low altitude and light vegetation. Thus, it is the most documented

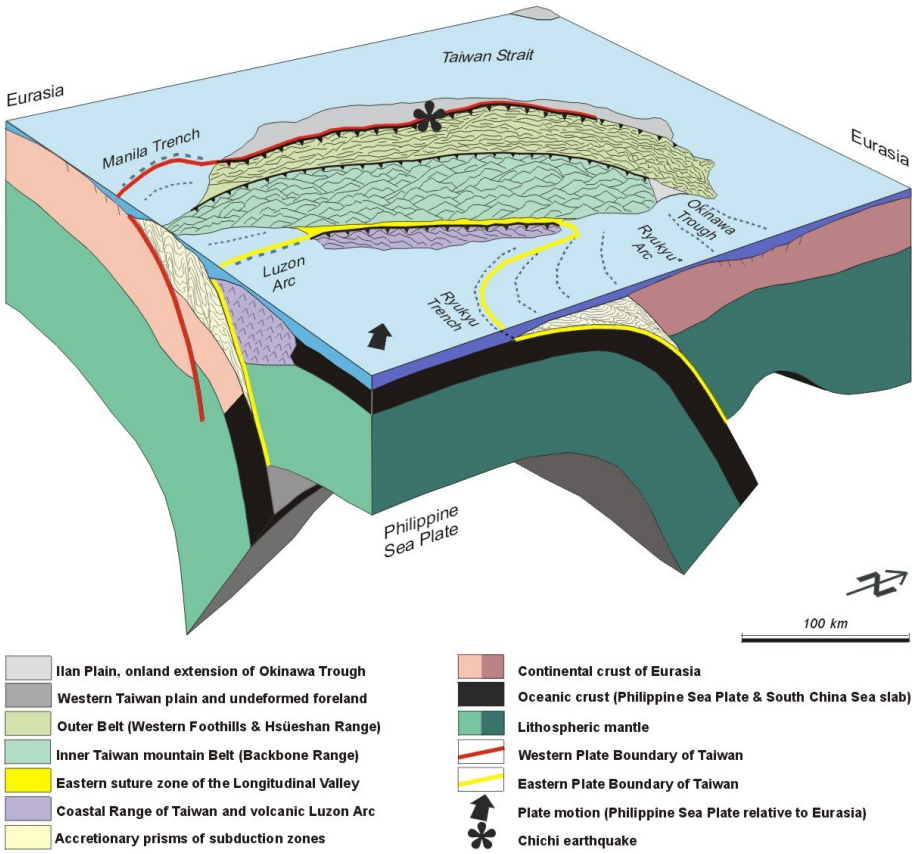

Figure 2.1: Schematic block-diagram describing the tectonic (lithosphere) situation of Taiwan island. Description of the colors above corresponding to major units and tectonic boundaries (extracted from Angelier *et al.* (2001)).

area in the literature. The Central Range and the Hsueshan Range are mountainous areas situated in the middle of the island. Over the Central Chain, an uplift of about 2 cm/year is happening with an E-W extension (Yu *et al.* (1997)). At the east, the Longitudinal Valley is present, where most of the deformation is happening each year and partly aseismically, and located on the Longitudinal Valley Fault (LVF, one of the most active fault in Taiwan). It is described as the junction area between the two tectonic plates. Finally, the Coastal Range at the East (Peyret *et al.* (2011)), narrow region with a length of 135 km and a maximum width of 15 km, it is parallel to the LVF.

Taiwan is a high-risk seismic area located along the Pacific seismic belt constantly threatened by earthquakes (see Figure 2.2), thousands are felt by the population each year, mainly located on the east coast and for shallower depth than 50 km. Two areas are particularly deforming and composed of active faults (mainly oriented EW to SW-NE): the Longitudinal Valley at the east and the foothills at the west. Hundreds of earthquakes were categorized as destructive due to the large number of

casualties (lives and constructions) and with magnitude greater than 5. In Central Western Taiwan occurred the earthquake Schinchiku-Taichu in 1935 ($M_l = 7.1$ and focal depth 5 km, source CWB: `http://www.cwb.gov.tw/`) and the major and most destructive inland earthquake of the 20^{th} century being the Chi-Chi event ($M_l = 7.3$ and focal depth 8 km, source CWB). Several other large events struck the island in the last century with a magnitude above 7 (Ng *et al.* (2009)) such as Meishan earthquake in 1906 (M_l= 7.1, focal depth 6 km) and Chungpu event in 1941 (M_l = 7.1, focal depth 12 km). Figure 2.2 based on seismic data from CWB covering 1998 to 2020 shows the quantity of earthquakes striking the island. The Taiwanese seismicity corresponds to a major portion of the annual seismicity of the entire globe, earthquakes of magnitude over 5 often strike the island and with epicentre depth beneath 25 km.

2.2 Earthquake Cycle Deformation

A brief description of the tectonic context of Taiwan and its main tectonic structures was presented in the previous section. The focus will now be on the deformation of the Central Western region, focusing on the Chelungpu fault and the consequences of the Chi-Chi earthquake.

The Chi-Chi earthquake, due to the reactivation of the Chelungpu fault which ruptured over 100 km, is the most destructive event happening in Taiwan in the last century. Studies (Johnson & Segall (2004); Loevenbruck *et al.* (2001)) showed that the main displacement happened in the north of the fault while the interseismic deformation was mainly in the south section of the fault and in the foothills, mainly happening aseismically on major discontinuities. The western part of Taiwan is where the largest cities are located such as Taichung in the middle of the study area. For this purpose, I am focusing the work on using the variety of EO and long period of data available to better understand the deformation in this area of high demography.

As previously presented, deformation due to earthquakes can be decomposed in two main periods: the coseismic phase corresponding to the event itself and the interseismic period (period between two events). During this period, an accumulation of tectonic stress is happening that can be suddenly released during the coseismic phase or released aseismically (the stress is liberated irregularly and only on certain zones of the fault). The spatio-temporal behaviour of a fault is important to analyse and to detect the accumulation areas in order to get an idea of which zones will potentially rupture in the near future. The monitoring of interseismic deformation is essential for the determination of tectonic stress and thus the seismic hazard estimation.

The next sections will present the main studies analysing the pre-, co- and post-seismic phases of the Chi-Chi earthquake detailing their models, conclusions and questions still open to discussion.

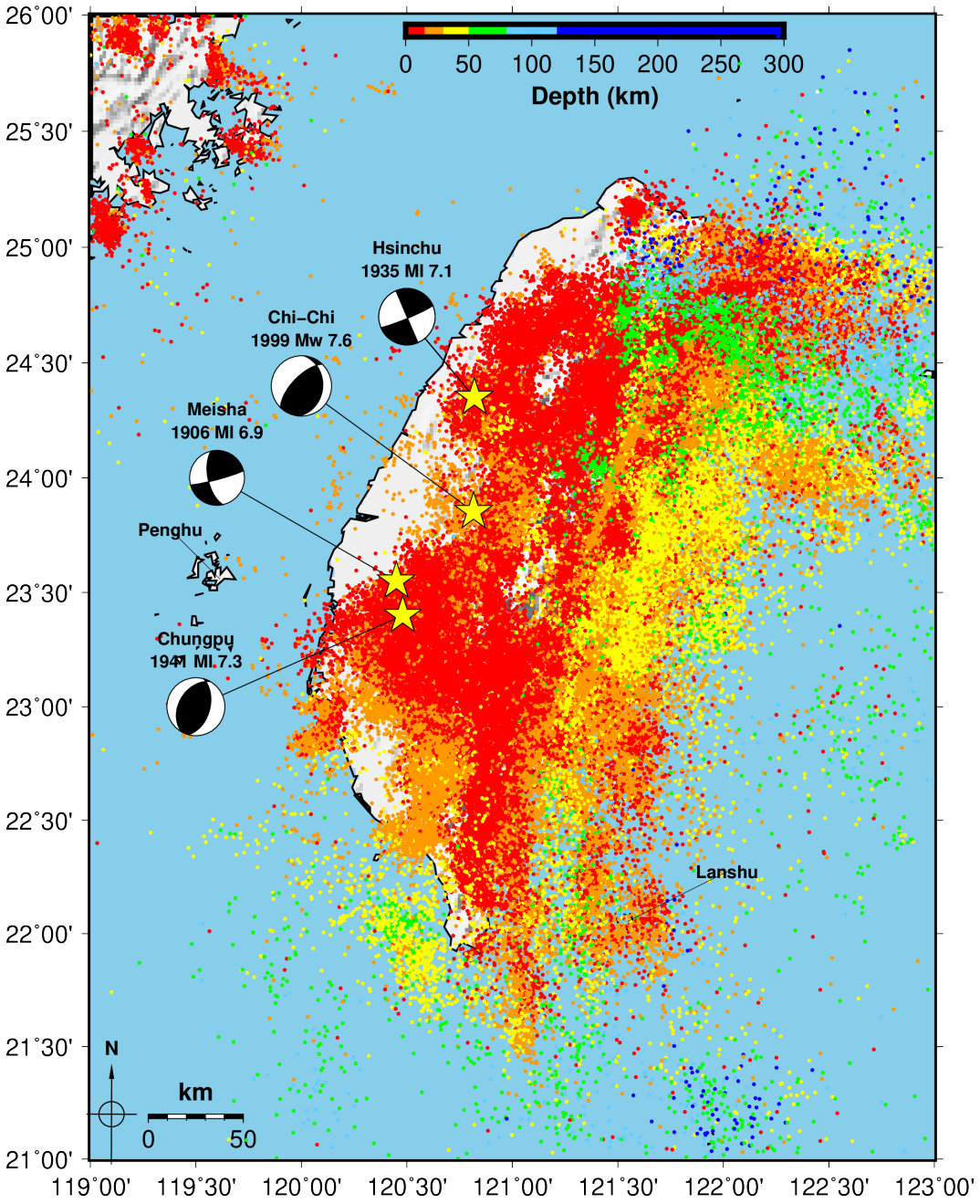

Figure 2.2: Seismicity distribution (for magnitude over 3) over Taiwan from 1998 to 2020. The localisation of each epicentre is shown by a dot and recorded by CWB. Colours are explained in the legend and corresponding to the depth. (For reading purposes, the magnitude is no shown by circle sizes.)

2.2.1 Pre-seismic deformation

The interseismic deformation is a part of the Taiwan orogenic belt motion and modelled as an elastic block using 10 years of GPS horizontal velocity (Ching *et al.* (2011)). The interseismic deformation is distributed over the entire area, from the Chelungpu fault to the LVF on the east coast with a strong east dip (45–50°) while coseismic deformation was concentrated around the Chelungpu thrust fault (CTF) (Loevenbruck *et al.* (2001)). According to Yen *et al.* (2006) & Wang (2016), 1000 days before the mainshock, the strain rate was low. The pre-seismic crustal deformation was estimated at 1.4–7.9 mm/yr horizontally (north-westward) and 2–10 mm/yr vertically (uplift) (Liu *et al.* (2004)). The Chelungpu fault is situated between two main active faults: the Changhua fault to the east and the Shuangtung fault on its west side. These three faults are interacting and should be considered in the study of the interseismic deformation of Central Western Taiwan. However, Hsu *et al.* (2009) ignored the impact of the Changhua fault in its modelling considering that one or both faults should be equivalent as long as the creep occurs only downdip of where they merge into their common decollement i.e. assuming that the Changhua fault is fully locked.

The area that ruptured during the Chi-Chi earthquake was considered as strongly locked before 1999 as shown by the GPS data (Yu *et al.* (2001); Hsu *et al.* (2009)). However, not the entire locked area ruptured: the southern part presented very low coseismic deformation at shallow depth. Hsu *et al.* (2009) estimated the amount of the expected long-term slip rate or slip deficit on the locked fault zones. The accumulation of moment deficit rate is proportional to the rate of strain concentration and estimated from $1.2 \cdot 10^{18}$ to $3.7 \cdot 10^{18} N.m/yr$.

Nevertheless, earthquakes do not rupture regularly in time or equally distributed along a fault, as can be shown by paleoseismicity. In this case, several ruptures occurred along the fault, mainly on the north part and very few on the southern part. Thus, the irregularity and the distributed ruptures make it a highly complicated event to estimate a return period.

GPS studies run over the period 1990 and 1995 (Loevenbruck *et al.* (2001)) showed that the interseismic displacements are due to aseismic slip helping the convergence between the Philippine Sea plate and the Eurasian one. Due to this slip, an accumulation of stress is building up at the sub-horizontal decollement around 10 km depth. No abnormal behaviour of the area was visible. Also, interseismic velocity from GPS is implying that the locked area was situated at the west part of the decollement where major earthquakes are likely to happen (Dominguez *et al.* (2003)). Adding seismological data to the geodetic observations, the rupture of the 1999 Chi-Chi earthquake is consistent with the locked area during the interseismic.

From InSAR studies covering 1996 to 1999 with ERS images, about 32 mm of deformation is observable and considered as accumulation due to the EW tectonic compression and not atmospheric effects (Liu *et al.* (2004)).

From strain rate and seismicity studies (Hsu *et al.* (2009)), a shortening of 25 mm/yr over the Western Foothills towards the Coastal Plain was present. A high

seismicity was observable around Taichung basin during that period indicating a contraction of Central Taiwan on the west side, location of the Chi-Chi rupture and an extension on the east side. The strain-rate data shows that on the east side of the island, location of the LVF, a high NW–SE-directed contraction is present. Concerning the east extension, a high NW–SE to NEE–SWW-directed extensions is present and explained as a consequence of exhumation and crustal thickening. A large number of small earthquakes happened at the top of the decollement surrounding the locked fault zone during the interseismic phase.

2.2.2 Chi-Chi M_w 7.6 earthquake

This event occurred on 21^{st} September 1999 with a magnitude of M_w 7.6 (CWB: 23.85° N 120.82° E). The seismic moment is estimated at 3.046 x 10^{20}N · m by the United States Geological Survey (USGS) with a mean slip of 2-3 m. Thousands of people were injured or killed, and many infrastructures were destroyed. During the three months following the event (Ma *et al.* (2001)), thousands of aftershocks occurred including six with a magnitude greater than 6.5, starting at the north and migrating downward and southward of the main event (Wang (2016)). As presented in Lee & Y-X. (2011), it is interesting to look at the seismicity (Figure 2.3) and its implications for the tectonics. Two NW-SE patterns are observed: one starting at the north of the Chelungpu fault and one at the south end between the Luliao and Tachienshan faults. They point out the impact of this event on nearby faults such as the Luliao fault that most probably was activated during the Chi-Chi event. This earthquake was due to the reactivation of the Chelungpu fault: thrust faulting on a north-south striking fault plane dipping to the east (Lee *et al.* (2001)). The rupture was complex with several dislocations; it reached the surface and created a 100 km-long scarp between the hanging-wall to the east and the footwall to the west (Pathier *et al.* (2003)). From GPS data (see Chapter 4), a clear change of surface motion is visible at the north end of the fault turning towards east. According to the focal mechanism, this event is in agreement with the SE-NW plate convergence motion (Lee & Chan (2007)), with an overlap towards west linked to the orogen deformation and a double plate convergence boundary, on each side of the Central Range (Angelier *et al.* (2001)).

Over the past 20 years, several models of the Chi-Chi earthquake were computed, each of them focusing on specific aspects, using different data sets, techniques and/or methods. In this study, I will focus on the use of GPS, levelling, InSAR and SPOT offsets. For instance, Ma *et al.* (2001) showed by using seismological data that the total rupture duration is 28 s starting at the south of the fault and a northward propagation with static offset up to 8 s, mainly at shallow depths of less than 10 km.

The GPS measurements acquired from three years before the event to a few months after (Yu *et al.* (2001)) showed major horizontal displacements of 1.1 m to 9.1 m from NW to NNW on the hanging-wall with an uplift of 1.2 m to 4.4 m near

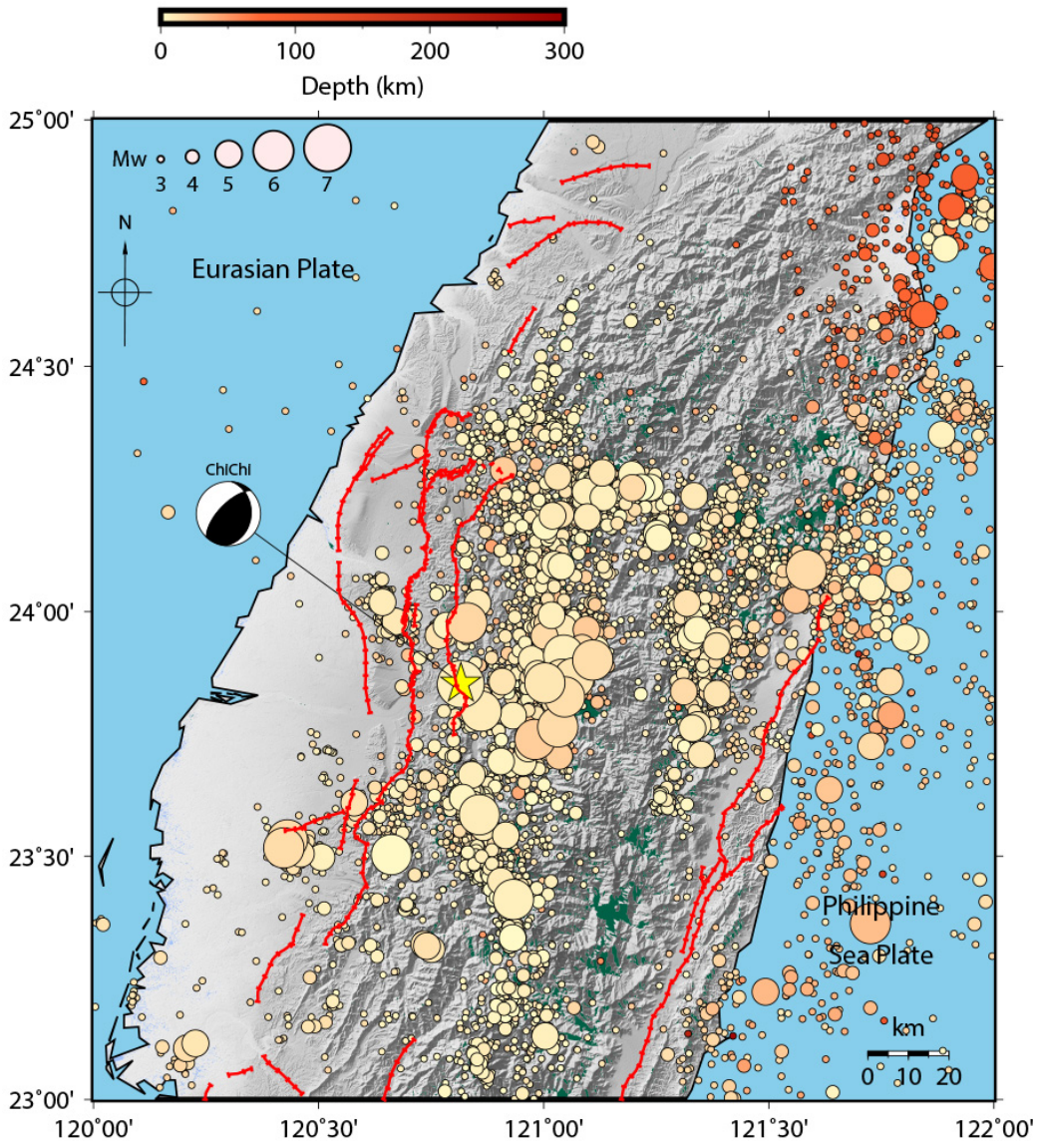

Figure 2.3: Seismicity (from 1998 to 2000) over Taiwan showing SE and NW trending seismicity at the northern and southern end of the Chelungpu fault and the focal mechanism of the Chi-Chi earthquake. Faults (detail in Figure 1.2) are indicated in red (National Taiwan university).

the rupture. The deformation is less significant towards the East and increases near the north end of the fault. Regarding the footwall, 0.1 m to 1.5 m were detected towards SE to ESE for horizontal displacements and 0.02 m to 0.26 m of subsidence.

Regarding studies using InSAR, only the ERS (European Remote-Sensing Satellite) constellation was previously used. Pathier *et al.* (2003) used ERS-2 products combined with GPS to study the footwall and reported some issues: the existence of a linear trend in phase difference caused by orbital error and atmospheric effects, also

the presence of non-coseismic displacements. Linear trend correction using GPS was applied to the interferograms to remove large scale perturbations but GPS are too sparse to constrain the error; 1.7 cm of uncertainty is estimated on the centimeter accuracy coseismic displacement map (Pathier *et al.* (2003)).

Due to limited contributions from ERS-2 interferometry to the surface coseismic deformation mapping of the hanging-wall (area presenting the major deformation but covered by a dense vegetation), a few researchers turned to optical images. Kuo *et al.* (2014) used aerial photos which gave understanding of the hanging-wall to build a high-resolution map of the horizontal coseismic deformation. Dominguez *et al.* (2003) used SPOT (Satellite Pour l'Observation de la Terre) images and interpreted the coseismic slip as shallow and detected more displacement on the hanging-wall than the footwall. Also, they estimated that the deeper part of the fault was not activated during the event and the western front of the area should produce a M_w 7 to 7.5 event every 150-250 years. However, Pathier *et al.* (2003) pointed out that non-negligible residuals were presented in Loevenbruck *et al.* (2001) and Dominguez *et al.* (2003) GPS based models. The residuals between each model and InSAR observations are estimated at 17 cm for Dominguez *et al.* (2003) and 7 cm for Loevenbruck *et al.* (2001). One explanation for this difference is the geometry used: Loevenbruck *et al.* (2001) uses a point source method while Dominguez *et al.* (2003) uses a plane dislocation (Okada (1992)).

In addition, several studies completed the knowledge on the fault using other data types: levelling data (Chen *et al.* (2011); Ching *et al.* (2011)), ground water level (Yen *et al.* (2006)), and reassessment of geodetic strain-rate and seismic stress fields (Chen *et al.* (2017)). Two other studies were done by Lee *et al.* (2001) using strong motion and Liao *et al.* (2013) using teleseismic data, mainly to test new techniques, confirmed the previous results obtained on the geometry of the hanging-wall of the fault. The slip is mainly confined at depths of less than 10 km, is centered around approximately 25-55 km north to the epicentre with a maximum slip of 20.4 m at 45 km north of the epicentre. The rupture velocity was between 0.3-3.8 $km.s^{-1}$. Using GNSS and strong motion, Ji *et al.* (2003) showed a model composed of three segments that explain quite well the data. Finally, Lee *et al.* (2001) run a simulation based on strong ground motion and concluded that heavy damages were constrained on the hanging-wall and serious shaking were present along the northward rupture direction.

Also, studies focusing on the neighboring areas of the Chelungpu fault were done focusing on the 2013 Nantou earthquake, in the western central part of Taiwan, creating a numerical model based on teleseismic body wave, cGPS and ground motion data (Lee *et al.* (2001)) and estimation of earthquake probability assessment for active faults in central Taiwan (Lee *et al.* (2016)).

Mainly based on GPS but also combining data sets (InSAR, SPOT or aerial photos), a few models were designed (see Figure 2.4). Johnson & Segall (2004) built a four-segment model based on GPS including a ramp decollement system at depth with a lateral ramp at the northern end. The main part is of about 70 km from the

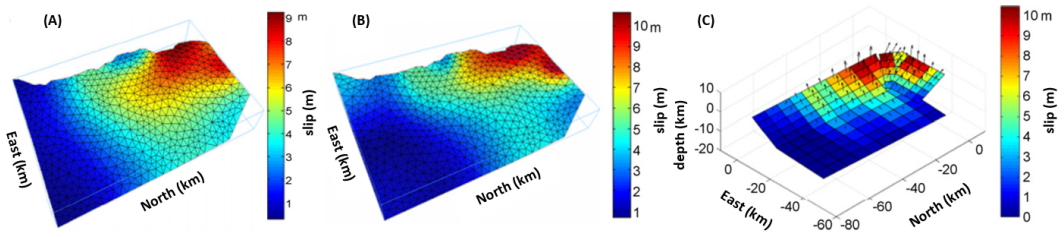

Figure 2.4: Chelungpu fault slip distribution (Zhang *et al.* (2008) using triangular dislocation elements (A) by inversion of InSAR and GNSS data (B) by inversion of GNSS only. (C) Chelungpu fault slip distribution using rectangular dislocation elements and inversion only based on GNSS (Johnson & Segall (2004)).

south to the north from Chushan to Fengyun; then, a 8 km long segment bending to the east; finally, a 25 km segment trending up to Shuangchi. Using GPS and InSAR, Zhang *et al.* (2008) constructed a model with triangular elements, a more realistic dislocation method to represent the curved three-dimensional fault surface without introducing overlaps and gaps. It shows similar slip pattern to GPS based models, but the magnitude of the fault slip is smaller and the slip pattern smoother.

The results of Dominguez *et al.* (2003) based on SPOT imagery pointed out a shallow 20-35° east dipping ramp with a low dipping decollement at a depth of 6 to 8 km. However, Hsu *et al.* (2002) concluded a decollement at a depth of about 12 km, more consistent with the hypocentral depth of the mainshock and the distribution of aftershocks. According to them, the maximum slip is happening at depth between 10 and 15 km on the shallow northern part of the fault with a moment of 3.6 x 10^{20} N $\cdot$ m but most of the moment was released at shallow depths (between 0 and 5 km). In addition, the area ruptured by the mainshock was fully locked before the earthquake. The slip is mainly aseismic for depths above 10 km (Hsu *et al.* (2009)). No earthquake similar in magnitude to Chi-Chi's is known to have occurred in recent centuries in Central Western Taiwan.

To conclude on the previous studies of the coseismic phase of the Chi-Chi earthquake, many questions or improvements are still needed. The focus of these research was on specific aspects or data type to model the slip distribution and the fault geometry. The low density of data (such as GPS and levelling) is not constraining the model enough to get a precise information, mainly on the decollement at depth. Non-negligible residuals are also present in models based on InSAR or optical data due to orbital errors, atmospheric effects or due to the resolution of the data. Finally, a debate on the geometry and position of the decollement at depth is still ongoing. All the knowledge on this event as well as the quantity and quality of data sets covering this area are an opportunity to test new techniques.

2.2.3 A complex mechanism: afterslip and viscoelastic relaxation

After a strain released episode or coseismic slip, a transient deformation episode occurs composed of various mechanisms of deformation and fluid flow. The fault slip can be described as steady aseismic creep, as recurring transient seismic or aseismic slip (Hsu *et al.* (2009)). However, these mechanisms are not well constrained or understood and can vary quite a lot in time and space. Furthermore, the recurrence of earthquakes and their sizes is dependent on the rheology of the crust and upper mantle, hence a precise description of the rheology is needed to build a model.

Two main mechanisms are running the postseismic phase: afterslip and viscoelastic flow. The afterslip deformation is mainly occurring near the epicentre of the event and decays rapidly. It was the main mechanisms of the first few years of the postseismic deformation of Chi-Chi event as shown in Loevenbruck *et al.* (2001); Hsu *et al.* (2002, 2007); Rousset *et al.* (2012). Then, a viscoelastic relaxation became the main deformation mechanism lasting for a longer period, broadly distributed and with higher rate than tectonic loading. As was presented previously, the coseismic deformation had a complex behaviour in time and space. The postseismic deformation is as much, with mainly displacement happening on the decollement in depth (see Figure 2.5).

A comparison of the seismicity before and a few weeks after the earthquake showed a clear increase of the number of earthquakes in the area starting at the mainshock (Lee *et al.* (2014)). Two groups are visible. A NNW-SSE trend from 1999 to 2001, with a main pick on the 21^{st} of September and a second one on the 12^{th} November 1999 with a M_w 5.3 earthquake. A second NE-SW trend is present until 2010. However, no particular change of depth in the seismicity is present. According to them, this first sequence might be due to the reactivation of a subsurface normal fault that strikes N10°W.

One of the complications to study the postseismic deformation of the Chi-Chi earthquake is the presence of two other active faults in the Western Foothills of central Taiwan. The Changhua fault, situated near the west coast and the Shuangtung fault, situated on the east side of the Chelungpu fault. Furthermore, the island is struck several times a year by strong earthquakes such as the M_w 6.8 Chengkung, the 2006 M_w 7.0 Pingtung, and the 2006 M_w 6.1 Taithung earthquakes disturbing the study of the time series.

In addition, the Chi-Chi earthquake had an unusual behaviour as most of the energy was released at shallow depth and not along the entire fault, mainly on the northern part. Most probably, some parts locked during the interseismic, still did not rupture. The north part of the Chelungpu fault that ruptured corresponds to an area locked during the interseismic period. The southern segment of the fault did not rupture during the event and did not present neither creeping before 1999 nor presents large afterslip deformation at shallow depth (Hsu *et al.* (2009)). In this case, postseismic displacement is located mainly in the south part on the

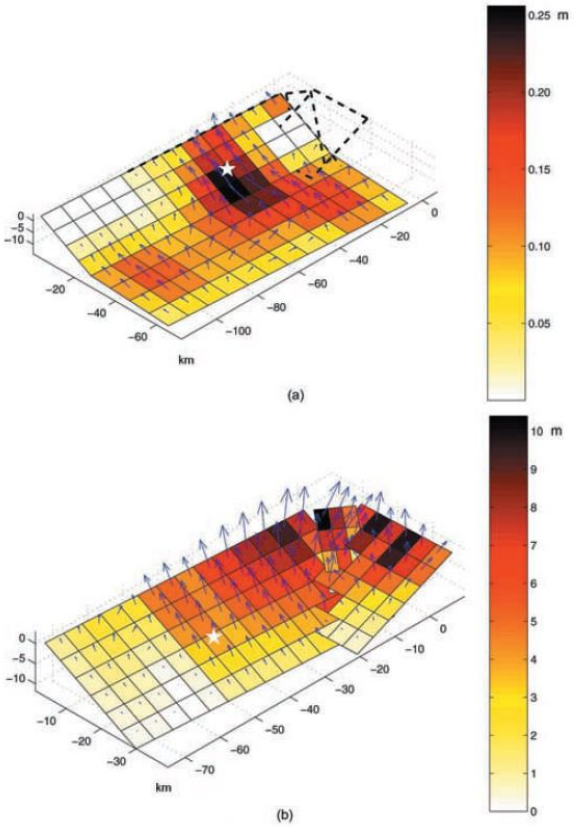

Figure 2.5: (Top) Postseismic and (Bottom) coseismic slip distributions (Hsu *et al.* (2002)).

decollement, with a maximum slip of 0.25 m in the three months following the event (12 m for the coseismic slip) (Hsu *et al.* (2002)). The afterslip distribution shows significant slip on the southern part of the decollement but little or no slip on the northern segments.

From a 15 months GPS measurement analysis, Hsu *et al.* (2009) noticed that in comparison with interseismic velocities, a systematic counter-clockwise rotation of postseismic surface displacements is present in the Central Range. They concluded that slip along the fault is mainly aseismic for depths above 10 km (presenting temperature beyond 200°C) and mainly seismic at shallower depth. The postseismic motion had been studied until 2008 with cGPS, Envisat (Huang *et al.* (2016)) and levelling (Ching *et al.* (2011)) showing the vertical displacement. The maximum slip is of 0.57 m in an area of high aftershock activity in the eastern region and the highest slip rates of about 1–1.5 m/yr near Chi-Chi and on the decollement (Hsu *et al.* (2007)). A detailed study (Wang *et al.* (2016)) of aftershock sequences was done working on the Chi-Chi event among many earthquakes showing a correlation between mainshock and aftershocks and ways to forecast large aftershocks. However, they also concluded that aftershocks are not entirely controlled by afterslip. A 14 years study showed that more than a decade after the mainshock, the deformation is

still more important than before the earthquake (3 to 8 mm/year faster (Tang *et al.* (2019))). About 1 m of cumulative afterslip is present on the southern segment of the Chelungpu fault, dominantly downdip from the ruptured area.

Afterslip models (Rousset *et al.* (2012); Sheu & Shieh (2004)) cannot explain the far field deformation, this is why more recent models are combining the two contributions: rapid afterslip localized around the epicentre and slower viscoelastic flow in the lower crust distributed on a larger area.

An important aspect to study while analysing viscoelastic flow is the variation of pressure and temperature with depth. Hsu *et al.* (2009); Rousset *et al.* (2012); Tang *et al.* (2019) included these parameters in their models and concluded that aseismic slip is dominant for temperature higher than 200°C. Hence, at depth below 30 km, a ductile deformation with a viscosity of $10^{19} Pa.s$ is dominant and mainly seismic at shallower depths corresponding to a brittle deformation with a viscosity of $5 \cdot 10^{17} Pa.s$.

In the 15 months after the event, afterslip released a cumulative moment of $3.9 \cdot 10^{19} N.m$ equal to about 11% of the coseismic moment (Hsu *et al.* (2009)). Afterslip is prominent on the decollement (80% of the seismic moment on the decollement while only 20% during the coseismic event) and in the southern part near the hypocentre and almost non-existent in the northern section (Hsu *et al.* (2007)). The afterslip moment is significantly higher than the seismic moment released by aftershocks, $6.6 \cdot 10^{18} N.m$ according to GPS data during the 15 months (between September 1999 and December 2000) following the main event, the postseismic deformation is supposed to be mainly aseismic.

Viscoelastic flow is less obvious, slower, and more distributed. It started more gradually with accelerated viscoelastic flow in the lower crust. After the event, an increase of Coulomb stress of about 1 MPa at 15 km depth is estimated on the creeping area corresponding to the aftershock distribution at depth 10–20 km depth (Hsu *et al.* (2009)). Furthermore, the change of behaviour from transient creep to steady state creep (viscoelastic relaxation) starts about a year after the event (Tang *et al.* (2019)).

Understanding the postseismic deformation of the Chi-Chi event requires to study both in space and time the deformation. Afterslip deformation is clearly present in the few months following the mainshock visible by a rapid and localized deformation, mainly on the southern segment of the Chelungpu fault (Tang *et al.* (2019)) near the epicentre of the Chi-Chi event, a transition zone that was creeping during the interseismic period.

2.3 Additional Deformation of Western Taiwan: Subsidence

I will briefly describe the subsidence happening in the south of the study area. Even though I am not further investigating this deformation, it is clearly present on the

interferograms and needs to be considered.

In central western Taiwan, a large quantity of groundwater is extracted each year for agricultural, aquacultural and industrial use and to provide drinking water for the population. It is causing large-scale land subsidence. This ground surface deformation is due to aquifer compactions, dewatering, and oxidation of organic soils, natural settlements of soils, and dissolution and collapse of Earth materials (Yang *et al.* (2019)). It has an environmental impact; it can cause flooding but also it is damaging structures such as the Taiwan High Speed Railway (THSR). The THSR is crossing Taiwan from the west coast from Taipei at the north to Kaohsiung at the south i.e. over 345 km and was installed in 2007. Several counties are impacted (Figure 2.6), over 2000 km^2 and up to a maximum subsidence of 3.2 m in 40 years, including at the north Taipei and Yilan, and Changhua, Yunlin, Chiayi, and Pingdong in Central and Southern Taiwan (Hsu *et al.* (2015)).

The most impacted area is Yunlin county situated over the Chuoshui River Alluvial Fan (CRAF), the largest aquifer in Taiwan (from the Wu River in the north to the Beigang River in the south and from the Baguashan Tableland and the Douliou Hill in the east to the Taiwan Strait in the west) which shows a subsidence rate greater than 30 mm/yr (Yang *et al.* (2019)) and crossed by the THSR.

The coast area of the counties was experiencing large subsidence from 1992 to 1999. Since 1999, inland areas are the most impacted: Huwei, Tuku, Yuanchang, and Baozhong Townships. The subsidence is completed by dike failures, seawater encroachment in coastal aquifers, coastal inundation, and salinity intrusion (Hsu *et al.* (2015)). In Mailiao, Lunbei and Baojhon Townships, a cumulative land subsidence of 110 cm was observed from 1992 to 2007 (Tung & Hu (2012)). Another county largely impacted by subsidence is Changhua, located at the north of the CRAF, and supposed to present abundant groundwater (Hung *et al.* (2012)).

Rainfall is a main parameter in this but unevenly distributed over the year (Hung *et al.* (2012)) and due to the topography, no large quantity of water can be stored. It has been observed that during the drought of 2015, the subsidence accelerated due to the large quantity of ground water extracted from shallow and deep aquifers and that more water is extracted during dry season than wet season (Hsu *et al.* (2015)). From piezometer data (Tung & Hu (2012)), the land subsidence rate is varying along season with the underground water level: a drop is present during the wet season (May to October) and remains constant or rises the rest of the year. A rate of about 1.5 cm/year is observed for the summertime and 9.0 cm/year for the wintertime. InSAR results are even showing that the land subsidence in dry season is up to 60-74% of the annual subsidence (Yang *et al.* (2019)).

In this study, I am focusing on the earthquake deformation and did not focus on this subsidence displacement which was already well studied with dense levelling network in the literature. For the postseismic modelling, I hid Yunlin and Changhua counties on the west of the study area.

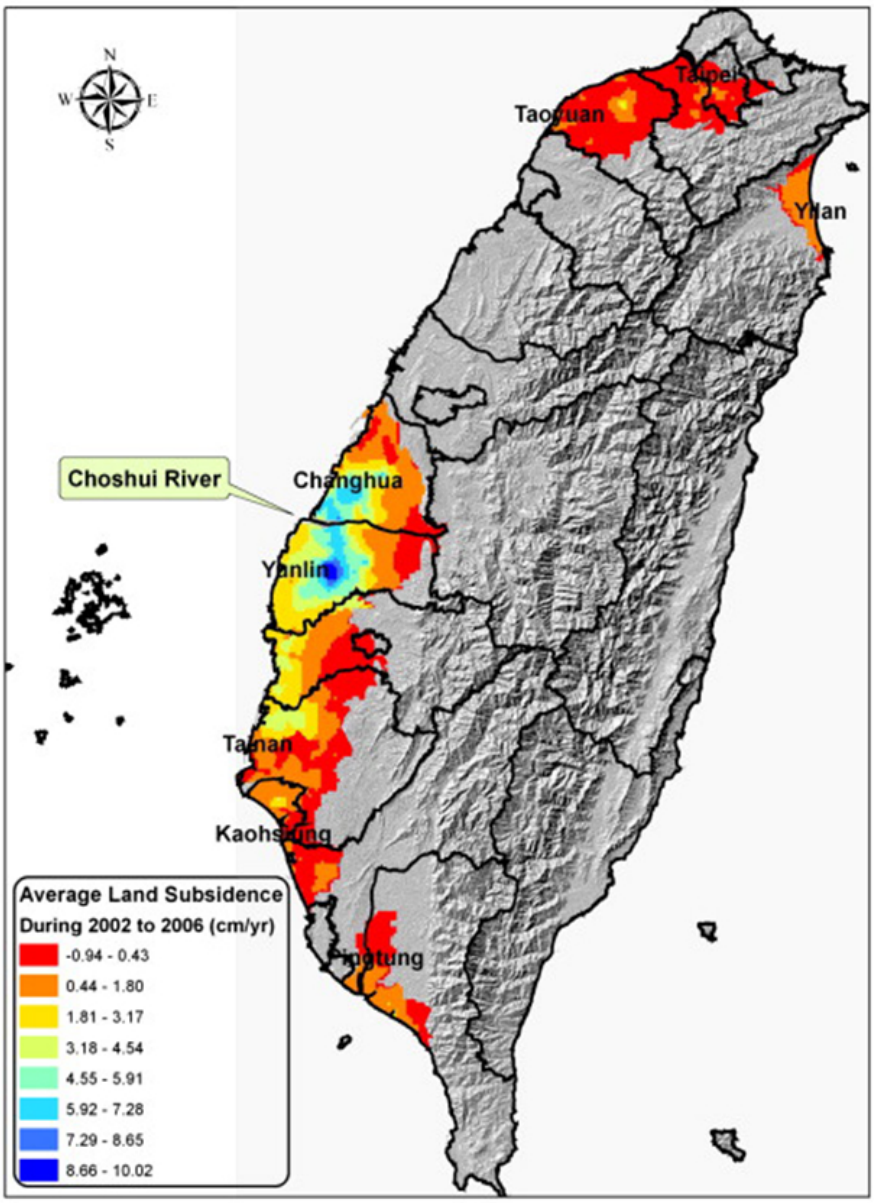

Figure 2.6: Average land subsidence area in Taiwan during 2002 to 2006. Black lines are the administrative boundaries. Figure extracted from Tung & Hu (2012).

2.4 Motivations and innovations

In this thesis, I will attempt to obtain more insights on the earthquake cycle of the Chi-Chi earthquake based on the knowledge provided by previous research and by building a methodology specific to the case. I am not aiming at estimating the recurrence time interval for this specific earthquake, but in the goal of getting more knowledge of the deforming areas. The area around the Chelungpu fault is intensely compressed due to the subduction and collision happening between the

Philippine Sea plate and the Eurasian plate. The Chi-Chi event had a complex rupture over a long area and is situated within many active faults. It is in an area stuck several times a year by seismic events as well as deformed by a large subsiding area. The understanding of the specific deformation associated to the Chelungpu fault is difficult to get. However, finding "precursors" (such as seismicity patterns, crustal deformation, or groundwater level change) associated with the earthquake and understand the transient deformation happening in the months or years after, are giving essential information for the monitoring of the area. Currently, 20 million people live in Taiwan under the constant threat of large earthquakes and potentially tsunamis as most cities are along the coast. It is therefore essential to better understand the processes controlling earthquakes in this area and identify which areas are prone to produce destructive events. Monitoring and increasing the information on the tectonic structures is crucial for hazard assessment.

Currently, most studies done on Taiwan are about the east area with the LVF and the south part due to the lack of new observations and the need of improvement of modelling techniques. In this thesis, I am using the strong background of geodynamic available to build methodologies for combining Earth Observations (EO) inversion techniques. The main difficulties of this area are the lack of precise information in the years around the earthquake (nowadays the GPS network is denser) and the non-coherence of InSAR on the hanging-wall due to the dense vegetation. Furthermore, atmospheric corrections and time series algorithms have considerably improved as well as inversion packages. The use of these techniques as well as the combination of EO will give more information of the past and current deformation.

In the next chapter, a precise description of the EO used in this study and how they can be used to measure surface displacement will be presented. In Chapter 4, a revisit of the coseismic phase of Chi-Chi earthquake will be done with the goal of combining five EO data with estimation of relative weights to realise a model of the Chelungpu fault and estimate the slip distribution. In Chapter 5, an analysis of the 20 years of deformation since the earthquake happened will be done using InSAR and GPS to detect the current state of the deformation. Based on the data available and previous studies, a study of the afterslip and viscoelastic relaxation will be realised to better understand the slip distribution of the postseismic deformation in comparison with the coseismic one.

2.5 Summary

A condensed description of the geodynamic of Taiwan with a focus on the Chelungpu fault area was presented in this chapter. According to previous studies, hazard assessment was giving a low probability of this area rupturing before the Chi-Chi earthquake struck the island. The complexity of the island with the presence of several active faults is demanding a precise knowledge of geology and tectonic, but also of a high precision from data and models to be able to differentiate the mechanisms deforming the area. Also, the geometry of the Chelungpu fault is not fully

understood, a large debate is still ongoing on the presence and geometry of the decollement.

The literature about the interseismic period leading up to the Chi-Chi earthquake gave us information to base the study on, which areas where fully locked before the rupture happened and which areas were deforming. No further investigation of the pre-seismic period was done in this thesis as the quantity of data available at that time is low (only a few GPS permanent stations were available and a few ERS images).

Coseismic studies used separately geodetic data (GPS, InSAR and optical images) to model the geometry of the fault and its slip distribution. From these models, gaps coming from techniques used or insufficient constraints are present. Residuals are present in slip distributions and discussions about the decollement in depth and the exact geometry of the fault are still ongoing.

The postseismic studies covered mainly the 15 months following the earthquake or focused on the rheology. A comprehensive and precise postseismic deformation understanding by covering the 20 years since the fault ruptured is essential to reference the more risky areas and improve hazard modelling.

Chapter 3

Remote Sensing and Geodetic Observations

3.1 Introduction

Remote sensing is the science of detecting and analysing the physical characteristics of an object thanks to the analysis of the signal emitted or reflected using a sensor. The instrument is not in direct contact with the object and can be mounted either on airborne, space borne or terrestrial platforms. Even though surface deformation can be analysed accurately by in situ measurements, field observations are challenging to get due to the complexity of the ground, they require time and hard work without obtaining a general overview of the displacement.

Several remote sensing and Earth Observations (EO) techniques exist. In this chapter and thesis, a few will be presented and used: Synthetic Aperture Radar (SAR) and optical images, Global Positioning System (GPS) and levelling.

In order to acquire information about the Earth's surface thanks to satellite equipment, two types of sensors exist to generate images of the ground. First, active sensors such as radar sensor (i.e. ERS, EnviSAT, Sentinel-1) and second, passive sensors such as the optical sensor (i.e. SPOT, Sentinel-2). The resolution of the imagery is one of the main parameters to consider, four types exist: radiometric (amount of information in each pixel, a high radiometric resolution enables to distinguish more details and variation in light), spatial (size of each pixel within an image and which area is represented by that pixel), spectral (how much differences in frequency can be detected by the sensor), and temporal (revisit time of the satellite).

GPS measurements and SAR images are complementary sources and can be used together for analysis of active tectonic structures horizontally and vertically due to their geometry of acquisition and, spatial and temporal sampling density differences. Spatially, GPS have a less dense coverage as InSAR. However, GPS can give measure every 5 min or even less in comparison with SAR acquisition done several days apart (the shorter one being Sentinel-1 with 6 days of revisit time while using A and B

satellites).

Sub-pixel analysis of satellite optical images for earthquake deformation is an efficient technique to measure horizontal displacement with high precision. This technique can pair easily with SAR due to their frequency differences.

With the high availability and variety of data, building strong geodetic observations based methodologies to monitor the Earth are essential. The current research is conducted for methodological improvement of EO processing and co- and post-seismic modelling in the context of surface deformation measurement due to earthquake.

This chapter focuses, first, on the main aspects of space borne imaging radar and its processing. A brief introduction of InSAR history will be followed by the principles and main challenges of SAR and InSAR. Finally, InSAR time series will be presented in Section 3.2.5. The second main section will focus on sub-pixel correlation of optical satellite imagery, its principles and the processing methodology followed. Finally, a brief introduction of GPS system will be presented in Section 3.4, as no actual processing was done in this work.

3.2 Synthetic Aperture Radar

Synthetic Aperture Radar (SAR) is a microwave imaging system. It is an active sensor with day and night operating capabilities, penetrates clouds and measures through any climates. SAR can be operated from ground-based aircraft, satellite platforms or radar-based terrestrial remote sensing imaging system (GBSAR). In this thesis, only SAR satellite will be used.

Since the launch of the European Remote Sensing satellite (ERS) in 1991, many improvements have been made with satellite sensor improving the resolution, reducing the revisit time, and increasing the data coverage. Figure 3.1 shows an overview of SAR satellites; historic ones, and those still in missions. The characteristics of the satellites used in this thesis are summarized in Table 3.1 (information extracted from `https://earth.esa.int/web/guest/missions/esa-eo-missions`).

3.2.1 Principle of Synthetic Aperture Radar

The satellites (such as Sentinel-1, ERS and EnviSAT) are evolving on a near-polar orbit. Polar orbit means that the inclination is about 90° to the equatorial plane in order to scan the entire planet including polar regions. Most of them are sun-synchronous (the satellite passes over the same area at the same solar time at each cycle). Satellites are following near-polar (northward and southward) orbits at an altitude of 500 to 800 km: the descending and ascending orbits (Figure 3.2). The descending orbit of a satellite is the path from the North pole to the South pole and south to north is the ascending one. The angle between north-south axis and the orbit varies between satellites but is usually of about 10°. Both orbits are visiting the same areas.

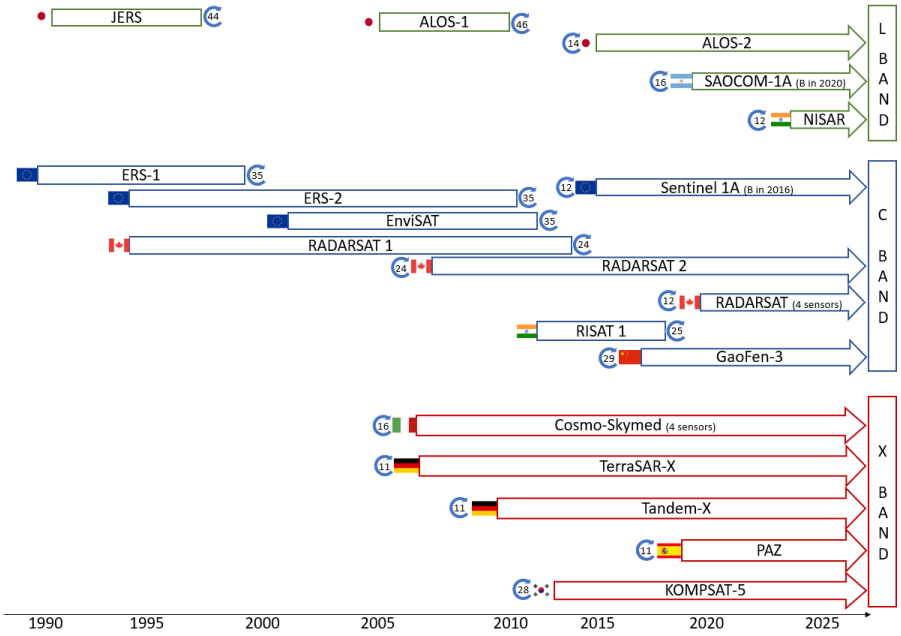

Figure 3.1: Overview of SAR satellite missions.

Table 3.1: Characteristics of satellites used in this study.

Mission	ERS-2	EnviSAT	Sentinel-1A/B
Launch date	21/04/1995	01/03/2002	A: 03/04/2014 B: 25/04/2016
End date	06/07/2011	08/06/2012	-
Altitude	785 km	790 km	693 km
Orbit inclination	98.52°	98.54°	98.18°
Revisit time	35 days	35 days	6 days (with A & B)
Incidence angle	23°	15-45°	18.3-46.8°
Resolution			
Ground range	25 m	25-50 m	5 m
Azimuth	5 m	5 m	20 m

On board the satellite, the radar carries an antenna that emits a microwave signal towards the ground (series of electromagnetic pulses) along the line-of-sight (LOS) (Figure 3.3) and the reflected signal is analysed (Figure 3.4). A target on the ground that reflects the signal is called a scatterer. As each scatterer is at a different distance of the radar, a delay is present between the transmission of the radiation and the back-scattered signal. This delay is equivalent to the phase change between both signals. As will be explained later in more details, the quality of the returned signal is affected by many parameters such as the geometry of the target, the relief, vegetation and roughness of the ground or the impact of the atmosphere.

The phase can be approximated as detailed in Ferretti *et al.* (2007) with equation

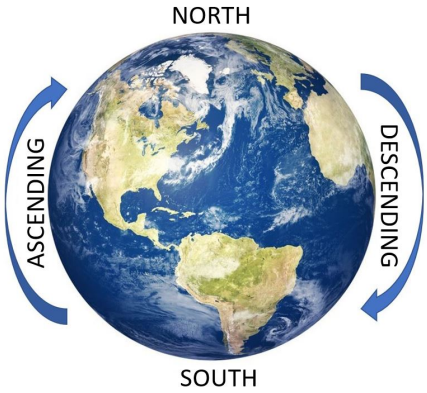

Figure 3.2: Ascending and descending orbits of a satellite.

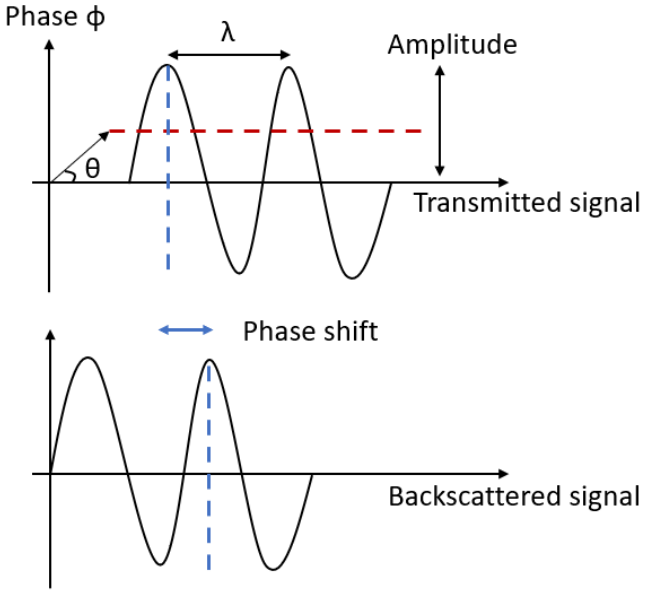

Figure 3.3: Principle of the SAR phase.

3.1:

$$\phi = -\frac{4\pi}{\lambda} \cdot R \qquad (3.1)$$

R: Distance radar-target;
ϕ: Phase;
λ: Wavelength (C-band: 5.6 cm).

A SAR imaging system is presented in Figure 3.4. The inclination of the antenna has a right-side looking geometry for SAR system such as used in this thesis (ERS, EnviSAT and Sentinel-1). The azimuth or along-track angle represents a linear distance in the direction parallel to the radar flight path and the range corresponds to the LOS distance from the radar to the illuminated area. The distance between the position of both satellites projected onto to the slant range is called the perpendicular baseline. The difference of acquisition time is called the temporal baseline.

Various radar systems exist associated with specific bands of the electromagnetic

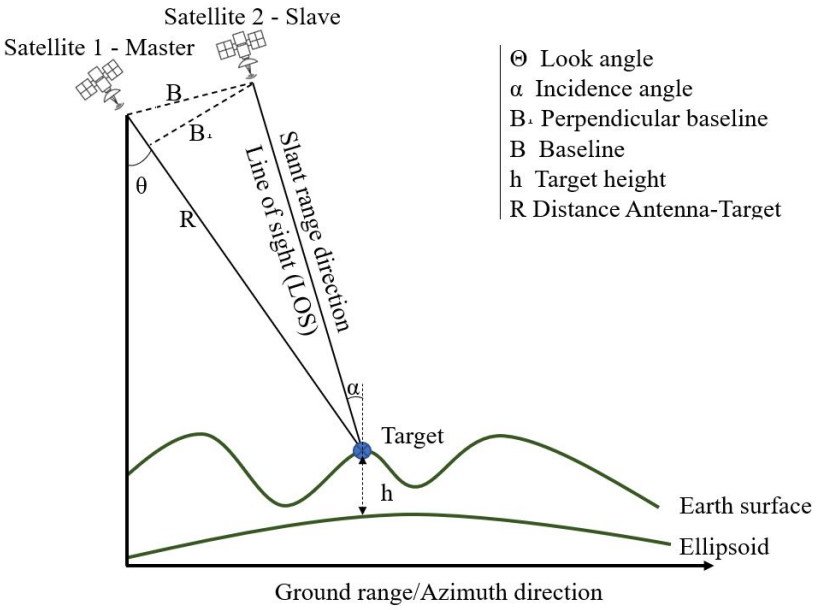

Figure 3.4: Geometry of repeat-pass SAR (adapted from Bhattacharya *et al.* (2012)).

spectrum to detect object on the ground:

- L-band ($f = 1 - 2$ GHz, $\lambda = 16 - 30$ cm): long band for long range traffic control and aerial surveillance. GNSS and passive radar are based on it as well as ALOS satellite;
- C-band ($f = 4 - 8$ GHz, $\lambda = 4 - 7$ cm): transponder meteorological radar, used for Sentinel-1, EnviSAT or ERS;
- X-band ($f = 8 - 12$ GHz, $\lambda = 2.5 - 3.75$ cm): used mainly by military forces.

A SAR image is composed of pixels. Each of them gives a complex value composed of phase and amplitude information from the microwave signal for all the scatterers within this resolution cell (Ferretti *et al.* (2007)) (rows of the image are along azimuth direction and columns along slant-range direction). The amplitude is related to the energy of the back-scattered signal and mainly depends on the roughness of the ground (urban areas have a high amplitude while flat sources have low one). Also, changes in dielectric constant of materials (due to composition or moisture) also affects the amplitude values of a SAR image. The phase is directly linked with the two-waves travel of the signal which allows the estimation of the ground displacement.

Three geometry effects are impacting the acquisition of the phase: foreshortening, layover, and shadowing effect (Figure 3.5) due to the side-looking geometry of SAR-antennas.

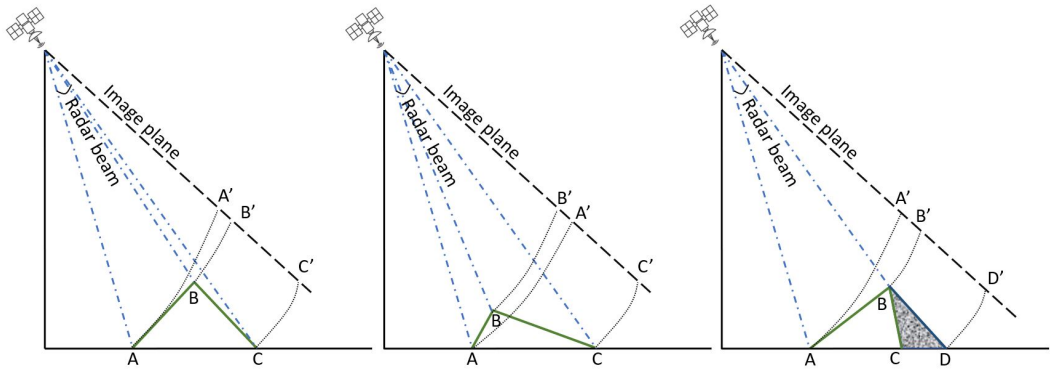

Figure 3.5: Foreshortening, layover and shadowing geometries (adapted from `https://earth.esa.int/handbooks/asar/CNTR1-1-2.html`).

- The foreshortening is the compression of the slopes oriented towards the satellite while they are projected onto the slant-range plane.
- The layover is the contrary of the foreshortening, it creates a distortion effect appearing when the angle of the slope oriented towards the satellite is bigger than the incidence angle.
- The shadowing effect appears when the opposite slope (not towards the satellite) is really steep in comparison with the incidence angle. Hence, some parts are not illuminated by the radar.

3.2.2 SAR interferometry

SAR interferometry (InSAR) allows to obtain the topography and the deformation by processing radar images. The method used in this study is to measure the modification of the signal phase between two images acquired at two different times over the same area. A difference in the distance between the sensor and the ground will create a change of the phase value. So, in order to quantify the displacement, the difference of phase between two complex radar SAR observations is calculated from two sensors with very close positions. Other SAR satellite configurations exist such as SRTM (Shuttle Radar Topography Mission) which possesses 2 independent SAR systems on board, one in C-band and the other X-band, representing a single-pass interferometer used for DEM generation.

InSAR representation (Figure 3.6), an interferogram, corresponds to a matrix of phase values uniformly located between $-\pi$ and $+\pi$, showing the change in surface displacement. It is the complex result (equation 3.2) of the multiplication of the primary (or reference) matrix S_1 times the complex conjugate S_2 of the secondary:

$$I = S_1 \cdot S_2^* \tag{3.2}$$

After combining the phase of two images, an interferogram is generated in which the phase is highly correlated to the terrain topography. Differential interferometry is used to obtain only surface deformation patterns by removing the phase shift related to topography.

The interferometric phase (Ding *et al.* (2008)) can be detailed as equation 3.3: a flattened phase (from the elevation variation of the Earth's surface), a target altitude from which a DEM can be extracted, the ground deformation term and the phase noise that will be detailed later.

The flat-earth phase is the part of the interferometric signal due to the variation of the range distance across the image i.e. due to the curvature of the Earth. This term is estimated using orbital and metadata information with a 2D-polynomial. Its removal leaves the interferogram with only fringes related to change in elevation (but still disturbed by noise or atmosphere).

$$\Phi = -\frac{4\pi}{\lambda} \cdot B_{perp} \cdot \Delta\theta - \frac{4\pi}{\lambda} \cdot \frac{B_{perp}}{R \cdot \sin(\theta)} \cdot h + \frac{4\pi}{\lambda} \cdot d_{los} + \epsilon_{noise} \tag{3.3}$$

λ: Wavelength of the radar signal;
B: Baseline length with B_{perp}, the perpendicular component;
R: Distance satellite-ground target with a height of h;
θ: Look angle, which is shifted due to the Earth's curvature by $\Delta\theta$.

This expression can be transformed to express the interferometric phase as a function of the primary and secondary geometry and the topography using equation 3.4:

$$\delta\Phi_{topo} = \frac{4\pi}{\lambda} \cdot \frac{B_{perp}}{r_0 \cdot \sin(\theta)} \cdot \delta h \tag{3.4}$$

λ: Wavelength of the radar signal;
B_{perp}: Perpendicular baseline;
r_0: Reference distance;
θ: Look angle;
h: Height of every point of the image.

In order to isolate the InSAR phase and only have the topography dependence term, a flat-earth term (due to the elevation variation of the Earth's surface, it can be calibrated using the baseline length) has to be cancelled considering that it has a constant linear phase term (see processing steps in Section 3.2.3). By exploiting this, the topography can be retrieved thanks to the extraction of the height from the two acquisitions taken at different positions.

At this point, the interferogram phase is wrapped. This means that the topography is represented as 2π cycles called fringes and provides an ambiguous measurement of the ground displacement. One full cycle in the interferometric fringes represents a change of half the wavelength between pre- and post-displacement images. By counting the number of fringes and multiplying by half of the wavelength,

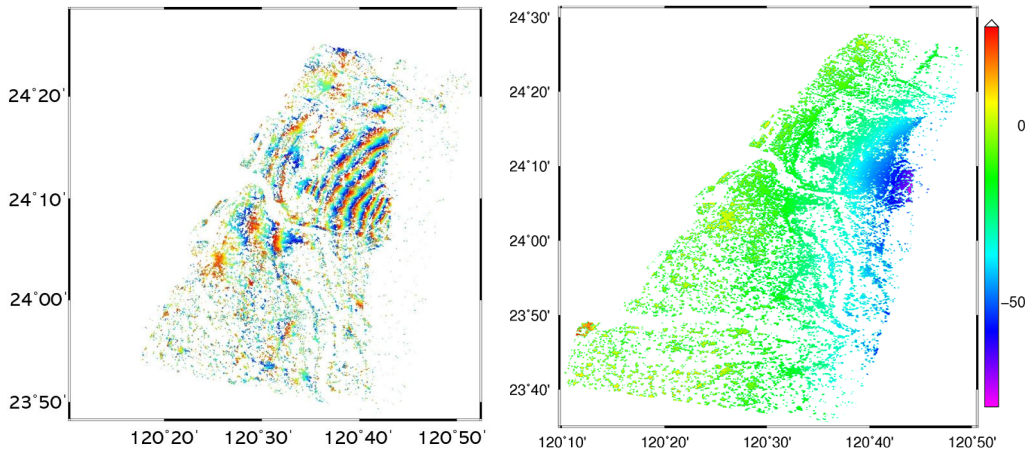

Figure 3.6: Example of wrapped (left) and unwrapped (right) interferograms (legend in cm).

a relative ground motion can be estimated between two points on the ground (the closer the fringes are to each other, the larger the displacement gradient is). A high frequency fringe is observed in the direction where the displacement quickly varies.

To create the differential interferometric phase (equation 3.5), we have to subtract these two signals:

$$\Delta\Phi = \Phi\_2 - \Phi\_1 = \Delta\phi + 4\pi \cdot \frac{\Delta R}{\lambda} + \Delta\nu + \Delta\eta \quad [2\pi] \tag{3.5}$$

$4\pi \cdot \frac{\Delta R}{\lambda}$: Geometric phase coming from the target-sensor distance;
$\Delta\Phi$: Components with same scattering properties;
ν: Components with same atmospheric conditions;
η: Components with same system noise component.

In order to respect the condition of stability, we should have $\Delta\phi = \Delta\nu = \Delta\eta = 0$. Hence, we obtain equation (3.1).

To unwrap the interferogram, the correct integer multiple of 2π must be added to each interferometric fringe.

3.2.3 InSAR processing

The processing of the SAR images is composed of several steps. The main steps are summarized in Figure 3.7 and explained here after. Some additional steps are useful depending on the satellite.

Co-registration of images: At least two images must be co-registered into a stack to create an interferogram. One image is selected as the primary (reference image) and one or more as secondary(ies) . This step will align the pixels (in range

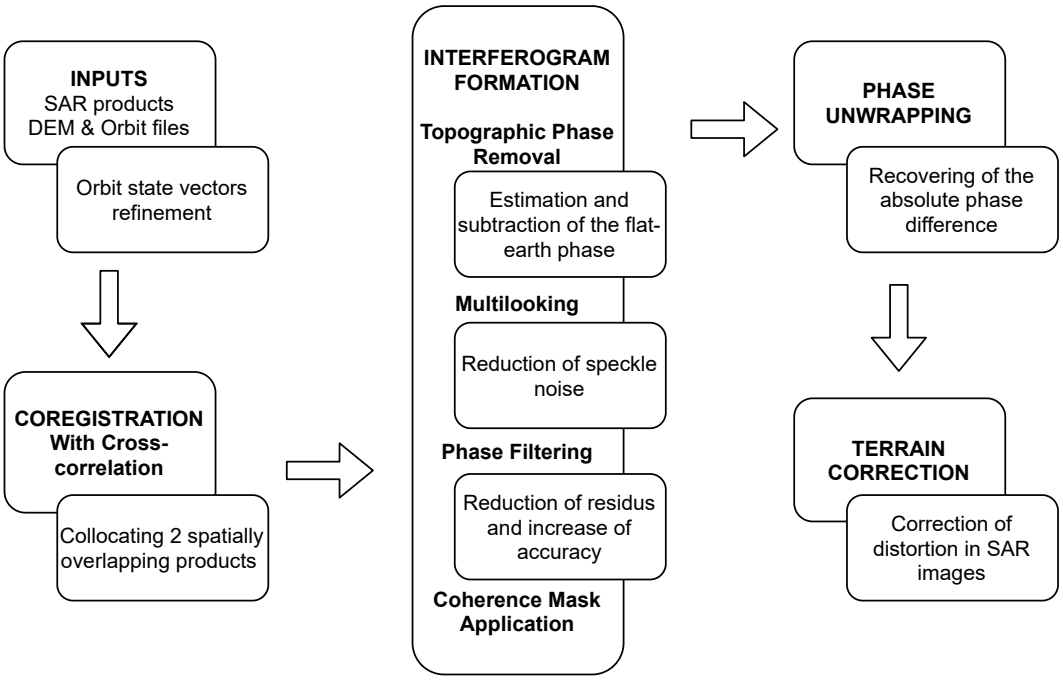

Figure 3.7: Flow chart of a standard repeat-pass InSAR processing.

and azimuth) of the secondary image(s) to the ones of the primary, up to sub-pixel accuracy. Orbit auxiliary data are used, they contain information about the position of the satellite at the time of acquisition of the image. A Digital Elevation Model (DEM) is used (commonly SRTM used).

Interferogram formation: To form an interferogram, the multiplication of the complex primary image by the conjugate of the secondary image is realised. The interferogram phase is wrapped which means that the topography is represented as 2π cycles called fringes. One full cycle in the interferometric fringes represents a change of half the wavelength.

Topographic Phase Removal: The interferogram is flattened by removal of the topographic phase. The operator will simulate an interferogram based on a reference DEM and subtract it from the processed interferogram. The flat-earth phase is due to the curvature of the reference surface. If the terrain is flat, constant or slow variation of fringes should be observed (obviously depending also on the coverage of the SAR images; if the area of interest is small, no fringe will be observed on a flat terrain).

In order to reduce the decorrelation of the phase, it is essential to keep high coherence pixels; otherwise the interpretation of the interferogram will be corrupted. To reduce the noise, spatial filtering is applied through filtering and multi-looking of the phase.

Multi-looking: Within each resolution cell, several scatterers are present creating a phenomenon called the 'speckle effect', which can be described as salt and pepper effect. To properly analyse the phase band of the interferogram, the signal to noise ratio is increased by multi-looking: averaging the intensity of adjacent pixels within a defined window. However, the higher the multi-look factor is, the more reduced the speckle noise will be but as well will the spatial resolution be. Also, multi-looking reduces the processing time.

Goldstein Phase filtering: An interferometric phase can be corrupted by noise from temporal or geometric decorrelation, volume scattering or processing errors. In order to unwrap the phase, the interferogram must be coherent, this step permits to increase the signal-to-noise ratio (SNR). Goldstein filter (Goldstein & Werner (1998)) is one of the main filtering algorithms to effectively suppress noise from interferogram. The quality of the fringes can be increased by applying specialized phase filter which uses a Fast Fourier Transformation (FFT) to increase the SNR of the image. However, filtering will not increase or restore coherence.

Unwrapping: As previously introduced, the electromagnetic wave is generated by the sensor periodically making the interferometric phase ambiguous and known within 2π. Unwrapping is used to relate the interferometric phase to the topographic height.

The hypothesis behind phase unwrapping is that the phase of two neighbouring pixels should only differ by a fraction of π. To recover the displacement, the appropriate multiple of 2π is added to the interferometric phase for each pixel making the signal continuous in space (Chen & Zebker (2000); Goldstein & Werner (1998)) using equation 3.6:

$$\phi_{unw} = \phi_{wrap} + 2k.\pi \tag{3.6}$$

Unwrapping is the most complicated step in the interferometric process and can impact largely time series analysis. Even though phase information cannot be restored, the quality of the fringes can be improved. Therefore, before unwrapping, spatial filtering is applied to the interferogram. If the phase is coherent and with a moderate deformation rate over the whole interferogram, then it is a straightforward step. However, for non-coherent area or with large deformation gradient (in case of a large earthquake for instance) in comparison to the pixel resolution of the image, neighbouring pixel value difference is larger than π and offsets are present in the unwrapped interferogram disturbing the interpretation of the interferogram.

In this thesis, phase unwrapping is done using SNAPHU (a two-dimensional phase unwrapping algorithm developed by Chen & Zebker (2000, 2001, 2002)) and the Minimum Cost Flow (MCF) method. This is a local method which unwrap the interferogram by a neighbouring technique by adding multiple of 2π to the phase. This method is highly dependent on the initial interferogram. The software is publicly available and runs on most Unix/Linux platforms. This technique is

complex to apply and often need to be corrected by phase closure algorithms, see Section 5.3.4.

Range Doppler Terrain Correction (Geocoding): Geocoding of the image by correcting SAR geometric distortions. The interferometric phase is projected into a geographic coordinate system thanks to a DEM.

3.2.4 Challenges and mitigation approaches

Several parameters are impacting the interferometric phase. Each of them has to be carefully evaluated and compensated in order to obtain the displacement information. Orbital and atmospheric errors are also partially mitigated by the time series analysis as will be described in Section 5.3.4.

Decorrelation

In function of the source (Ding *et al.* (2008)), it is characterised as decorrelation (noise caused by error sources that have a correlation length smaller than a regular coherence estimation window) or as coherent noise (such as atmospheric artefacts or orbit errors).

The main parameter quantifying the decorrelation is the coherence γ linked to the quality of the phase (for instance, a high coherence is present over urban areas but low over forest or water areas). Ideally, it should be obtained from the expectation values by equation 3.7:

$$\gamma = \frac{E\{S_1 \cdot S_2^*\}}{\sqrt{E\{|S_1(n)|^2\} \cdot \{|S_2(n)|^2\}}} \tag{3.7}$$

To sum up, all the terms composing the interferometric signal can be expressed by equation 3.8:

$$\Delta\phi_{int} = \Delta\phi_{def} + \Delta\phi_{topo} + \Delta\phi_{orb} + \Delta\phi_{atm} + \Delta\phi_{noise} \tag{3.8}$$

The topographic term $\Delta\phi_{topo}$ comes from the ground geometry (topography and Earth curvature) that can be corrected by using a DEM (Digital Elevation Model). After removal of this term from the interferometric signal, residuals from the DEM uncertainties are left. In the case of no DEM uncertainties and/or if the perpendicular baseline is equal to zero, then, this term is null;

The deformation component $\Delta\phi_{def}$ represents the change of the ground position in the slant-range direction between the two acquisitions;

Large correlation length errors are composed of the orbit inaccuracies ($\Delta\phi_{orb}$ related to the acquisition system) and the atmospheric artefacts: $\Delta\phi_{atm}$ induced by the ionospheric and tropospheric contributions, the change of scattering properties and the modification of the atmospheric parameters between the two acquisitions (relative humidity, temperature, and pressure).

Finally, there are the small correlation length errors or decorrelations combined in the $\Delta\phi_{noise}$ component. This term is reflecting the incoherent surfaces (forest or water), mis-registration decorrelation coming from the co-registration of the pixel prior the interferogram formation, spatial decorrelation coming from the different looking directions, the Doppler centroid decorrelation equivalent as an azimuth spatial decorrelation, volume scattering linked to the penetration of the radar waves into the illuminated scene and the temporal decorrelation due to the change of the wavelength-scale scatterers properties between two images.

Orbital ramp correction

Orbital ephemerides (position and velocity vectors of the satellite with a cm precision) are used to retrieve precise satellite state vectors. However, they are not always accurate enough, especially for ERS and EnviSAT, due to inaccurate orbit geometry determination. For more recent satellites such as Sentinel-1 or ALOS-2, GPS receivers on board is considerably improving the geometry determination.

Long-wavelength errors are present on the interferograms (Massonnet & Feigl (1998)) but can be due to atmospheric delays or orbital errors (spatially correlated but temporally uncorrelated). The complex spatial-temporal pattern can create a bias in the velocity field indistinguishable from slow deformation signals disturbing the interpretation of the phase (Ferretti *et al.* (2007); Hanssen (2002); Yu *et al.* (2020)). Most time series analysis method are removing a planar ramp from the phase (however, usually insufficient), and can potentially remove actual deformation signals such as post- or inter-seismic displacements. To correct the orbital error, a spatio-temporal filter is applied (composed of high-pass filter in time and low-pass filter in space) and separating noise components from the actual displacement. However, applying atmospheric correction and orbital correction (both removing long-wavelength signal) together, can remove the actual displacement as well.

Atmospheric error

SAR techniques are very efficient to estimate ground deformation at large scale thanks to satellites. As two images are computed with temporal separation while producing an interferogram, the impact of the difference in the path length can be important knowing that it equals a part of the radar wavelength (for C-band radar: λ=5.66 cm).

The Earth atmosphere is hypothesized at the first order as horizontally stratified due to the Earth's gravity (Kelley (2009)) and composed of many layers with different temperature gradients. Figure 3.8 shows a representation of the temperature and pressure profile according to the height.

The pressure is decreasing with the height, but the temperature has a different behaviour steered by the "pauses" in the atmosphere. Several parameters related to temperature and pressure are destabilizing the layers such as thermal radiation which create convection and tropospheric baroclinic instabilities from the vertical

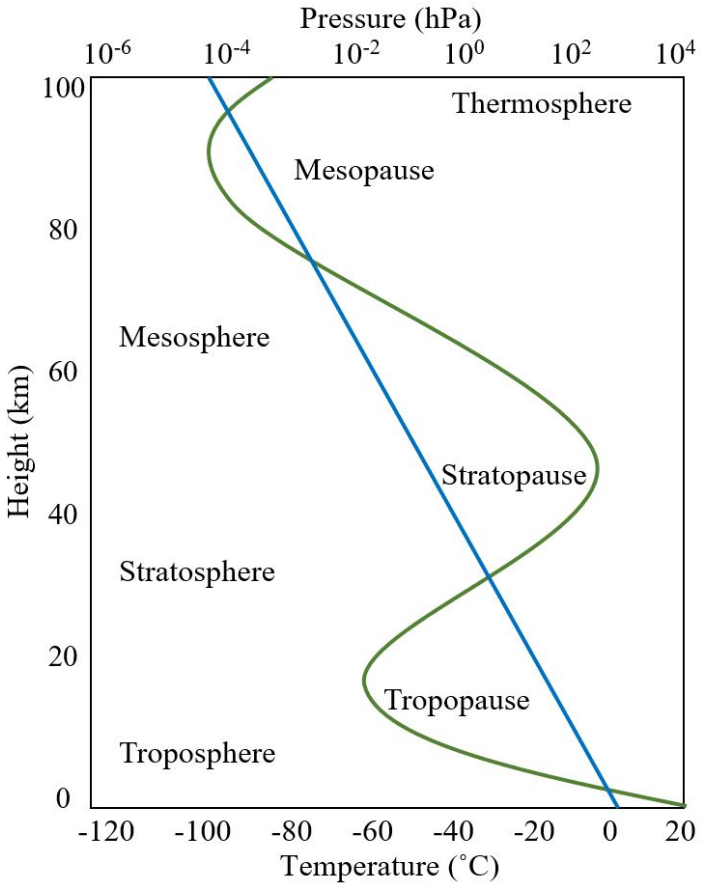

Figure 3.8: Atmospheric pressure and temperature profiles for mid-latitudes. The green curve represents the vertical variation of pressure and the blue line, the temperature.

wind shear. The stratosphere, around 30 km of height and above the troposphere, contains almost no cloud formation and so, is quite dry and does not perturb much the signal. The main contribution to the atmospheric signal comes from the water vapor distribution in the low height of the atmosphere, the troposphere as explained by Hanssen (2002). The troposphere contains 80% of the total atmospheric mass and most of the water vapor of the atmosphere. The ionosphere is the ionized portion of the upper-atmosphere, above 60 km and is described as vertically organised by the electron density variation with altitude.

The atmospheric artefacts are due to these layers (described by different refractivity indexes) crossed by the electromagnetic waves between the satellite and the ground target. Consequently, the propagation speed is modified creating a delay on the interferometric phase. C-band satellites are mainly impacted by the tropospheric layer creating a non-dispersive delay dependent on the temperature, pressure, and water vapor of the atmospheric layer. L-band satellites are also impacted by the ionospheric layer creating a dispersive delay in function of the microwave frequency.

The heterogeneous refractivity distribution in the atmosphere creating a noise effect on the interferogram is called the Atmospheric Phase Screen (APS). Its definition is, according to Jolivet *et al.* (2011): "spatiotemporal variations of the refractivity of air can introduce a change in the measured interferometric phase".

Atmospheric correction

To correct the atmospheric impact, the characteristics of each layer crossed at the time of the acquisition have to be taken into account: humidity, temperature, pressure, and velocity different from the speed of light ($V_i = \frac{c}{n_i}$) of each section.

To obtain this information, the HRES-ECMWF (High-RESolution) global meteorological model at 0.1-degree and 6h resolutions is used and produced by the European Center for Medium-Range Weather Forecast (ECMWF). Global atmospheric reanalysis are methods to produce climate data sets. It is created by an unchanging data assimilation scheme and model which acquired observations every 6h over a specific period. The goal is to estimate the evolution of the global atmosphere state by computing basic upper-air atmospheric fields (temperature, wind, humidity, ozone, surface pressure), followed by separate analysis of near surface parameters (2 m temperature and 2 m humidity), soil moisture and soil temperature, snow, and ocean waves. The HRES-ECMWF reanalysis is produced following a 12-hourly analysis cycles and has a 4D-Var analysis (four-dimensional variational data assimilation technique). Altitude, temperature and water vapor partial pressure are available at 37 pressure levels and for surface until 50 km of altitude (Jolivet *et al.* (2011)). It contains two grids: one computed every 6 hours with an estimation of 3D meteorological variables covering the troposphere and the stratosphere, and one every 3 hours with several surface parameters (weather description, ocean-wave, and land-surface conditions). As meteorological variables are computed only every 6h, an interpolation of the data is realised to coincide with the acquisition time of the images useful for the interferogram.

The atmospheric component has a major impact on the interferometric phase, especially in mountainous area and during the summer, the decorrelation between topography and deformation is hard to determine. For instance, while estimating small displacement such as interseismic movement with low amplitude and long wavelength deformation characteristics due to strain accumulation, the effect of an APS not corrected can have a huge impact on the unwrapped phase (Gourmelen *et al.* (2010); Yu *et al.* (2020)). APS variations from one image to another can produce major phase fluctuations and modify until several centimetres the deformation results. For multi-temporal applications, an accurate estimation and compensation of the APS has to be done as a pre-processing step in any DInSAR techniques.

3.2.5 InSAR time series analysis

Interferograms are affected by turbulent atmospheric errors and topography correlation at short or long wavelengths which are impacting the deformation signals in

InSAR deformation map. One solution to decorrelation is the use of Time Series (TS) analysis aiming at retrieving temporal displacement from a stack of differential interferograms. These techniques are generally called Multiple Images DInSAR algorithms (Ferretti *et al.* (2000, 2001); Berardino *et al.* (2002)).

Two main categories of InSAR TS exist: Persistent Scatterers (PS) Interferometry (PSI) (Crosetto *et al.* (2016)) developed by the Politecnico di Milano (Ferretti *et al.* (2000, 2001)) which requires PS (stable reflectors within the resolution cell that dominate the back-scattered signal in every interferogram of the set), and Small BAseline Subsets (SBAS) (Berardino *et al.* (2002)) developed by the Instituto per il Rilevamento Elettromagnetico dello Ambiente (CNR-IREA) which are both based on finding coherent pixels over a period.

PSI is mainly used over cities as "natural" PS are rare in vegetated areas. PS are usually man-made objects (buildings, bridges, exposed rocks, etc). PS-TS is based on the dispersion of amplitude of the employed image pixels. Targets are selected when returning an ideal isotropic response. Using PS enables to maximize the signal to noise of resolution cells containing a single dominant scatterer. The targets are characterized by a high stability of the response signal. The advantages of this technique, as shown by Crosetto *et al.* (2016), are that it has a wide area coverage associated with a relatively high spatial measurements density and a high sensitivity to small deformation.

SBAS TS uses Distributed Scatterers (DS) which are scatterers presenting a good coherence in several interferograms of the network. DS are usually identified from homogeneous ground, desert areas or non-cultivated crops. SBAS is related to the coherence. DS are analysed implying a phase averaging on the original interferogram. As the coherence is a truthfully indicator of the phase quality, a lower number of images is necessary in comparison with PS technique. SBAS technique uses the more correlated areas to derive the deformation signal from multi-looked interferograms. Even if a reduction of the spatial resolution is associated with this technique, the speckle is reduced, and the phase estimation is improved.

In this thesis, TS-SBAS approach is used, and the rest of this section will focus on its description. A SBAS differential algorithm is applied to obtain the time-dependent deformation map (Mora *et al.* (2002)).

A refined stack of unwrapped interferograms is inverted to get the cumulative displacements and estimate the mean linear velocity map as well as the estimation of the velocity standard deviation. In some cases, gaps in the interferogram network (due to refinement after unwrapping or coherence loss) or gaps on a pixel-by-pixel basis can be present. This approach can improve the redundancy of measurements which mitigates temporal and geometrical decorrelations.

For a stack of T-unwrapped and atmospherically corrected interferograms L generated from Q images acquired at $(t_0, \ldots, t_{Q-1})$, Q-1 incremental displacement vector $d = [d_1, \ldots, d_{Q-1}]^T$, with d_1 the incremental displacement between time t_0 and t_1, least square based TS algorithm is used to estimate time dependent deformation, each interferogram pixels follow equations 3.9 & 3.10 (Yu *et al.* (2020)):

$$L_{ij} = X_{ij} + \frac{4\pi b_{ij}}{\lambda\theta} * X_{DEM} + \epsilon \tag{3.9}$$

$$\mathbf{L} = \begin{bmatrix}\mathbf{D} & \mathbf{C}\end{bmatrix} \begin{bmatrix}\Phi \\ X_{DEM}\end{bmatrix} \tag{3.10}$$

L_{ij}: Atmospherically corrected phase observation;
$X_{ij} = \Phi_j - \Phi_i$: Cumulative displacement from the earthquake rupture at t_0;
X_{DEM}: Digital Elevation Model error;
D_{TxQ}: Coefficient matrix of the cumulative displacement;
C_{Tx1}: Coefficient matrix of the DEM error;
ϵ: Errors (including temporal decorrelation, orbital error, thermal noise effect and atmospheric error);
b_{ij}: Perpendicular baseline;
λ: Wavelength;
θ: Incidence angle.

InSAR time series can be fitted by different functions depending on the displacement analysed: linear function or logarithm function (such as used for the postseismic deformation): $A + B * ln(t - t_0)$ with A and B constants and t the time in years since the earthquake.

For linear constraint, the previous equation 3.9 becomes (between date d_i and d_j):

$$L_{ij} = X_{ij} + (d_i - d_j) * X_v + \frac{4\pi b_{ij}}{\lambda\theta} * X_{DEM} \tag{3.11}$$

For logarithmic constraint, it becomes:

$$L_{ij} = X_{ij} + \ln(d_i - d_j) * X_v + \frac{4\pi b_{ij}}{\lambda\theta} * X_{DEM} \tag{3.12}$$

3.3 Optical Imagery

3.3.1 Optical sensor

Optical imagery can also be used to monitor the globe, they are passive sensors such as SPOT or Sentinel-2. This type of sensor needs the energy of the sun to work, there are sun-synchronous which means they can only return images during daylight. The energy is reflected by the Earth or absorbed and re-emitted towards the satellite (as shown in Figure 3.9). Optical sensors are making observations of visible light and infrared rays and cannot penetrate cloud cover. They are composed of several types of radiometers which measure the intensity of electromagnetic radiation in specific selected bands, and spectrometers which are detecting and analysing the spectral content of reflected electromagnetic radiation. An analysis of the ground surface, the sea surface temperature and vegetation for instance can be measured. Optical products output amplitude images and have a nadir looking geometry. The characteristics of the principal optical satellites are presented in Table 3.2.

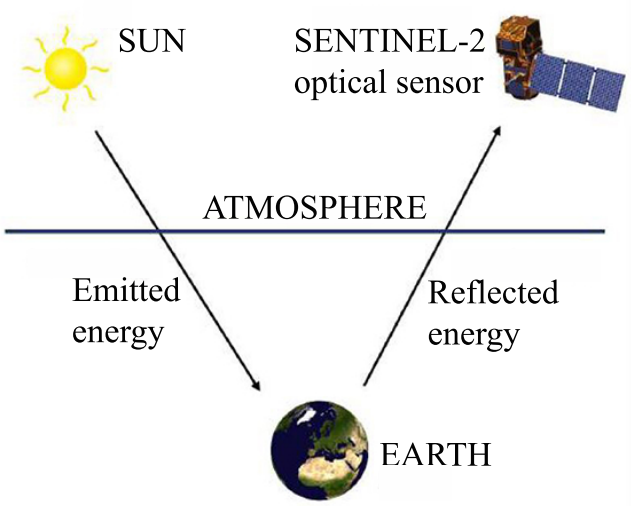

Figure 3.9: Principle of a passive sensor.

Table 3.2: Characteristics of optical satellites.

Mission	Inclination	Revisit	Altitude	Swath	Resolution
SPOT 1-7	98.7°	26 days	822 km	60 km	20 to 1.5 m
LANDSAT 7-8	98.2°	16 days	705 km	185 km	30 to 15 m
SENTINEL-2	98.5°	5 days	786 km	290 km	10, 20, 60 m

3.3.2 Sub-pixel correlation

The principle of optical images correlation is similar to the one of SAR images. The correlation of two optical images gives a measure of the horizontal displacement (two components East and North) on the Earth surface with a sub-pixel resolution. It cannot achieve cm or mm precision as SAR imagery gets using the phase.

In this study, SPOT-1&2 images were processed using COSI-Corr (Coregistration of Optically Sensed Images and Correlation (Leprince *et al.* (2007); Ayoub *et al.* (2009))) software. Figure 3.10 shows the workflow to process the images (set up by Stanford university). This section will be focused on describing the successive steps to obtain the correlation of optical images, specifically for our coseismic study.

- **Inputs**: The inputs for COSI-Corr are SPOT (Pleiades or ASTER can also be processed) panchromatic and multi-spectral images of level-1A. Ancillary files are computed containing the positions, altitudes, and look directions of the satellite acquiring the images and some information about the resolution and structure of the file. Finally, a DEM is needed.

- **Co-registration and ortho-rectification**: Image coregistration is the first step of pixel correlation that consists in super-imposing two or more images in such a way that for each image, the same pixel corresponds to a specific point

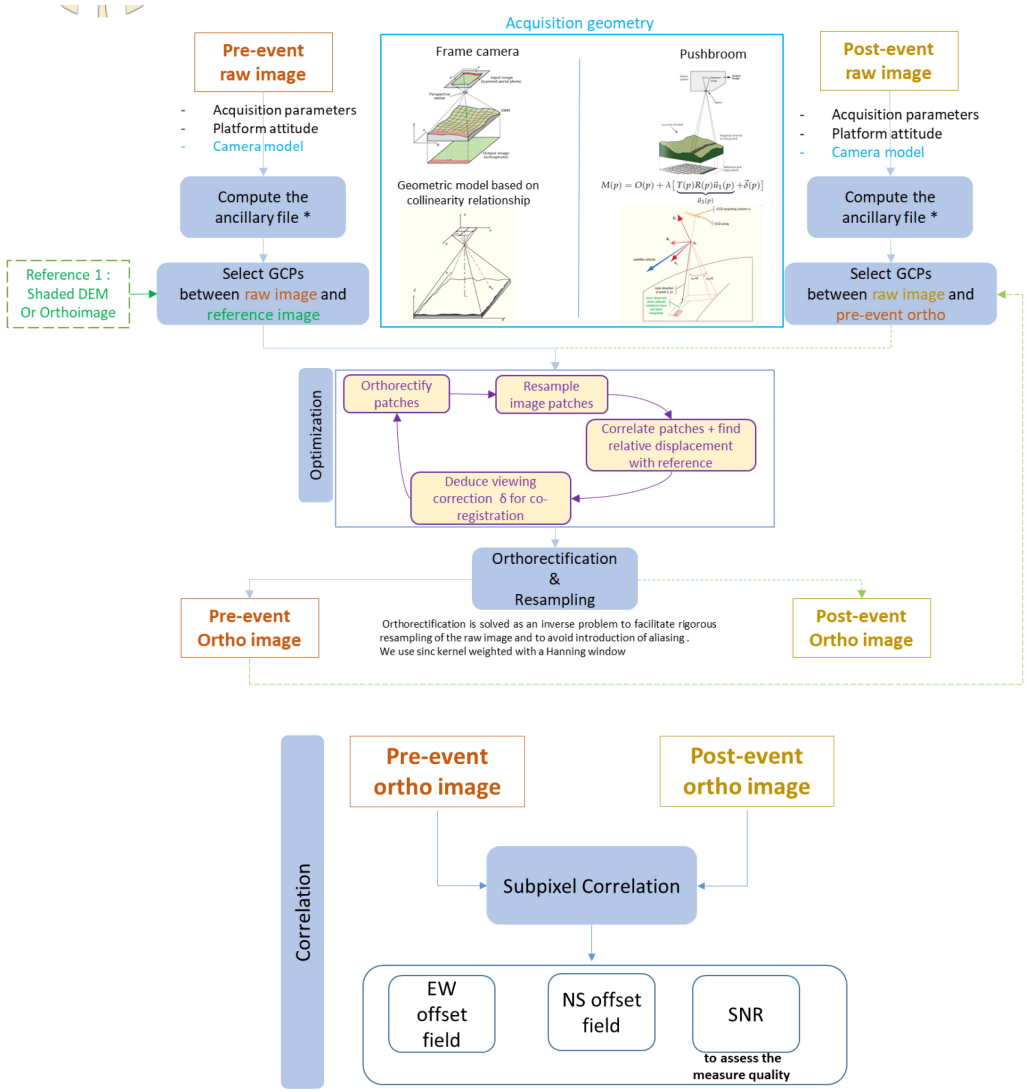

*Ancillary file regroups the meta data from the sensor into one single file to be used during the processing.

Figure 3.10: Workflow for COSI-Corr processing (Provided by Saif Aati, Stanford University).

of the ground. In contrary with SAR coregistration which image correlation is necessary due to the look angle of the satellite, optical image correlation will detect similar pixels on two images acquired at different times in order to detect the shift of the homogeneous pixels.

To refine the absolute geolocation of image 1 (the pre-event one), Ground Control Points (GCPs) points are used: either by GPS (Global Positioning System) campaign or by taking Tie-Points (TP) between the image and a geolocalized reference (for the first image, a shaded DEM is used). The TP

selection consists of pairing points between an ortho-rectified (geometrically corrected from the topography effect) image and a raw one. The TPs are then converted into GCPs and optimized if necessary (even if the TPs are selected carefully, some mis-registration can be present).

A Digital Elevation Model (DEM) and the ancillary files are used to assist these steps.

- **Correlation of the 2 co-registered and ortho-rectified images**: A map of the relative displacements is obtained and composed of three bands: E-W displacement map (positive towards East), N-S displacement map (positive towards North) and a Signal to Noise Ratio (SNR) assessing the quality of the measure.

3.3.3 Image correlator softwares

Several correlators exist to measure ground surface deformation from multi-temporal images. In this work, two were tested: COSI-Corr and Mic-Mac.

The main software used in this thesis for sub-pixel correlation of optical images is COSI-Corr, more details will be presented in Chapter 4. COSI-Corr is a free add-on Envi (Harris Geospatial Solutions) using IDL (Interactive Data Language) developed by the Tectonics Observatory of Caltech with main objective being to retrieve coseismic ground displacements from primary and secondary images around an earthquake. COSI-Corr is based on frequency-domain correlation i.e. the relative displacement is obtained from phase difference of their Fourier transforms. It possesses a graphical user interface and a statistical correlation function. However, with frequency-domain correlation, a correlation window size too small will be critical and increase the correlation noise.

MicMac (Multi Images Correspondances par Méthodes Automatiques de Corrélation (Pierrot-Deseilligny & Paparoditis (2006))) is an open-source software implemented by IGN (Institut National de l'Information Géographique et Forestière) principally dedicated to photogrammetry for 2D or 3D modelling. It has a command line interface. The correlation is realised in the spatial domain. MicMac is the only correlator with a statistical correlation function which uses a multi-scale technique with a regularization algorithm (technique enabling to get good outputs using small correlation window). According to Rosu *et al.* (2015), MicMac is the only correlator than can provide satisfactory results in difficult cases thanks to its regularization algorithm and non-linear correlation cost which are less vulnerable to noise. It could produce smoother results with less noise than COSI-Corr's and gives more accurate displacement values as smaller windows can be used.

The analysis of the coseismic deformation was realised using COSI-Corr, the non-negligeable RMS present in the far field (while comparing with GPS data) made me curious of testing MicMac to see if more precision could be achieved. Sub-pixel detection being largely dependent on the quality and noise level of the data. Even

if the results were slightly smoother using MicMac, a small difference was present in the outputs that were under-estimated (in comparison with GPS data) with both softwares. I decided to continue this work using COSI-Corr as the platform enables to do the entire study, MicMac only possesses the correlation tool.

3.4 Global Navigation Satellite System

Global Navigation Satellite System (GNSS) is a general term describing any satellite system that provides positioning, navigation, and timing (PNT) on a global or regional basis. The most known and used one is the Global Positioning System (GPS), which was established by the Department of Defense (DoD) of the United States (Teunissen & Montenbruck (2017)). Nowadays, it is publicly available and used largely not only for navigation purposes but also for the atmospheric and environmental monitoring. An increasing number of permanent stations are installed all over the globe and many campaigns take place each year to monitor the land. The purpose of any GNSS system is to provide location and time through any weather condition anywhere in the world and at any time. GNSS data are used in many applications, from navigation and tracking for civil or military, study of the atmosphere to surveying and geodesy (tectonic plate motion, Earth surface activities such as landslides or volcanoes). A short description of existing systems is presented in Table 3.3. In the next section, a brief description of GPS (other systems are similar) system will be given (the processing was done at National Taiwan university).

Table 3.3: GNSS systems with global coverage.

GPS	GLONASS	BeiDou	Galileo
Global Positioning System	GLObal NAvigation Satellite System	China Satellite Navigation Office	
United Stated	Russia	China	Europe
1993	1993	2012	2016
24 satellites	24	27	30

3.4.1 System architecture

A GPS system is composed of three segments, namely *Space segment*, *Ground segment* and *User segment* (Teunissen & Montenbruck (2017)). The *Space segment* includes a constellation of 24 satellites available at all time and arranged over 6 orbital planes, and their functioning. GPS satellites are evolving on geostationary orbits meaning that they are following the rotation of the Earth, at an orbit of about 20 200 km and an inclination of 55° with respect to the equatorial plane. They cover twice the whole Earth each day. The trajectory of satellites enables any

station on the ground to receive at least 4 satellites at any time. Satellites are constantly transmitting ranging signals on two or more frequencies towards receiving devices. The *Control segment* is a global network of stations present on the ground, they check the transmissions and analyse the signal to send back commands such as re-synchronisation of clocks and rectification of orbits. Finally, the *User segment* includes receivers and users receiving the data from each satellite to calculate the geolocation of antennas.

Thanks to these three components, the GPS position can be calculated (latitude, longitude, and height) anywhere in the world, at any time and through whichever meteorological conditions. However, some errors that will be described at the end of this section, make the mm theoretical precision hard to reach.

3.4.2 Signal structure

A GPS satellite has on board an atomic clock and its signal is continuously emitted over several frequencies in the L-band domain of the radio spectrum propagating at the speed of light and are modulated by codes. Each signal is composed of ranging codes and navigation data to enable the user to determine the travelling time between the satellite and the receiver as well as the satellite position at any time. The signal is composed of the *Carrier* that is the radio frequency sinusoidal signal, the *ranging code* that is a sequence of 0 and 1 that enables to determine the travel time and *navigation data* providing information on the satellite ephemeris (position and velocity of the satellite), clock bias parameters, satellite health status, etc.

3.4.3 GPS observables

To determine the receiver position, the triangulation principle is applied. Three satellites are necessary to locate an object (x, y, z coordinates) by knowing his distance with three reference points. A fourth satellite is required to get the altitude. To obtain the measurement required, the time needed for the GPS signal to travel between the satellite and the receiver is saved. By multiplying this time by the speed of light, the distance or range is obtained. The GPS signal contains several ranging codes that allow users to compute the travelling time. A correlation of the received code with a replica of the generated phase enables to determine the travelling time.

The determination of the receiver position can be done by *Pseudorange* measurement: measurement of the distance and time between the satellite and receiver antennas and clocks.

The *Carrier-phase measurement* is a more precise method (about two orders) but ambiguous by an unknown integer number of wavelengths. It is a measure of the phase difference between the received signal and the receiver-generated carrier signal at the reception time. Here, the distance is expressed as the sum of the total number of full and fractional carrier cycles multiplied by the carrier wavelength, a

cycle being a full carrier wave. An ambiguity is the ambiguous integer number of cycles in the carrier phase measurement. A comparison of the emitted signal and the received one enables to measure the phase shift which gives the distance between the operator from the satellite until mm precision.

Finally, *Doppler measurements* based on the Doppler effect can also be used to determine the velocity vector of the user. It is a phenomenon of frequency shift of the signal caused by the relative motion of the emitter and receiver.

3.4.4 Errors

Several GPS errors impact the signal. First, errors due to the satellite system (ephemeris, clocks, etc.). Ephemeris errors (order of 3 cm (El-Rabbany (2002))) are due to the difference between the actual and expected orbital position of the satellite.

Then, errors due to the receiver (clocks, multipath, noise, etc.). Multipath is a phenomenon happening when the GPS signal reaches the receiver via two or more different paths due to reflection on structures i.e. a distortion of the amplitude and phase of the direct-path signal. Also, each satellite has an atomic clock on board to precisely know the time of transmission and each receiver has an inexpensive crystal clock less accurate. An error due to the clock synchronisation can induce a 30 cm shift for a slight shift of 1 ns (Cornwall *et al.* (2008)).

Finally, errors linked to the atmosphere (troposphere and ionosphere). As presented in Section 3.2, the waves are crossing several layers of the atmosphere with different characteristics which vary the propagation speed of the wave across the troposphere. The ionosphere is impacted by solar radiation modifying the propagation speed as well. In contrary to C-band satellites commonly used in InSAR, GPS L-band satellites are mainly impacted by the ionosphere.

3.4.5 Atmospheric corrections

Furthermore, GPS measurements are useful for InSAR atmospheric corrections as explained in detailed in Yu *et al.* (2017*b*). Differential interferometry and GPS are both measuring a temporal delay of the electromagnetic signal propagation between the captor and the target, and their signals cross the different layers of the atmosphere. Atmospheric delays measured by GPS can be used to compensate the atmospheric artefacts in interferograms.

3.4.6 Coordinate system

In our study, several types of data set are used and coming from different sources. It is important to define all coordinates in the same reference system. Kovalevsky & Mueller (1981) defines the reference system and reference frame as: “A reference system is a set of prescriptions and conventions together with the modelling required to define at any time a triad of coordinate axes.

A reference frame realizes the system by means of coordinates of definite points that are accessible directly by occupation or by observation."

The International Terrestrial Reference Frame (ITRF) is the most common one. Most of the data coming from National Taiwan University used in this thesis (Levelling and Benchmarks) are defined in the TWD67 reference frame while InSAR and GPS are in the coordinate system WGS84 aligned with the ITRF97.

3.5 Summary

In this chapter, the basic knowledge of the main Earth observations used in this thesis are described: SAR interferometry, optical imagery and GNSS (specifically GPS in this case). Principles and processing steps as well as error sources were presented.

The large availability and variety of data enable to study each phase of earthquake deformation: the high temporal resolution of GPS data and its mm precision enable to study slow and fast displacements; SAR and optical data have a high spatial density and sub-cm precision providing more information over large areas. Using the variety of data in this study enables to compensate the weaknesses (sparse spatial distribution of GPS data and low temporal sampling rate of SAR and optical images depending on the satellites available) of one data over an area or period with the strengths of another one. However, the processing of each data type is complex and requires precise methodology or techniques.

The study of the coseismic deformation will use the estimation of displacements from several data sets to build geophysical models: constrain of the fault geometry and estimation of the slip distribution. GPS and InSAR measurements have proved their potential to determine fault plane geometry as well as slip distribution, and more generally to understand earthquake hazards. InSAR and optical offsets are efficient to study strain rates over large areas. Small deformation signals over long wavelengths can be studied through time series, a continuity in the data is important and can be improved by using GPS. For longer term monitoring purposes such as post- or inter-seismic motions, InSAR time series analysis over several years allows the precise corrections of atmospheric delay, DEM error and orbital error of the deformation signal to achieve a mm/year precision. In addition to the study of GPS TS, the high precision of GPS data enables a validation of InSAR TS. TS will be extracted from InSAR and GPS to study the postseismic deformation, the afterslip and the viscoelastic relaxation mechanisms will be analysed.

The current work is conducted for methodological improvement in combining EO data sets in the general purpose of surface deformation in the context of earthquake cycle. In Chapters 4 and 5, these techniques will be applied for co- and post-seismic deformation.

Chapter 4

Coseismic Study of the Chi-Chi Earthquake

The work presented in this Chapter 4 was previously published in "Roger, M., Li, Z., Clarke, P., Song, C., Hu, J.-C., Feng, W. & Yi, L. 2020 Joint inversion of geodetic observations and relative weighting - the 1999 Mw 7.6 Chi-Chi earthquake revisited. Remote Sensing 12 (Roger *et al.* (2020))". The dissertation author is the primary researcher and conducted all the processing and analyzes of this paper, whilst the co-authors listed are the main author's supervisors, who directed the research, helped to design the logic flow of the paper, and fine-tuned the English. The other co-authors procured data and scripts for the modelling. The paper was reformatted in this chapter.

4.1 Introduction

The Chi-Chi earthquake occurred on 21^{st} September 1999 with a magnitude of M_w 7.6 and at a depth of 33 km (according to USGS: 23.772° N 120.982° E)). It was the most destructive inland earthquake of the 20^{th} century happening in Central Western Taiwan. The seismic moment was estimated at 3.046 x 10^{20} N $\cdot$ m by the USGS with a mean slip of 2-3 m. Thousands of people were injured or killed, and many infrastructures were destroyed. During the three months following the event (Ma *et al.* (2001)), thousands of aftershocks occurred including six with a magnitude greater than 6.5, starting at the north and migrating downward and southward of the main event (Wang (2016)). This earthquake was due to the reactivation of the Chelungpu fault: thrust faulting on a north-south striking fault plane dipping to the east (Lee *et al.* (2001)). The rupture was complex with several dislocations; it reached the surface and created a 100 km-long scarp between the hanging-wall to the east and the footwall to the west (Pathier *et al.* (2003)). From GPS data (see Figure 4.1), a clear change of surface motion is visible at the north end of the fault turning towards east. According to the focal mechanism, this event is in agreement with the SE-NW plate convergence motion (Lee & Chan (2007)), with an overlap towards

west linked to the orogen deformation and a double plate convergence boundary, on each side of the Central Range (Angelier *et al.* (2001)).

In this study, I used five types (see Figure 4.1) of geodetic observations (GPS, levelling, benchmarks of urban planning, InSAR and SPOT offsets) in a joint inversion in order to estimate the slip distribution with and without precise estimation of the relative weights. In previous models, non-negligible residuals are present due to lack of information (density of the GPS network and no coherence on the hanging-wall for InSAR). This study focuses on showing the importance of combining and using complementary data sets rather than improving the model geometry. The fault geometry was determined by previous studies and slightly modified as a result of our data. The method presented in this paper shows the impact of different data sets on the slip distribution as well as the necessity to properly determine the relative weights.

4.2 Geodetic Data Sets and Processing

The use of geodetic observation data is efficient for the study of earthquakes because of their high precision and their complementarity. In this study, several types have been selected: GPS, ERS-SAR and SPOT-optical images, levelling and benchmarks. GPS data have a high temporal resolution and a precision less than 1 mm/yr useful to study slow deformation such as the postseismic phase but it can also be used to study fast deformation such as the coseismic phase; however their spatial distribution is sparse. Levelling and benchmarks have also an high spatial precision (few cm or higher) but rely on field measurement campaigns. InSAR data have a high spatial density and sub-cm precision but a low temporal sampling rate depending on the satellite (for instance, 6 days for Sentinel-1A/1B satellites but 35 days for ERS). Finally, SPOT images have a similar spatial density to SAR images, but can often provide useful measurements despite vegetation where SAR images lose coherence and at higher density than a pixel offset map estimated from the SAR amplitude would give. Even though the study area is partially covered by dense vegetation making InSAR output non-coherent, the joint study of InSAR with correlation of optical images and terrestrial measurements is an efficient and precise way to understand earthquakes. In Central Western Taiwan, from InSAR outputs, information about the footwall of the fault is obtained and SPOT offsets cover the full study area more densely than GPS. Levelling and benchmarks give precision about vertical movements and about the curved part at the north of the fault as benchmarks were measured only in this area (Figure 4.1.B-C respectively).

4.2.1 GPS measurements

The GPS network in Taiwan was installed in 1989 and has been surveyed since 1990 covering the whole island. Figure 4.2 shows benchmarks and an antenna of the Taiwan network. Specifically for the coseismic study (see Figure 4.1.A), the

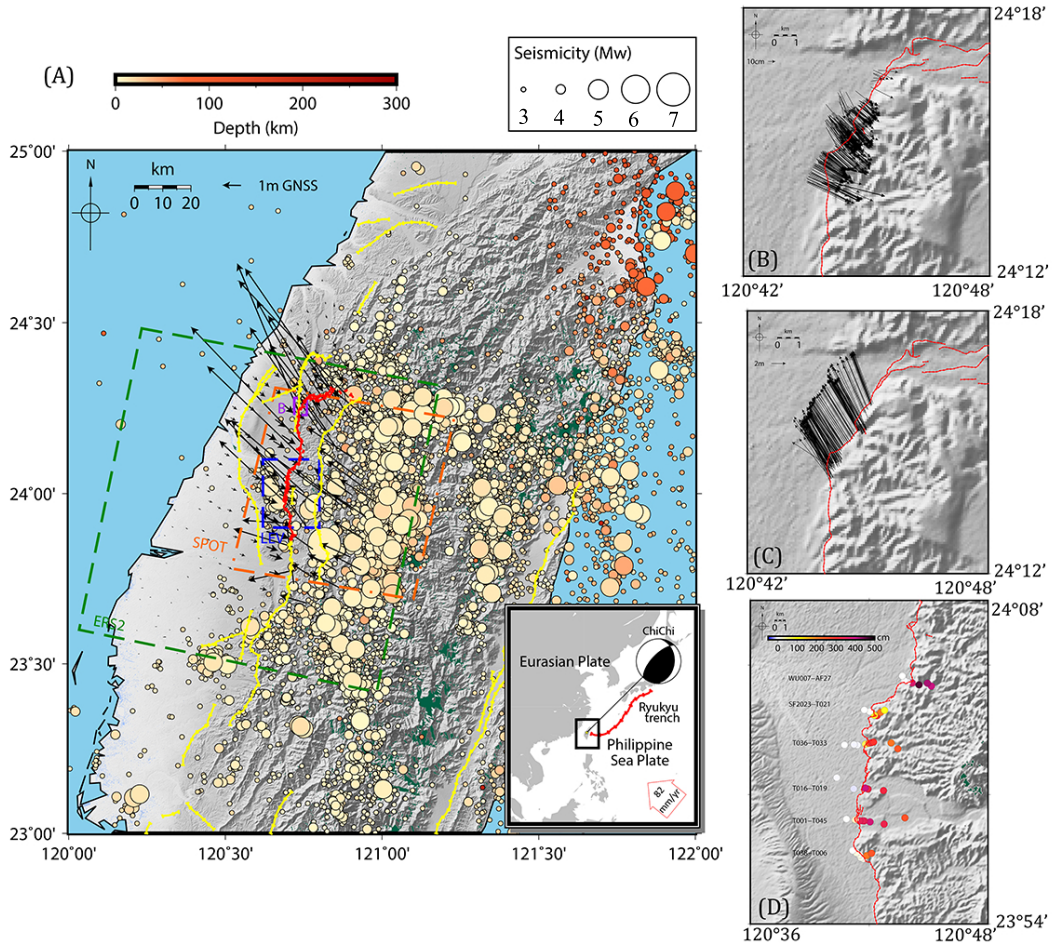

Figure 4.1: (**A**) Geodynamic map of Taiwan. The Chelungpu thrust fault is shown in red (source J.-C. Hu from National Taiwan University) and the other faults in yellow (source J.-C. Hu from National Taiwan University). Focal mechanism of the Chi-Chi earthquake on the inset map. Seismicity (from 1998 to 2000, source J.-C. Hu from National Taiwan University) over Taiwan. GPS displacement vectors (Yu *et al.* (2001)) shown by black arrows. Green dashed box shows the location of the ERS-2 scenes from descending track 232, orange dashed box shows the location of the SPOT satellite images used in this study. The purple dashed box is the location of the benchmark data, results are presented in (**B**) for the footwall displacements and in (**C**) for the hanging-wall displacements (notice the different scale). Finally, the blue dashed box is the location of the levelling data, results are presented in (**D**).

displacements were extracted from Yu *et al.* (2001) (who did all the processing and corrections stated in this section). 41 permanent stations are available (operated by the Central Weather Bureau (CWB); the Satellite Survey Division and Land Survey Bureau, Ministry of Interior (MOI) and the Institute of Earth Sciences, Academia Sinica (IESAS)) and 101 campaign-surveyed stations (conducted by three institutions (the Central Geological Survey, Ministry of Economic Affairs (MOEA, CGS); MOI and IESAS)) covering 1992 to 1999. They separated pre- and post-seismic deformation to estimate the coseismic displacement due to the Chi-Chi earthquake. Yu *et al.* (2001) processed the GPS data using Bernese software v. 4.0 and corrected with precise ephemerides, and residual tropospheric zenith delays were estimated by least squares. The reference station selected is Kinmen, located on the east coast of mainland China ($\sim$ 257 km from the epicenter) which did not show any coseismic movement. Furthermore, the pre-seismic secular motions were corrected by interpolating the velocity of 24 stations observed from 1992 to 1999. Finally, postseismic displacements were corrected from the coseismic displacements at the stations surveyed during the three months following the earthquake by interpolation from the nearby stations (Johnson *et al.* (2001)). GPS, benchmarks and levelling are well correlated with each other.

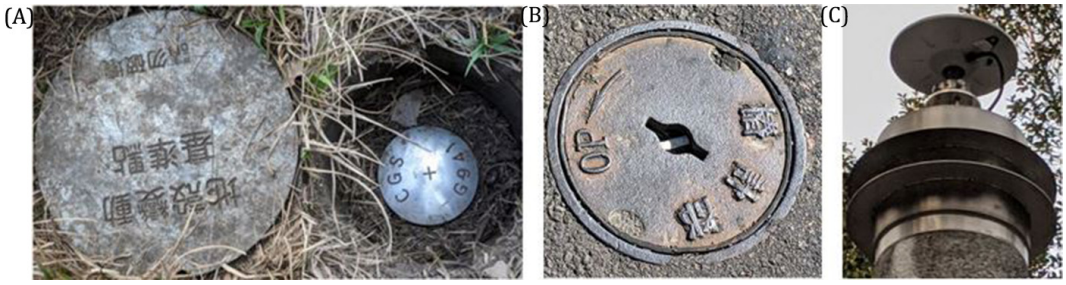

Figure 4.2: (A) Levelling and (B) geodetic benchmark in Taichung city, Taiwan and (C) a GPS antenna in Puli City, Taiwan. [Photo credit: Marine Roger]

In addition to GPS data, benchmarks of urban planning (Huang *et al.* (2008)) situated at the north part of the fault, in Fengyuan city, were used (locations shown by the purple dashed box in Figure 4.1.A and the displacements on the footwall and hanging-wall in Figure 4.1.B-C respectively). The pre-earthquake benchmarks were measured by total-station and the survey after the earthquake is a mixture of total station trilateration/triangulation and GPS campaigns. The horizontal positions were estimated by total station trilateration/triangulation. The data were provided with respect to the origin of TWD67 System (Transverse Mercator Two-degree Grid system) that I converted to WGS84 (World Geodetic System 1984) to be consistent with the rest of the data sets. The densely spaced distribution of the city-planning benchmarks provides an accurate location of constructions. Before the earthquake, a city map was created giving accurate position of human constructions. As many constructions were damaged during the earthquake, a second survey was run to remap

the city after the event, the new map contains all the old city-planning benchmarks as well as Chi-Chi earthquake surface ruptures. The coseismic horizontal displacement data set was extracted from the comparison of these two maps. The horizontal displacements present an uncertainty of 1-2 cm against a mean displacement of 5 m in this area for the coseismic displacements.

4.2.2 Levelling data

In addition to GPS data, levelling measurements (locations shown by the dark-blue dashed box in Figure 4.1.A and the displacements in Figure 4.1.D) were procured by CGS (MOEA) from 1998 to 2002 and converted from TWD67 to WGS84. They give more information about the vertical displacement, and are consistent with the GPS. Two of the six levelling lines are presented in Figure 4.3.

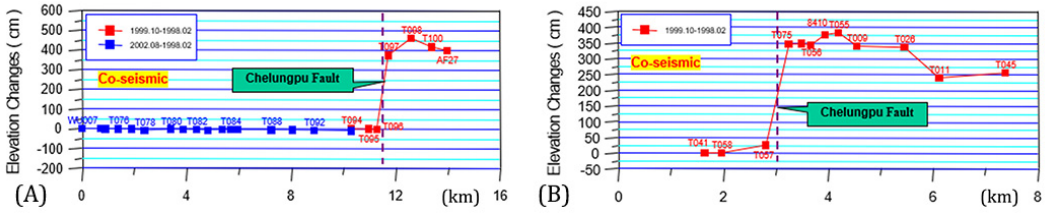

Figure 4.3: Levelling deformation profiles of 2 lines: (A) WU007-AF27, (B) T001-T045. See Figure 4.1.D for profile locations.

4.2.3 InSAR: ERS-2 interferometric processing chain

ERS images were interferometrically processed using the ESA (European Space Agency) open-software SNAP (Sentinel Application Platform). Their parameters are presented in Table 4.1 and their coverage shown in Figure 4.1.A. Only the footwall of the fault could be analysed on the interferograms. The hanging-wall, which experienced the main deformation during this event, is densely vegetated resulting in low coherence. Coseismic interferograms show about 11-13 fringes in the footwall which is equivalent to a surface displacement of up to 37 cm (the estimation is approximated due to the low coherence and is based on the number of fringes) (Figure 4.4).

Three interferograms were processed using SNAP and SNAPHU (Statistical-cost, Network-flow Algorithm for Phase Unwrapping Chen & Zebker (2000, 2001, 2002)) for unwrapping the phase (the interferograms are consistent to each other with a regression coefficient of 0.7-0.8). After the coregistration of the primary and secondary images using Delft orbits and a 30 m SRTM (Shuttle Radar Topography Mission) DEM (Digital Elevation Model), the interferograms were formed and multilooked

Table 4.1: ERS-2 data used in this study.

Acquisition date	Track	Frame	Orbit	Temporal baseline [days]	Perp. baseline [m]	Height ambiguity [m]
28/10/1999	232	3123	23633	-	-	-
21/01/1999	232	3123	19625	280.00	-92.89	102.07
06/05/1999	232	3123	21128	175.00	20.08	-469.46
15/07/1999	232	3123	22130	105.00	-247.71	38.28

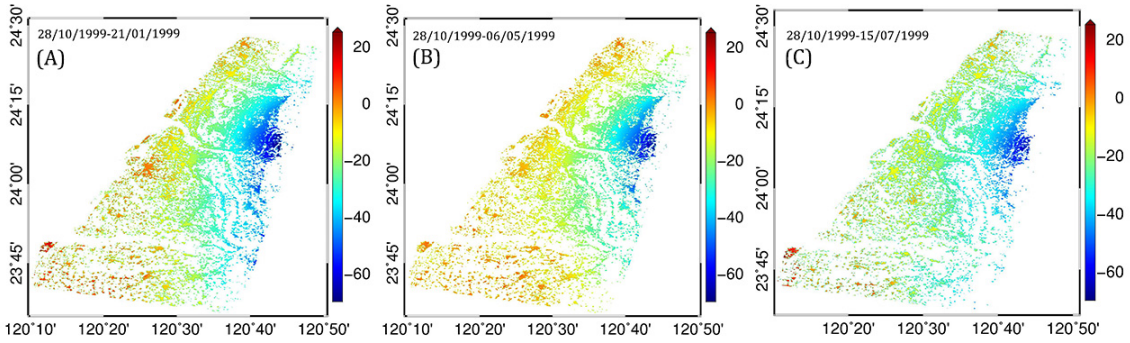

Figure 4.4: Interferograms of the Chi-Chi earthquake (color bar in cm) as presented in Table 4.1, the primary image is on 28/10/1999. (A) 28/10/1999-21/01/1999. (B) 28/10/1999-06/05/1999. (C) 28/10/1999-15/07/1999.

by 4x20 m to reduce the phase noise, which gives a ground resolution of about 80 m. Finally, the interferograms were corrected for the effects of topography using the 1 arc-second (30 m) resolution SRTM DEM and filtered using Goldstein filtering (an adaptative power spectrum filter Goldstein & Werner (1998)) before unwrapping the phase and geocoding. Only pixels with a coherence higher than 0.2 were kept to be used in the joint inversion. The low coherence was the main challenge of the InSAR processing especially for the unwrapping of the phase. Furthermore, the hanging-wall of the fault, which is covered by dense vegetation, presents the main deformation as shown by GPS data. Thus, the main area of the deformation is not visible on the interferograms. Due to this reason, I decided to use optical images in addition to the radar interferometry. They have a better spatial resolution (10 m) than pixel offsets from InSAR (about 20 m) and will give me information about the deformation on both sides of the fault.

4.2.4 Sub-pixel correlation of SPOT images

In order to obtain observations of the hanging-wall, the COSI-Corr (Co-registration of Optically Sensed Images and Correlation) software was used to correlate pre- and

Table 4.2: SPOT data used in this study, resolution 10 m and right orientation.

Acquisition date	**Satellite**	**Cloud cover**	**Incidence angle**	**Orient. angle**	**Sun elevation**	**Sun azimuth**
29/01/1999	SPOT-2	10%	2.9°	9.4°	42.9°	151.0°
23/11/1999	SPOT-1	0%	2.5°	9.4°	43.4°	159.7°

post-earthquake optical images. SPOT satellite panchromatic images were processed to determine the horizontal coseismic displacement using the subpixel correlation technique (Van Puymbroeck *et al.* (2000); Michel *et al.* (1999)). In this study, I used SPOT 1-2 images with a 10 m resolution and with the lowest cloud coverage (see Table 4.2). The location of the SPOT images are showed by the orange dashed box in Figure 4.1.A. The pre-earthquake image is from 29 January 1999 and 2 months following the event for the second image (23 November 1999). In order to minimize uncertainties in the correction of topographic effects, I selected images covering the area with near-vertical incidence angle (2.9° for the pre-earthquake image and 2.5° for the post one). I used a Tandem-X DEM with a spatial resolution of 12.5 m for the processing as the resolution of the images is 10 m (InSAR resolution is 80 m). Even though the images selected are covering 8 months before the event and two months after, no significant pre-seismic deformation was present on the GPS observations and only a few cm of horizontal postseismic deformation, so it can be considered that the offsets are essentially representing the coseismic displacements (Dominguez *et al.* (2003)).

In order to obtain the ground deformation, SPOT pairs were processed using COSI-Corr. It is a module developed in IDL (Interactive Data Language) and integrated in ENVI (Environment for Visualizing Images) by the Caltech Tectonics Observatory (USA). The methodology allows an automatic and precise orthorectification and coregistration of satellite images (Leprince *et al.* (2007)). The main steps of the procedure are an ortho-rectification of the primary image with Tandem-X DEM due to precise selection of ground control points (GCPs), then ortho-rectification of the secondary image using GPS data values in the far field to correct for long wavelength bias. An optimization is applied to improve the ortho-rectification: reduction of the mis-registration unavoidable from the manual tie points selection by optimizing the GCPs of the secondary image (iteration until ground offset between the primary and secondary images is negligible). Finally, the subpixel correlation of the pre- and post-event ortho images leads to three bands (East-West (see Figure 4.5.A) and North-South offset fields (see Figure 4.5.B)), and the Signal-to-Noise ratio from which the horizontal ground displacement is retrieved.

For the joint inversion, I only kept pixels with a Signal-To-Noise Ratio (SNR) above 0.1 and removed the area covered by clouds. An RMS (Root Mean Square) of about 1 m and 1.7 m for the E-W and N-S components respectively is present between GPS and SPOT offsets (see Figure 4.6) mainly due to the different number

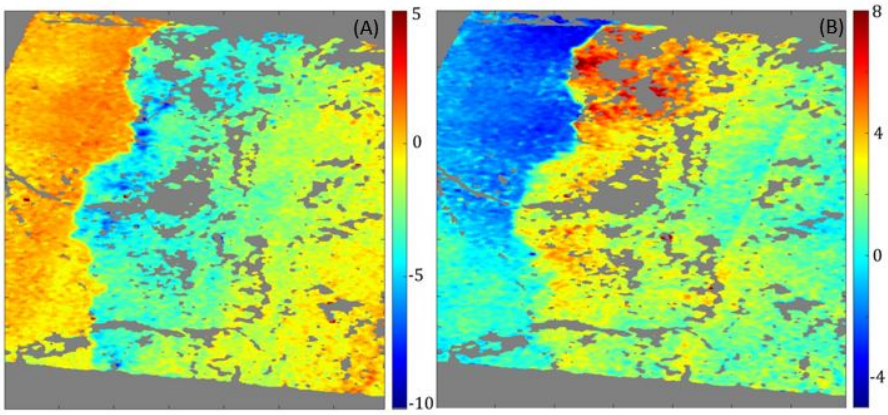

Figure 4.5: **(A)** & **(B)** East-West and North-South horizontal offsets obtained from the sub-pixel correlation of the two SPOT images (see Table 4.2) acquired before and after the earthquake (scale in m). Grey areas are where the correlation was too low (Mean and standard deviation for EW band: -1.5 m, 1.7 m and for NS band: 1.2 m, 1.9 m).

of points and the issues in the far field. For the modelling, points in the far fields are excluded. Long-wavelength artifacts are observed on the offsets (see Figure 4.5), mainly for the North-South image, due to satellite attitude changes.

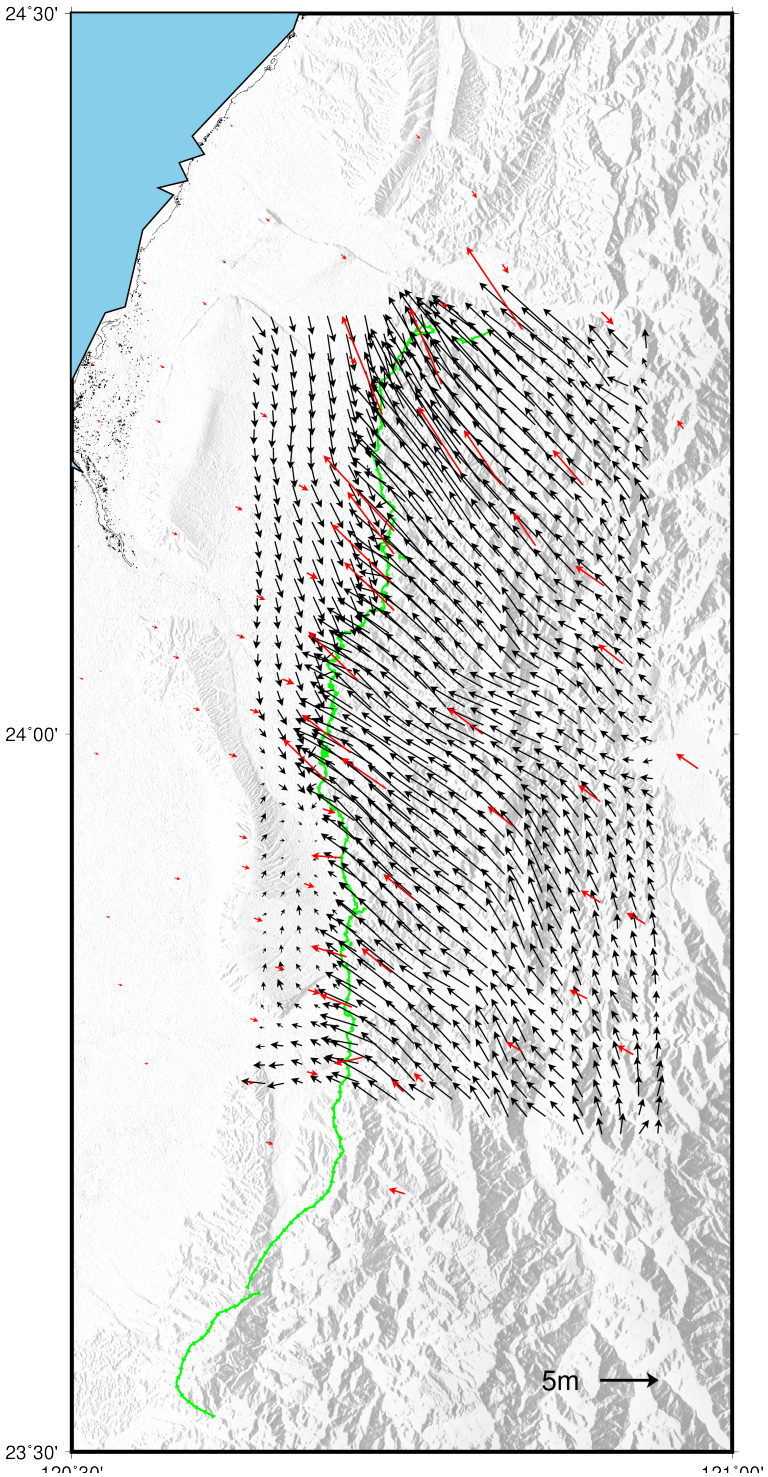

Figure 4.6: Coseismic displacement vectors, black arrows represent SPOT offsets and red arrows GPS data.

4.3 Earthquake Modelling

Okada's dislocation theory (Okada (1985)) has been generally used to study and invert seismic fault displacements. However, it only works under the assumption that the Earth crust is a homogeneous elastic half-space and for near-field observations, as the Earth's curvature and radial heterogeneity are not taken into account in Okada's equations. This standard dislocation model calculates an analytical solution for ground deformation due to shear and tensile faults. The fault is modelled by a rectangular geometry (defined by length, width, depth, strike, dip and 3-component dislocation amplitude (rake, slip and opening)) which is decomposed into small dislocation patches. This theory will be used to determine the slip distribution in this study.

From previous models available for the Chi-Chi event in the literature as presented in the introduction of this paper, inconsistencies are observed between rupture processes of the earthquake using one or multiple types of observations. For instance, inconsistencies due to the quality of the data sets: low density of GPS points and low coherence of InSAR, non-negligible residuals between observations and model or the type of dislocation model used introducing overlaps and gaps. The proposed method in this paper combines five data types in a joint inverse model and thus requires a precise estimation of relative weighting of each data set. In that objective, the generalized Akaike's Bayesian Information Criterion (gABIC) is used.

Furthermore, before estimating the relative weights and inverting the data, in order to make the computation feasible and efficient, InSAR observations are often down-sampled to limited numbers of points (from several thousand points to a few hundred). The Quadtree method (Jonsson *et al.* (2002)) was used and displacement gradients are used to determine the sub-sampling window size. Before this, a linear trend is removed from the interferograms (to remove the orbital ramp).

4.3.1 Generalized Akaike's Bayesian Information Criterion

A precise weighting of each data set is fundamental to realize the joint inversion. These weightings strongly affect the result of the inversion (as explained in Funning *et al.* (2014)). For instance, an over-weighting of one data set could induce an under-weighting of the other data sets and disturb the estimation of each parameter of the fault geometry. In that goal, the weight determination method developed by Yi *et al.* (2017, 2018) is used: the Generalized Akaike's Bayesian Information Criterion (gABIC) based on the entropy maximization principle (Akaike (1973)) to determine the regularization parameter (a spatial constraint used to regulate the rupture process), and the Bayesian theorem to estimate the probability distribution of the slip for given observations (GPS, benchmarks, levelling, InSAR, SPOT offsets) and prior constraints (Laplacian constraint in our case). In this generalized version, the type of observations and prior constraints do not need to be specified; only diagonal covariance matrices have to be estimated before running gABIC script.

As I have 8 sets of (pseudo-) observations (3 interferograms, GPS, benchmarks,

levelling and SPOT offsets in addition to the Laplacian constraint), 7 hyperparameters need to be determined using the search-based gABIC method. To obtain optimal weight ratios that minimize the ABIC value, large enough ranges of these hyperparameters have to be considered. In practice, searching the seven data sets with a small enough interval is highly time consuming. In order to reduce the processing time, a first estimation of each relative weight was done by calculating it for each data set in respect with the GPS one, which covers the whole area with a low uncertainty. For this first step, the weighting range was determined using a power law method (10^x) and then refined using a linear method (x) for the interval of inputs (x representing the values to test). Once the interval of hyperparameter was reduced, gABIC could be applied using several data sets at once.

The inversion equations (Yi *et al.* (2018)) are the following (to make the equations more manageable, only one interferogram is mentioned):

$$\mathbf{d} = \mathbf{Ha} + \mathbf{e} \tag{4.1}$$

$$\mathbf{0} = \mathbf{Sa} + \boldsymbol{\epsilon} \tag{4.2}$$

With:

- $\mathbf{d} = [\mathbf{d}_{GPS}\ \mathbf{d}_{Ben}\ \mathbf{d}_{lev}\ \mathbf{d}_{SAR}\ \mathbf{d}_{Sp}]^T_{Nx1}$: Nx1 vector containing 5 data types (respectively [GPS, Ben, lev, SAR, Sp] for GPS data, Benchmark, Levelling, Radar Interferometry and SPOT offsets) (total N observations);
- $\mathbf{H} = [\mathbf{H}_{GPS}\ \mathbf{H}_{Ben}\ \mathbf{H}_{lev}\ \mathbf{H}_{SAR}\ \mathbf{H}_{Sp}]^T_{NxM}$: NxM coefficient matrix;
- $\mathbf{S} = [\mathbf{S}_S]^T_{PxM}$: PxM coefficient matrix containing Prior constraints;
- $\mathbf{a}$ is a M dimensional model parameter vector that varies with the time windows;
- $\mathbf{e} = [\mathbf{e}_{GPS}\ \mathbf{e}_{Ben}\ \mathbf{e}_{lev}\ \mathbf{e}_{SAR}\ \mathbf{e}_{Sp}]^T_{Nx1}$ & $\boldsymbol{\epsilon} = [\boldsymbol{\epsilon}_S]^T_{Px1}$:
  are vectors of the Gaussian-distributed uncertainties of observations and constraints, respectively.

Furthermore, $\mathbf{e} \sim \tilde{\boldsymbol{Q}}(\sigma_i^2)$ where $\tilde{\boldsymbol{Q}}(\sigma_i^2) = \sigma^2_{GPS}$ with $\mathbf{Q}$ (i refers to the five data sets) covariance matrices of observations and a similar equation for the constraint). The covariance matrix $\mathbf{Q}$ is expressed as follows (*blkdiag* means block diagonal matrix):

$$\mathbf{Q} = blkdiag\left[\tilde{\boldsymbol{Q}}_{GPS} \quad \left(\tfrac{\sigma^2_{Ben}}{\sigma^2_{GPS}}\right).\tilde{\boldsymbol{Q}}_{Ben} \quad \left(\tfrac{\sigma^2_{lev}}{\sigma^2_{GPS}}\right).\tilde{\boldsymbol{Q}}_{lev} \quad \left(\tfrac{\sigma^2_{SAR}}{\sigma^2_{GPS}}\right).\tilde{\boldsymbol{Q}}_{SAR} \quad \left(\tfrac{\sigma^2_{Sp}}{\sigma^2_{GPS}}\right).\tilde{\boldsymbol{Q}}_{Sp}\right]_{NxN}$$

The ABIC function was first introduced by Yabuki & Matu'ura (1992), using only static GPS observations and Laplacian spatial constraint, as:

$$ABIC = N \cdot log\ s(\mathbf{a}^*) - M \cdot log\ \alpha^2 + log||\mathbf{H}^T\mathbf{E}^{-1}\mathbf{H} + \alpha^2\mathbf{G}|| + log||\mathbf{E}|| - log||\mathbf{S}^T\mathbf{S}|| + N(log(2\pi) - logN + 1) \tag{4.3}$$

gABIC is the generalized version, it searches for the hyperparameters (σ_i^2) that minimize the ABIC value as presented in Yi *et al.* (2017):

$$ABIC = N \cdot log\ s(\mathbf{a}^*) - M \cdot log\ \alpha^2 + log||\mathbf{H}^T\mathbf{E}(\sigma_i^2)^{-1}\mathbf{H} + \alpha^2(\mathbf{S}^T\mathbf{S})\boldsymbol{\Delta}(\epsilon_i^2)^{-1}|| + log||\mathbf{E}(\sigma_i^2)|| - log||(\mathbf{S}^T\mathbf{S})\boldsymbol{\Delta}(\epsilon_i^2)^{-1}|| + N(log(2\pi) - logN + 1) \tag{4.4}$$

Where:

- $\alpha^2 = \left(\frac{\sigma_{GPS}^2}{\epsilon_S^2}\right)$ is the smoothness parameter;
- ϵ_i is a hyperparameter representing the weight of the constraint;
- $s(\mathbf{a}) = (\mathbf{d} - \mathbf{Ha})^T\mathbf{Q}^{-1}(\mathbf{d} - \mathbf{Ha}) + \alpha^2\mathbf{a}^T(\mathbf{S}^T\mathbf{S})\boldsymbol{\Delta}^{-1}\mathbf{a}$

4.3.2 Modelling strategy: fault geometry and slip distribution

Regarding the fault geometry (see Table 4.2), this study was based on the previous model designed by Johnson *et al.* (2001); Johnson & Segall (2004) and adjusted in accordance with the more recent literature as described in the introduction. Johnson & Segall (2004) is in agreement with the geologically constrained fault model of Yue *et al.* (2005). Mainly, the decollement subfault was adjusted: especially the depth, dip and the rakes of each sub-fault according to the inversion of our data sets. The decollement was fixed arbitrarily to be wide enough so that insignificant slip occurred at one edge of it. Furthermore, for segments 2 and 3, I tried to avoid as many gaps and overlaps as possible. The purpose of the study was to test gABIC on a complicated but known case including several data sets, not to determine the most precise fault geometry. However, for more precision and physical reality a triangular dislocation model would be necessary. Poly3d will be used in a future work (Maerten *et al.* (2014)).

Under the assumption of an elastic homogeneous half-space, the fault geometry and the slip distribution are determined following a 2-step approach using the Particle Swarm Optimization and OKada INVersion package (PSOKINV). It is a geodetic inversion package (Feng *et al.* (2013)) developed in Matlab which can solve linear and nonlinear problems. Multiple geodetic data sets can be handled by the program.

Table 4.3: Fault geometry parameters used in this study and the ones from Johnson *et al.* (2001) & Johnson & Segall (2004) [from SRCMOD: Earthquake Source Model Database (http://equake-rc.info/srcmod/)].

	Length [km]	**Width** [km]	**Depth** [km]	**Dip**	**Strike**	**Rake**
This study						
Segment 1	71.45	30	0	23°	3.3°	62°
Segment 2	10	10	0	22°	50°	90°
Segment 3	15	20	0	24°	88°	90°
Segment 4	70	34	11.7	5.7°	3.3°	54°
Other models						
Segment 1	70	30	0	23° [22-31]	3.3°	?
Segment 2	8.6	30	0	23° [13-30]	35°	?
Segment 3	27 [22-35]	30	0	21° [14-41]	88° [49-94]	?
Segment 4	70	?	[5.8-8.6]	$[0-7]°$	88°	?

First, a nonlinear inversion is performed to determine the fault geometry parameters (location, strike, dip, rake, length, width, depth and slip) minimizing the square misfit under the hypothesis of a uniform slip on a rectangular fault using the multi-peak particle swarm optimization (M-PSO) (Feng & Li (2010)), a non linear algorithm approach based on the elastic Okada dislocation models (Okada (1985)). The slip distribution is then determined as a linear problem, and optimally-smoothed parameters are obtained based on a conjugate gradient least square method. The dip angle is particularly sensitive to the data. Hence, as the non-linear step is a first order approximation, the dip angle is refined during the second step by studying the relationship between weighted model misfits and multiple dip angles. When all the parameters are optimally determined, the fault plane was discretized into rectangular sub-patches of 2 km x 2 km (Figure 4.7).

4.4 Data Set Weighting

4.4.1 Benefit of multiple data sets

The Chi-Chi earthquake is a particularly interesting event to work on a joint inversion methodology as it has been well studied already, its fault geometry is quite stabilised and the island is well monitored so a large variety of data sets is available from satellite images (ERS and SPOT) to field measurements (levelling, benchmarks, GPS in our case).

As explained previously, geodetic observations were selected with their advantages and disadvantages but presenting a good temporal and spatial complementarity. Figure 4.8 presents the slip distribution obtained for each data set alone

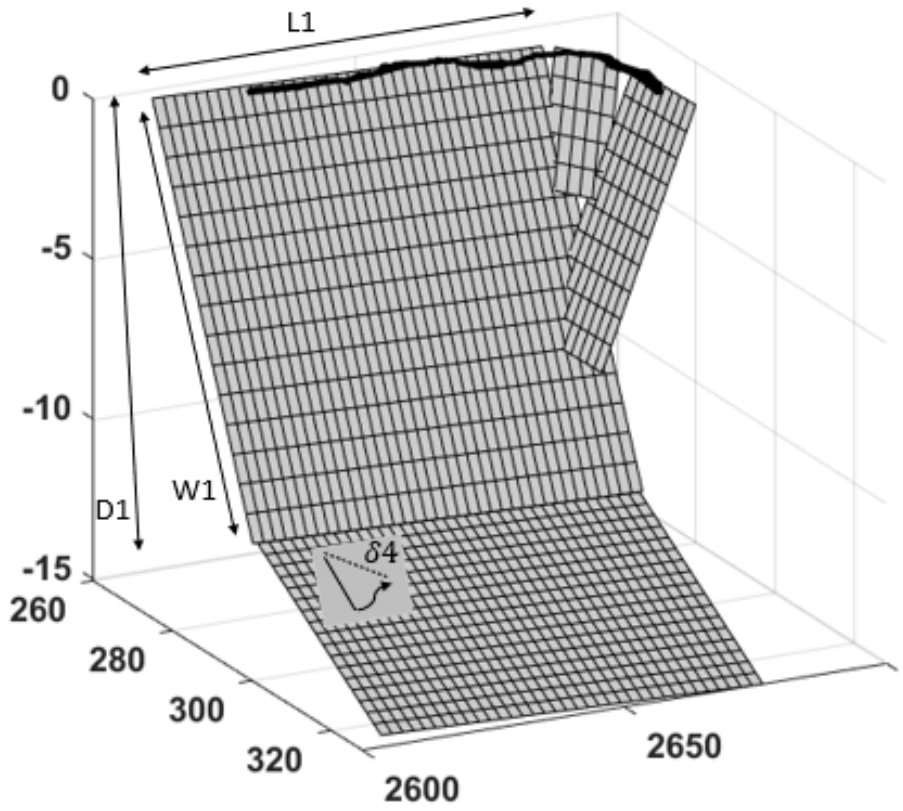

Figure 4.7: Fault geometry used in this study (Table 4.3).

to see its impact to the overall slip distribution. For the GPS based slip distribution (see Figure 4.8.A) and adding benchmark and levelling data (see Figure 4.8.B), similar patterns as the one presented in Johnson & Segall (2004) are observed. The maximum of slip occurs near the surface at the northwestern edge of the fault and negligible slip is present below 10 km depth. The contribution of benchmark and levelling data sets in addition to GPS is useful to get more information in the curved part (where the slip has the highest magnitude and where the geometry of the fault may not be optimal). A shallower slip distribution is visible in comparison to GPS alone (especially subfaults 2 and 3) and I obtain more precision about the vertical movement. From InSAR observations (the result from the interferogram 28/10/1999-15/07/1999 is presented in Figure 4.8.C), the slip is under-estimated in comparison with GPS data due to the asymmetrical distribution (only covering the footwall) of the interferograms. This is also why I do not observe any signal on the decollement at depth. Finally, Figure 4.8.D, from only SPOT offsets, is not over- or under-estimating the slip but showing more deformation at depth mainly due to the large uncertainties in the far field.

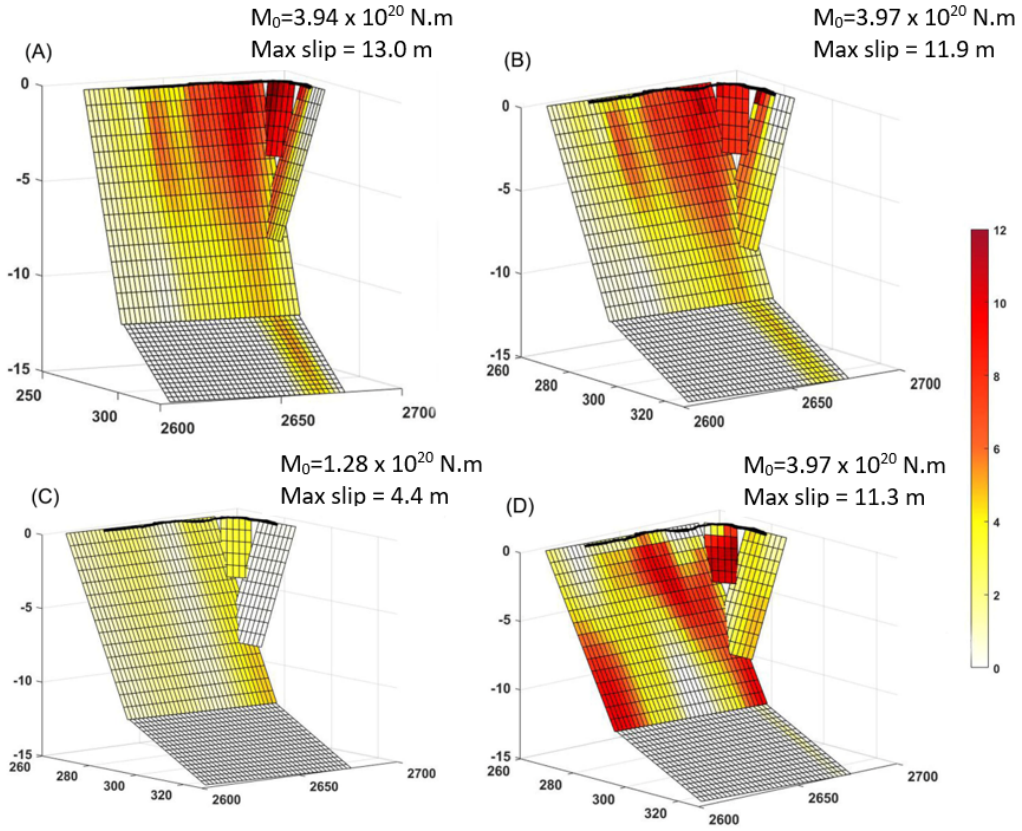

Figure 4.8: Slip distribution model for 4 sub-faults geometry for the Chelungpu fault (scale bars in m). Inversion (Correlation coefficient, RMS (m)) based on **(A)**. GPS only (0.96, 0.39); **(B)**. GPS, benchmarks and levelling (0.57, 3); **(C)**. One interferogram (15/07/1999) (0.90, 0.03); **(D)**. SPOT offset only (0.91, 0.90). The colour scale saturates at 12 m. M_0 is the total seismic moment for each model.

4.4.2 gABIC impact

It is essential in the joint inversion to determine the relative weights between the different data sets and the constraint to properly balance the contributions of each of them. The difference with previous studies is the use of the generalized formula of the ABIC method (Akaike (1973)) from Yi *et al.* (2017) (gABIC) to be able to take into account any type of data sets without need of specification and different type of constraints. The point of using gABIC is to obtain a precise value for the weight of each data set that is used for the estimation of the slip distribution. The main issue with this method is that it is computationally intensive. In order to reduce the processing time, the following strategy was followed. First each data set was run separately with the GPS as reference to estimate the relative weight of this data set in relation to the GPS. Then, when a first estimation was made, I run all data sets together by restricting the search intervals.

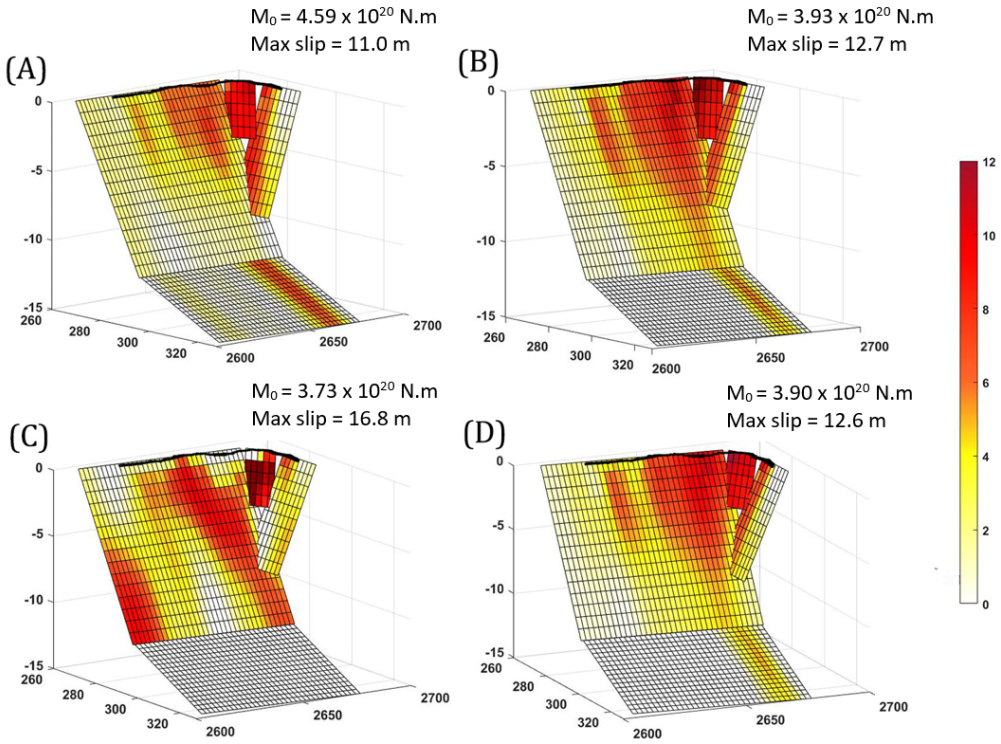

Figure 4.9: Slip distribution models. Inversion based on **(A)** GPS data and three interferograms (4.1) with all the weights set to 1; **(B)** same data sets but with the relative weights estimated by gABIC (GPS 1, 0.09, 0.10, 0.10 for the three interferograms). All the data sets were included in (C) and (D). **(C)** The relative weights are set to 1; **(D)** the relative weights ([GPS, levelling, Benchmarks, Interferograms 1, 2, 3, SPOT]= [1,10^{-4},10^{-4},0.09,0.10,0.10,0.01]) were estimated by gABIC. The colour scale saturates at 12 m. M_0 is the total seismic moment for each model.

The first row of Figure 4.9 presents the slip distribution obtained from GPS and the three interferograms where first all the weights were set to 1 and secondly the weights were estimated by gABIC. The second row is presenting the slip distribution obtained from all the data sets used jointly following the same steps: first the weights were set to 1, then weights were estimated by gABIC.

After the estimation of the relative weights by gABIC, I can see that the slip distributions are smoother, with a maximum of slip at the curve of the fault of about 12 m. No unexpected slip is present on the edge of the fault. The weights for the benchmarks and levelling is low because the spatial extent of the data sets is small in comparison with the other data sets even though their precision is better.

4.4.3 Checkerboard test

In order to examine the geodetic data resolution for the slip distribution on the fault plane, checkerboard tests were conducted using GPS only, InSAR only, SPOT

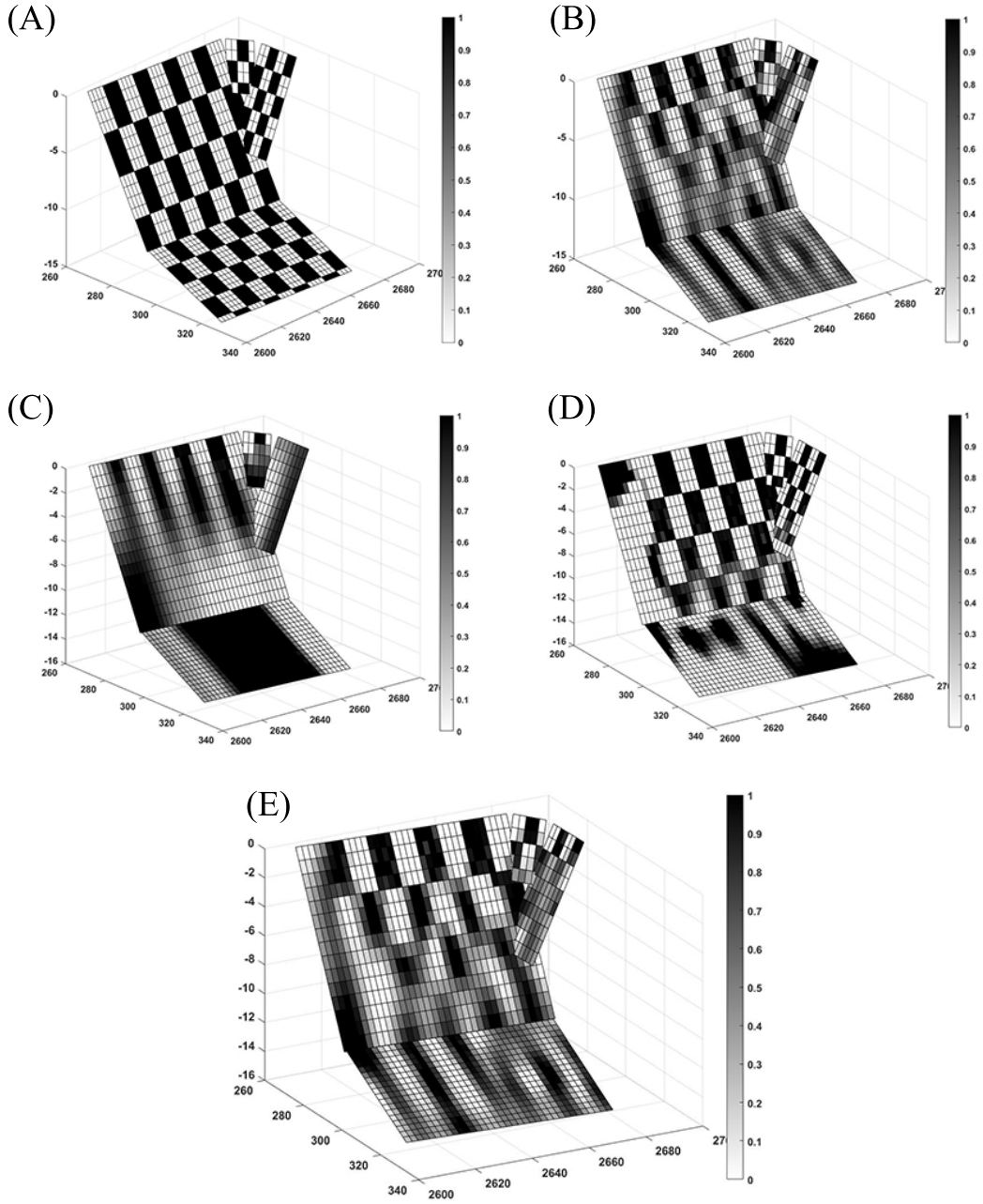

Figure 4.10: Results of the Checkerboard tests. (A) The synthetic slip distribution. (B-E) correspond to the slip solution inverted from the synthetic ground deformation: GPS only, InSAR only, SPOT correlation only and all datasets respectively.

correlation only and finally, all the datasets together (no noise were added to the synthetic geodetic field). Synthetic slips of 0 and 1 m were assigned on different fault patches and then, inverted for the slip solution using the same inversion method as previously detailed in section 4.3.

The checkerboard test results show that the GPS network (Figure 4.10.B) has a better fault slip resolution compared with InSAR and SPOT correlation (Figure 4.10.C & D), especially on the decollement. However, the result from SPOT correlation only has a high model resolution on the curved area at the north of the fault (the high resolution of this result on the shallow part of the fault could be biased by the uncertainties of the SPOT offsets). From the checkerboard test, we can see that InSAR is only helpful for the shallow part of the fault. Generally, the geodetic data have a better resolution at shallow depths.

Comparing the checkerboard test from GPS only and using all the datasets together (Figure 4.10.B & E), we observe an improvement on the main segment of the fault and the segment at the north. However, on the decollement, the fault slip resolution is similar. Our final solution better resolves the fault slip but the GPS data plays an important role in the construction of the slip model for this specific case that is the Chi-Chi earthquake.

4.5 Seismic Hazard

The seismic moment was estimated based on the inverted slip distribution, with a maximum at 3.9 x 10^{20} N $\cdot$ m:

$$M_0 = \mu \cdot S \cdot \delta u \qquad (4.5)$$

μ: Shear modulus taken as 33 GPa;
S: Area of the fault;
δu: Mean slip from strike slip and dip slip.

The seismic moment release was summed for each 2x2 km patch in horizontal rows to obtain the variation in moment release with depth, and summed in vertical columns to get the moment release along strike. The slip distribution and the study of the integrated moment by depth and strike show that the main deformation happened in the north part of the fault, where the fault is curving towards the east with a slip reaching 12.6 m (Figure 4.9.D) and most of the moment was released at depths shallower than 4 km.

To evaluate the effect of the rupture on the surrounding area, the Coulomb Stress Change (CSC) was calculated using Coulomb 3.3 (Graphic-Rich Deformation and Stress-Change Software) USGS software (Toda *et al.* (2005); Lin & Stein (2004)). CSC represents the transfer of stress. It is possible to estimate, from the CSC, the triggering effect of large earthquakes such as the Chi-Chi event. CSC was estimated on a specified fault (strike, dip, and rake specified) at a depth of 11 km with a friction coefficient of 0.4. Figure 4.11 shows that the increase of Coulomb stress is concentrated at the north of the Chelungpu fault and towards the north-east which indicates that most of the stress was transferred to faults at the north of the Chelungpu fault. As presented by Hsu *et al.* (2009), aftershocks (Figure 4.12) mainly occurred down dip from the rupture area which is consistent with the increase of Coulomb stress that I observe in Figure 4.11.A. Figure 4.11.B shows an increase of stress for depth above 10 km which is consistent with the aftershock distribution.

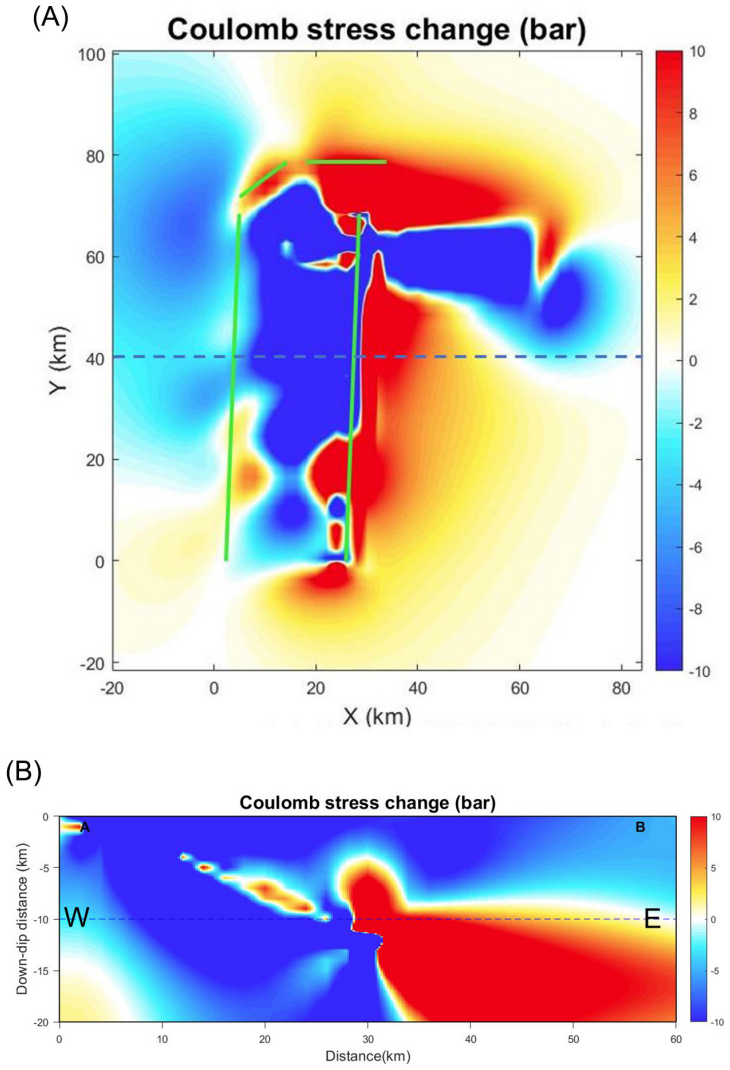

Figure 4.11: (A) Coulomb Stress Changes due to the Chi-Chi earthquake. The green lines are the location of the 4 sub-faults. (B) Cross section with location presented on (A) by the dashed line.

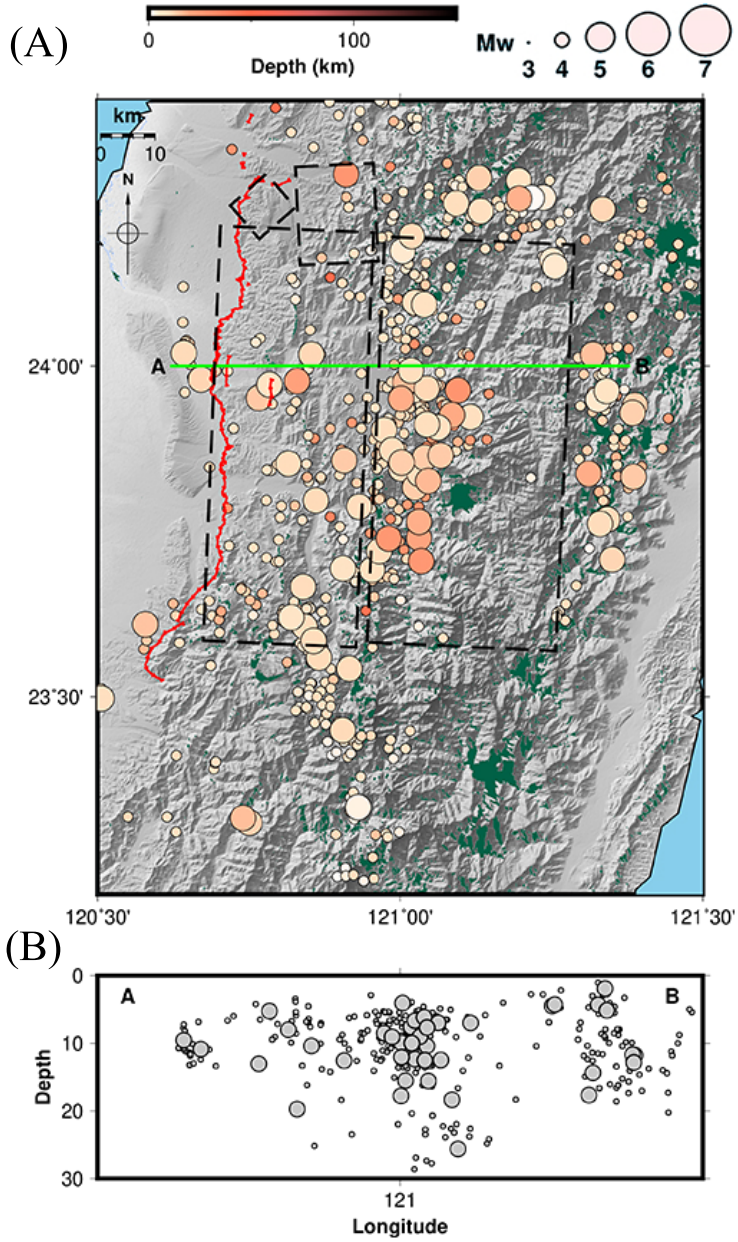

Figure 4.12: (A) Position of the Chelungpu fault (in red) and the fault geometry in black. Dots are representing the aftershocks during the 6 months following the event. Larger dots: $M_w \geq 5$, small ones $3 \leq M_w < 5$. (B) A-B profile showing the aftershocks in depth (m).

4.6 Summary

The Chi-Chi earthquake is a complicated event that was caused by the reactivation of the Chelungpu fault whose geometry is quite complex, and which occurred in a region of steep topography and dense vegetation.

Five types of geodetic observations (GPS, levelling, benchmarks, InSAR and optical offsets) were combined to determine the fault slip distribution of the 1999 Chi-Chi earthquake. A methodology was established in order to precisely estimate the relative weights between the data sets, which is a critical step for the modelling. A wrong estimation will create an under- or over-estimation of the slip distribution. For this purpose, the generalized ABIC formula was applied to estimate the relative weights between the observations and the constraint. The slip distribution is mainly determined by the GPS as presented in previous papers; however the incorporation of other geodetic observations constrains the model especially on the curved part at the north of the fault.

The preferred slip distribution including all the data sets and using the relative weights estimated by gABIC shows that the maximum slip of 12.6 m was on the north curved part of the fault with a seismic moment of 3.9 x 10^{20} N $\cdot$ m, corresponding to a magnitude of M_w 7.6. The study of the moment and Coulomb Stress Changes show that most of the slip happened on the north part of the fault at shallow depths and that most of the energy released by the event was transferred to the faults at the north of the area, which is now the most probable location of a future event.

Revisiting this earthquake was a challenge, as the precision and coverage of the data sets available are quite poor as well as the complexity of the topography and atmospheric conditions. This study enabled to better see which impact each data set has on the model, how and in which condition to use each type and especially how we can join them to use their strengths and overpass their limitations (for instance, vegetated area is non-coherent with InSAR but visible with optical imagery). Most models have been built only using GPS, however precise features of the earthquake cannot be achieved with GPS-only model due to the lack of observation in near-field. This work focused on processing carefully each data set and from the modelling to get more information about the deforming area, the maximum slip and the slip distribution over the different segments of the Chelungpu fault in comparison with locked sections from the interseismic period. The PSOKINV-gABIC approach is viable for the study of complicated cases such as the Chi-Chi earthquake and can significantly benefit from the weight determination and physical realism of the fault geometry.

Future works should consider every type of Earth observation available and realise joint inversion for more precision. In the last decade, satellite images have dramatically improved especially with the Sentinel-1 constellation and the evolution of atmospheric methods, as well as the densification of GPS networks. It is essential to take advantage of all these data, to take into account their quality and coverage

by estimating precise relative weights and thus to establish methodology to precisely monitor Earth deformation.

Chapter 5

Postseismic Study of the Chi-Chi Earthquake

5.1 Introduction

In the introduction of this thesis, the principle of the earthquake cycle was described: it is a combination of a rupture (coseismic phase, described in Chapter 4), afterslip and viscoelastic relaxation (postseismic phase) and a locking period (interseismic phase). Figure 5.1 presents these earthquake cycle processes. The combination of these mechanisms redistributes the stresses all around the fault over the earthquake cycle.

The postseismic deformation is a transient part of the interseismic phase lasting from days to decades after the rupture. Its study is useful to constrain the rheological properties of rocks. It is a complex system composed of several physical processes linked to the redistribution of stress in the crust and upper mantle. Postseismic deformation or strain evolution depends on the rheology of the crust and mantle wedge (a rheology is defined by the properties of the materials, the medium condition of pressure and temperature, and the way materials deform and flow under stress), and the fault geometry and slip distribution of the coseismic rupture. The deformation is time-dependent but also linked to the temperature/pressure conditions (i.e. with an increase of depth, the temperature increases and rocks behave in a ductile way). Furthermore, as rocks are porous and liquid saturated, the stress changes during the coseismic phase induce a flow of pore fluids at the base of transient deformations.

The Taiwan collision is particularly suited for the analysis of the mechanisms governing transient postseismic deformation: dense GPS network, stress perturbation due to the 1999 Chi-Chi earthquake and geological knowledge. Large earthquakes such as the Chi-Chi event are followed by large-scale crustal and mantle deformation that can last up to several decades. Furthermore, the large number of seismic events striking the island every year gives information about the postseismic deformation. However, the quantity of events and mechanisms deforming the lithosphere are also complicating the study of the postseismic phase. Before the event, the seismicity

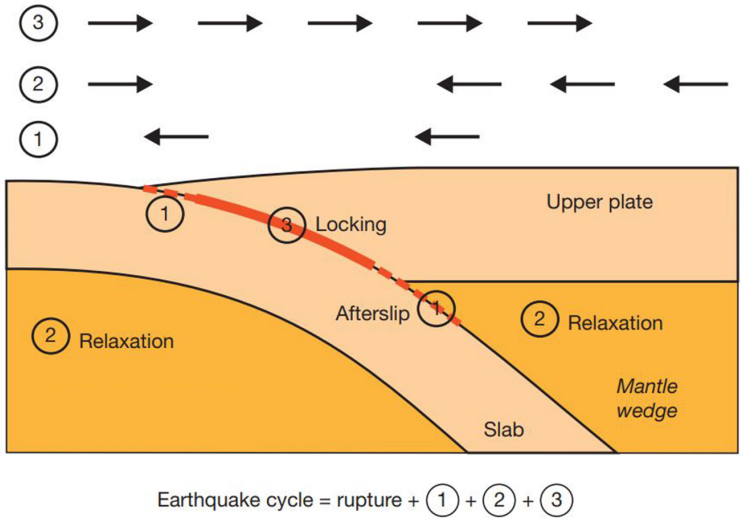

Figure 5.1: Overview of earthquake cycle processes in the case of a subduction event. Numbers correspond to the different phases: (1) aseismic afterslip happening mainly close to the rupture area, mostly around the rupture zone; (2) viscoelastic relaxation happening in the upper mantle which was stressed by the rupture; and (3) locking of the fault after the postseismic deformation. Arrows explain the sense of the horizontal motion of the ground happening during each phase (Figure modified from Wang *et al.* (2012)).

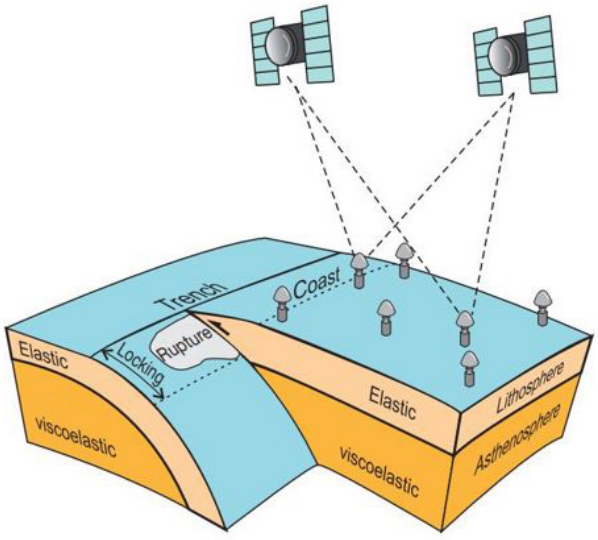

Figure 5.2: Representation of subduction earthquake cycle models. 3D viscoelastic model (Figure extracted from Wang *et al.* (2012)).

distribution of Taiwan is uneven (Figure 5.3.(A)). The east side of the island is particularly struck by earthquakes (due to the subduction of the Philippine Sea plate), at depth above 100 km in the north and at shallower depths towards the south. In the Central Western part of Taiwan, only a few shallow earthquakes of magnitude under 4 happened in the 5 years preceding the event. Figure 5.3.(B), presenting the seismicity from the event to 2010, shows that the majority of aftershocks happened in the south part of the Chelungpu fault and in the south-eastward direction. Several aftershocks including several of magnitude above 5 followed the mainshock starting at the north and migrating downward and southward of the main event, and the majority of seismic events happening after 1999 are for depth above 50 km. Previous studies (Graham *et al.* (2014); Tang *et al.* (2019); Wang & Fialko (2014)) demonstrated that in response to coseismic stress changes, a combination of mechanisms happened in the lithosphere: a continuity of slip happens in the upper layer of the lithosphere (mainly aseismically), fluid flow in the porous rocks (poroelastic relaxation) close to the fault, and viscous relaxation in the lower part of the lithosphere rocks (see Figure 5.2).

Geodetic observations, GPS and InSAR, are powerful tools to map interseismic strain (Takada *et al.* (2018); Tong *et al.* (2013); Wright *et al.* (2001)) and to detect non-linear displacement over time defining the postseismic phase. In this study, both InSAR and GPS are used, GPS has excellent temporal coverage but poor spatial coverage as each GPS station is a single point. Conversely, InSAR has a high spatial coverage but a sparse temporal coverage. So, GPS is better at understanding non-linearity in deformation than InSAR, but InSAR is better at understanding the pattern of deformation. In most cases, only 5 to 10 years of EO are available to study the long-term rate of strain accumulation.

In the case of the Chi-Chi event, we have access to a few years before the earthquake and 20 years of data since to study the postseismic deformation. To explain the processes and both vertical and horizontal movements, a combination of slip and relaxation is needed. Aseismic slip surrounding the main rupture area or viscoelastic relaxation in the mantle alone cannot explain the complexity of displacement following such an event (Chan & Stein (2009)). In this study, a power-law Burgers rheology (Qiu *et al.* (2018); Pollitz *et al.* (2006)) is used to model the postseismic processes (which will be discussed later in this thesis) following the sudden rupture of the coseismic phase (Klein *et al.* (2016)) and take into account contribution from both afterslip and viscoelastic flow. In this study, the effect of poroelastic relaxation was not considered. According to Rousset *et al.* (2012), the maximum displacement predicted from poroelastic relaxation is less than 10 mm corresponding to less than 10% of the observed amplitude in the near field. Hence, it is not dominant, and it will not be considered in this study but this mechanism as well as other micromechanisms can be the cause of residuals in the model. A Burgers body is defined by an instantaneous elastic strain, a long-term viscous strain rate and a transient creep which decreases as a function of time. More details will be given on the rheology in Section 5.2.3.

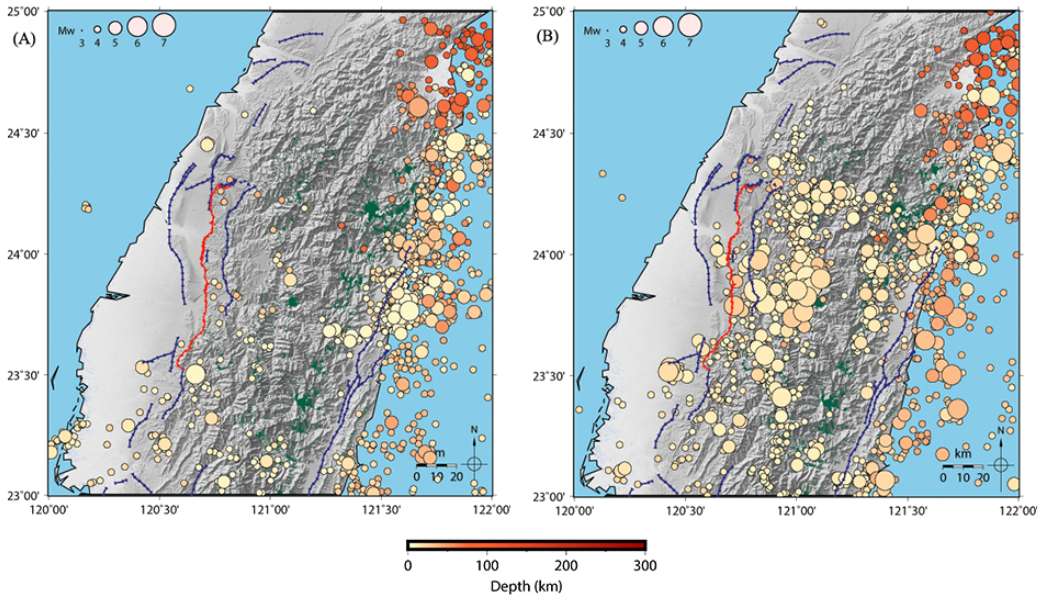

Figure 5.3: Maps of the distribution of seismicity over Taiwan covering (A) 1995 to 19^{th} September 1999 (B) from the 20^{th} September 1999 to 2010. The Chelungpu thrust fault is shown in red and the other active faults in blue (source J.-C. Hu from National Taiwan University).

The goal of this chapter is to analyse the postseismic deformation of Central Western Taiwan during the last 20 years by considering Time Series (TS) from GPS and InSAR and by running a mechanically coupled afterslip-viscoelastic flow Burgers model to analyse the postseismic mechanisms. A few studies were realised in the literature using a shorter period of GPS data such as Hsu *et al.* (2007) covering 15 months of data evaluating the contribution of afterslip and viscoelastic flow. Rousset *et al.* (2012) used 10 years of data to analyse the complex behaviour in time and space of the postseismic deformation. Finally, Tang *et al.* (2019) used 14 years of data to analyse the rheological behaviour of the lower crust. A precise correction of atmospheric and unwrapping errors was realised to enable the use of InSAR data over this area and for the first time, to study the postseismic deformation of the Chi-Chi earthquake using InSAR TS. Furthermore, the modelling of the deformation using a mechanically coupled afterslip-viscoelastic approach enables us to access the status of the deformation and discuss the return to interseismic phase after 20 years of deformation.

First, I will introduce the postseismic deformation theory focusing on afterslip and viscoelastic flow. An analysis of the frictional properties and the viscous structure of the upper mantle will be done. Then, the data sets and processing applied will be detailed. Finally, an analysis of the time series and outputs of the postseismic model will be done.

5.2 Afterslip & Viscoelastic relaxation theory

Around the seismogenic zone (fault areas of major seismic ruptures), different mechanisms are deforming the crust and upper mantle, and different earthquake cycle phases can be detected over some segments of the fault and over different periods. After the sudden stress release of the coseismic phase, a concentration of stress around the earthquake rupture causes an increase of slip in the velocity-weakening regions i.e. afterslip which is usually defined by creep with a velocity faster than the plate rate (the previously locked area has to average the plate rate over the whole cycle). Afterslip (elastic deformation) and viscoelastic flow (non-elastic mechanism) are mechanically connected during a postseismic period but their distributed contributions vary for each event. As explained in Muto *et al.* (2019), these two processes are interacting and diffusing the coseismic stress changes due to the earthquake cycle process. Viscoelastic flow redistributes stress over a distributed area and in deeper layers, and afterslip is increasing the geodetic moment, aseismically. The dynamic of the crust and upper mantle is a complex system of linear and non-linear interactions composed of aseismic displacements near the fault, brittle and ductile flow movements. The system responsive to the coseismic rupture is implying a clear reduction in the effective viscosity during this transient phase (Muto *et al.* (2019)). Several parameters are varying depending on the situation and have to be taken into account while modelling such as pressure, temperature (a study was run by Tang *et al.* (2019) examining the temperature structure under Taiwan using an inverse model with GPS data) or material properties.

A large earthquake is followed by aftershock sequences and transient deformation (over several months) which are both redistributing stresses. Studies discussing the relationship between early afterslip and aftershocks such as Jiang *et al.* (2021) show that faults are creeping aseismically after an event and that a link is observed between afterslip and aftershock rates. They showed that there is a strong correlation between the changes of shallow aftershock rates and stress change history attributed to early afterslip and slip reversal. Usually, an increasing afterslip is followed by larger aftershocks.

5.2.1 Afterslip modelling theory

During short-term deformation, the lithosphere experiences deformation (from 82 mm/yr of relative plate velocity to 12 m of coseismic slip) that can be approximated by infinitesimal strain hypothesis as presented in the coseismic study. A finite length thrust is considered (Okada (1985)) and the theory for computing displacements for general 3D dislocations will be presented.

The displacement field can be described by the following equation (5.1) composed of a first term representing a rigid body translation and a second term representing the displacement gradient tensor. u is the displacement field that describes the change of position of a particle from a reference location x_0:

$$u_i(x) = u_i(x_0) + \left.\frac{\partial u_1}{\partial x_j}\right|_{x_0} dx_j + ... \qquad (5.1)$$

u: displacement field;
x_0: Reference location.

The governing laws of elastic dislocations are the following:

Strain tensor: $$\epsilon_{ij} = \frac{1}{2}\left(\frac{\partial u_i}{\partial x_j} + \frac{\partial u_j}{\partial x_i}\right) \qquad (5.2)$$

Hooke's law: $$\sigma_{ij} = 2G\epsilon_{ij} + \lambda\epsilon_{kk}\delta_{ij} \qquad (5.3)$$

Conservation of momentum: $$\frac{\partial \sigma_{ij}}{\partial x_j} = f_i \qquad (5.4)$$

u: Displacement field;
ϵ_{ij}: Strain tensor;
σ_{ij}: Stresses;
λ and G: Lame constants;
δ_{ij}: Kronecker's delta;
G: Shear modulus;
f: Body force density.

In this section, I am considering a theoretical thrust fault, hence considering a plane strain. In the modelling, a 3D modelling of the fault is realised.

Plane stress is used to define a thin plate, and plane strain when an infinitely long fault in cross-section is considered. In plane stress, it is assumed that one of the principal axes is zero ($\sigma_3 = 0$). This is usually the case in thin flat plates deformed by forces parallel to the plate. In plane strain, direction 3 is considered as infinitely long i.e. $\epsilon_{i3} = 0$. It is usually the case for thrust (or normal) faulting with a sufficient along-strike length, which is the case for the Chelungpu fault (in this case, $\sigma_{33} \neq 0$ corresponding to the restraining stress due to the along-strike material (Barbot & Moore (2019))).

For a dip-slip fault, the following equations are obtained:

$$u_3 = 0 \qquad \text{and} \qquad \frac{\partial u_1}{\partial x_3} = \frac{\partial u_2}{\partial x_3} = 0$$

$$\epsilon_{33} = 0 \qquad\qquad \sigma_{11} = 2G\epsilon_{11} + \lambda\epsilon_{kk}\delta_{11}$$
$$\epsilon_{11} = u_{1,1} \qquad\qquad \sigma_{22} = 2G\epsilon_{22} + \lambda\epsilon_{kk}\delta_{22}$$
$$\epsilon_{22} = u_{2,2} \qquad\qquad \sigma_{12} = 2G\epsilon_{12} + \lambda\epsilon_{kk}\delta_{12}$$
$$\epsilon_{12} = (u_{1,2} + u_{2,1})/2 \qquad\qquad \sigma_{33} = \nu(\sigma_{11} + \sigma_{22})$$

There are 8 unknowns due to two independent equations to solve (2 displacements, 3 stresses and 3 strains), using Einstein summation notation:

$$\mu\nabla^2 u_i + (\lambda + \mu)\frac{\partial u_{k,k}}{\partial x_i} + f_i = 0 \qquad (5.5)$$

The theory to solve this system is detailed in the Chapters 2 & 3 of Segall (2010) and Barbot & Moore (2019).

The deformation of the continental crust is controlled by the mechanisms of faulting. Brittle materials at cold temperature behave elastically when small stress

and strain are applied, and break under large stress. In this case, a thrust fault accommodating horizontal shortening and vertical thickening is studied. Friction is the force resulting from the sliding of rocks (due to the presence of asperities) on both sides of a fault due to relative motion (static friction coefficient for lithosphere rocks: [0.6 0.8]). According to Scholz (1990), the size of the surfaces in contact does not impact the frictional force. The frictional resistance or effective normal stress and the Coulomb friction law can be expressed by equation 5.6 (Barbot & Moore (2019)):

$$\sigma_{eff} = \sigma_n + \alpha p \qquad (5.6)$$

which can be expressed by:

$$\tau + \mu_0 \sigma_{eff} = 0 \qquad (5.7)$$

σ_{eff}: Effective normal stress;
σ_n: Normal stress;
α: Coefficient of effective stress;
p: Fluid pore pressure (positive if under compression);
μ_0: Friction coefficient;
τ: Frictional shear stress.

Friction describes the generation of earthquakes and slow-slip events. The stress-driven afterslip can be modelled with a velocity-strengthening friction law using equation 5.8 (extracted from Teunissen & Montenbruck (2017)):

$$s = S \log\left(1 + \frac{t}{\tau}\right) \qquad (5.8)$$

s: Slip;
S: Multiplicative constant;
t: Time since the earthquake;
τ: Relaxation time depending on frictional properties.

Usually, the spatial pattern of the afterslip displacement is different from the slip happening during the coseismic phase. However, as it primarily surrounds the coseismic slip region, there can be some minor overlaps at the edges. As fault frictional properties cannot be directly observed in-situ, an inversion of ground displacement similar to the coseismic one is realised.

5.2.2 Viscoelastic theory

Rocks composing the Earth are deforming elastically and viscously within different timescales and stress regimes. For the study of the viscoelastic relaxation following an earthquake, the understanding of the rheology is essential. Rocks can behave as brittle (which break under stress) or as ductile (flow under stress) materials. When deforming elastically, a rock can return to its original state after the stress release; however, a viscous medium evolves similarly to a fluid and does not return to its original state. The viscosity of Earth rocks is typically within 10^{17} and 10^{23} Pa.s (however, near some volcanoes or some transient viscosities can be lower). This large range of viscosity values is due to the variation of temperature as described by Arrhenius law (see equation 5.9, Moore & Parsons (2015)). The temperature increases with depth and viscous flow is usually at depth, below a rigid layer. Viscoelastic materials (Barbot & Moore (2019)) act as elastic over short-time following Hooke's

law (equation 5.10) and as viscous over long-period following a viscous rheology (equation 5.11).

$$\eta = A \exp\left(\frac{Q}{RT}\right) \quad (5.9)$$

η: Viscosity;
T: Absolute temperature;
A: Pre-exponential factor;
Q: Activation energy;
R: Universal gas constant.

$$\epsilon = \frac{\tau}{G} \quad (5.10)$$

G: Rigidity;
τ: Shear stress;
ϵ: Strain.

$$\dot{\epsilon} = \frac{\tau}{\eta} \quad (5.11)$$

η: Viscosity;
ϵ: Inelastic strain.

Finally, the governing equation for a Maxwell material is expressed by 5.12:

$$\dot{\epsilon} = \frac{\dot{\tau}}{G} + \frac{\tau}{\eta} \quad (5.12)$$

In the simple case of 1D Maxwell material, the viscoelastic relaxation following the coseismic rupture is defined by equation 5.13 (extracted from Teunissen & Montenbruck (2017)):

$$d = B\left(1 - \exp\left(-\frac{t}{\tau}\right)\right) \quad (5.13)$$

d: Displacement;
B: Multiplicative constant;
t: Time since the event;
τ: Relaxation time depending on the ratio of the shear modulus and viscosity.

5.2.3 Coupled modelling

To analyse the behaviour of a viscoelastic material under stress perturbation, some approximations are made to build models based on simple constitutive laws. In the case of Earth deformation, a viscoelastic medium can be constructed from a combination of elastic and viscous properties, schematically represented by springs and dashpots in series or parallel (Bürgmann & Dresen (2008)). Spring and dashpot behaviours are used to approximate the shear zone, respectively corresponding to an elastic material and a viscous material. Their joint response gives a viscoelastic system. Three controls interplay in a viscous shear zone: viscosity-depth dependence, shear-stress heating and a power-law stress–strain rate relation (Moore & Parsons (2015)).

The rheology of the upper crust can be described by linear elastic stress-strain relations. A spring represents a Hooke solid and a dashpot, a Newtonian fluid. Deformation at higher temperatures and pressures is requiring both elastic and

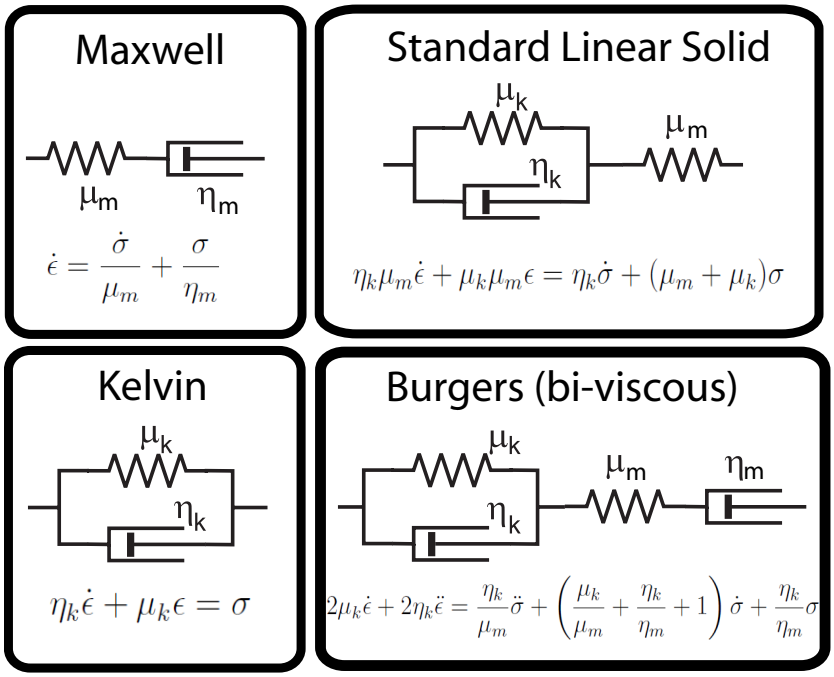

Figure 5.4: Most common linear viscoelastic materials (pictures extracted from Bell (2013)).

viscous behaviours, at least over a short period. In this case, combinations of linear elastic and linear viscous elements are considered.

An elastic element is described as a spring i.e. as an instantaneous reaction:

$$\sigma_s = 2\mu\epsilon \qquad (5.14)$$

σ: Stress;
μ: Young modulus;
$\mu_m = 2\mu$;
ϵ: Strain.

A viscous element acts as a dashpot with a viscous fluid and is time-dependent:

$$\sigma_d = 2\eta\frac{\partial\epsilon}{\partial t} \qquad (5.15)$$

η: Viscosity;
$\eta_m = 2\eta$;
Earth's rock $\eta = [10^{17}\ \ 10^{23}]$ Pa.s ;
$\delta\epsilon/\delta$t: Strain rate.

Figure 5.4 is a description of the variety of mechanical processes that can describe postseismic deformation.

Maxwell material is the simplest viscoelastic model with the desired short-term ($t \to 0$) elastic and long-term ($t \to \infty$) viscous behaviour. It is composed of a spring and a dashpot in series. It is usually used to model crustal deformation because it acts as an elastic solid for short time and as a viscous fluid at infinite times. A Maxwell body corresponds to a steady-state diffusion creep due to the linear relationship between stress and strain rate. This material possesses a constant viscosity.

In mathematical term, the stress and strain are expressed as (Chapter 6 of Segall

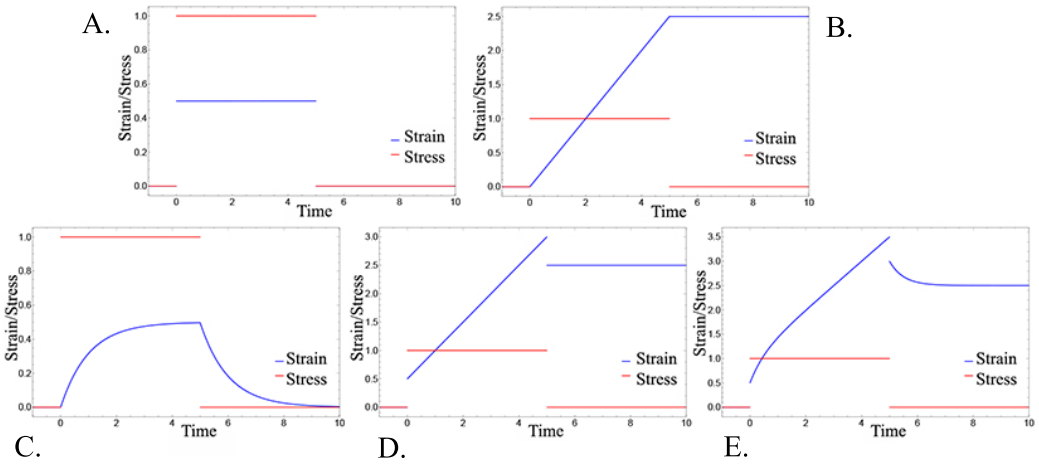

Figure 5.5: Strain-stress relationships for theoretical viscoelastic relaxation of different bodies. A. Elastic solid; B. Viscous fluid; C. Kelvin material; D. Maxwell body; E. Burgers rheology. [Figures credits to James D. P. Moore]

(2010)):

$$\sigma_{max} = \sigma_s = \sigma_d \tag{5.16}$$

$$\epsilon_{max} = \epsilon_s + \epsilon_d \tag{5.17}$$

The strain rate is then:

$$\dot{\epsilon} = \dot{\epsilon_s} + \dot{\epsilon_d} \tag{5.18}$$

As

$$\dot{\sigma}_s = \mu_m \dot{\epsilon}_s \qquad \& \qquad \tau = \frac{\eta_m}{\mu_m}$$

giving the Maxwell material equation (i.e. equation 5.12):

$$\mu_m \dot{\epsilon} = \dot{\sigma} + \frac{1}{\tau}\sigma \tag{5.19}$$

A Kelvin material is composed of a spring and a dashpot in parallel: it behaves at long times as a solid and it is rigid at short times, hence it does not sustain long-term deformation.

$$\sigma_{kel} = \sigma_s + \sigma_d = \mu_k \epsilon + \eta_k \dot{\epsilon} \tag{5.20}$$

More complex rheologies can be created by combining springs and dashpots (for instance, the Standard Linear Solid or the Burgers rheology). Figure 5.5 presents their principle at short and long term.

A Burgers material is composed of a Kelvin material in series with a Maxwell's. In the case of postseismic deformation over a long period, Burgers rheology is usually used. The Burgers rheology is commonly referred as bi-viscous due to its combination of a recoverable deformation described by the Kelvin solid, and a non-recoverable deformation described by the Maxwell fluid. It is a linear rheology that fits postseismic deformation composed of a short-term transient deformation followed by a long-term relaxation. Several examples have used this rheology (Muto *et al.* (2019); Pollitz *et al.* (2006); Tang *et al.* (2019)).

Finally, to obtain a realistic model, the variation of viscosity with depth has to be taken into account. The viscosity of rocks is in function of many physical parameters including temperature (increasing with depth and explained by an Arrhenius law) and pressure, local stress and strain rate, mineral content and grain size, fluid content, etc. Muto *et al.* (2019) explains that transient creep and power-law flow is needed to explain geodetic data. Furthermore, following the study of Tang *et al.* (2019) analysing the rheological behaviour of the lower crust after the Chi-Chi earthquake, in this study, a power-law Burgers rheology will be applied.

A power-law rheology is defined as follows:

$$\dot{\epsilon} \propto \sigma^n \qquad (5.21)$$

$\dot{\epsilon}$: Strain rate;
σ: Stress;
n: Stress exponent.

In the case of n=1, a Newtonian rheology is obtained where viscosity is stress invariant and strain rate increases linearly with stress (for instance, diffusion creep). In the cases of n $\geq$ 1, strain rate is dependent in a non-linear way to the stress. For example, the movement of dislocations within crystals gives rise to a deformation mechanism called dislocation creep which is a power-law rheology with n=3.

In this study, a power-law rheology at steady state and power-law rheology for transient creep are combined. The viscoelastic relaxation is modelled with a Burgers body following a non-linear steady-state flow law in the Maxwell element (equation 5.22). The strain rate of the transient deformation is modelled by a deforming Kelvin material (equation 5.23):

$$\dot{\epsilon}_M = A_M \sigma^n C_{OH}^r \exp\left(-\frac{Q+pV}{RT}\right) \qquad (5.22)$$

$$\dot{\epsilon}_K = A_K (\sigma - 2G_K \epsilon_K)^n C_{OH}^r \exp\left(-\frac{Q+pV}{RT}\right) \qquad (5.23)$$

$\dot{\epsilon}_M$: Steady-state strain rate;
ϵ_K: Cumulative transient strain;
G_K: Strain-hardening coefficient;
A_M and A_K: Pre-exponential factor;
σ: Norm of the deviatoric stress tensor;
C_{OH} and r: Water content and its exponent;
n: Stress exponent;
Q: Activation energy;
T: Absolute temperature;
R: Gas constant;
V: Activation volume;
P: Pressure.

Stress-driven afterslip is modelled with a velocity-strengthening friction law following equation 5.24 which describes a non-linear response after a stress followed by a relaxation:

$$\nu = 2\nu_0 \sinh \frac{\Delta\tau}{(a-b)\sigma_n} \qquad (5.24)$$

$\Delta\tau$: Stress change after the mainshock;
$a - b$: Steady-state friction parameter;
σ_n: Effective normal stress;
ν: Velocity of afterslip;
ν_0: Reference slip velocity.

To conclude, Maxwell rheology explains steady-state (i.e. constant stress or strain rate) diffusion creep and a power-law rheology explains a dislocation creep. The viscosity is varying in a power-law rheology (non-linear function joining stress and strain rate). To account for an initial transient creep (i.e. rapid change of stress or strain rate), a Burgers rheology or a power-law Burgers rheology can be used, explaining diffusion creep and dislocation creep. A Kelvin element represents the strain rate of the transient phase. The linear Burgers rheology explains a steady-state and transient creep in the diffusion creep regime while the non-linear power-law Burgers explains a combination of steady-state and transient creep in the dislocation creep regime.

5.3 Data and Methods

5.3.1 GPS

Taiwan Global Positioning System (GPS) network was surveyed since 1990. This dense network is enabling nowadays the study of crustal deformation and tectonics in Taiwan. The data used in this chapter were provided by the Institute of Earth Sciences, Academia Sinica (IESAS), Taiwan covering from 1993 to 2019 from permanent stations (see Figure 5.6).

Hector software (Unix based, Python scripts and C++ source code, Bos *et al.* (2013)) was used to estimate a trend in TS with temporal correlated noise and remove factors such as seasonal signal or outliers that are affecting the TS. The main steps and scripts used are presented in Figure 5.7 and were extracted from the software manual of Bos & Fernandes (2019). First, offsets are estimated (Chi-Chi earthquake epoch was added to the header) followed by a removal of outliers, seasonal signals are then estimated.

Several noise models can be used and combined in Hector's software to fit various periodic signals to the observations which annual and semi-annual amplitude may vary from year to year. A Wiener filter is used to precisely estimate the varying part of the seasonal signal. A combination of noise model is performed to estimate the constant part of the seasonal signal including white noise and power-law noise. A trend is estimated (the period for the estimation of the trend is varying for each

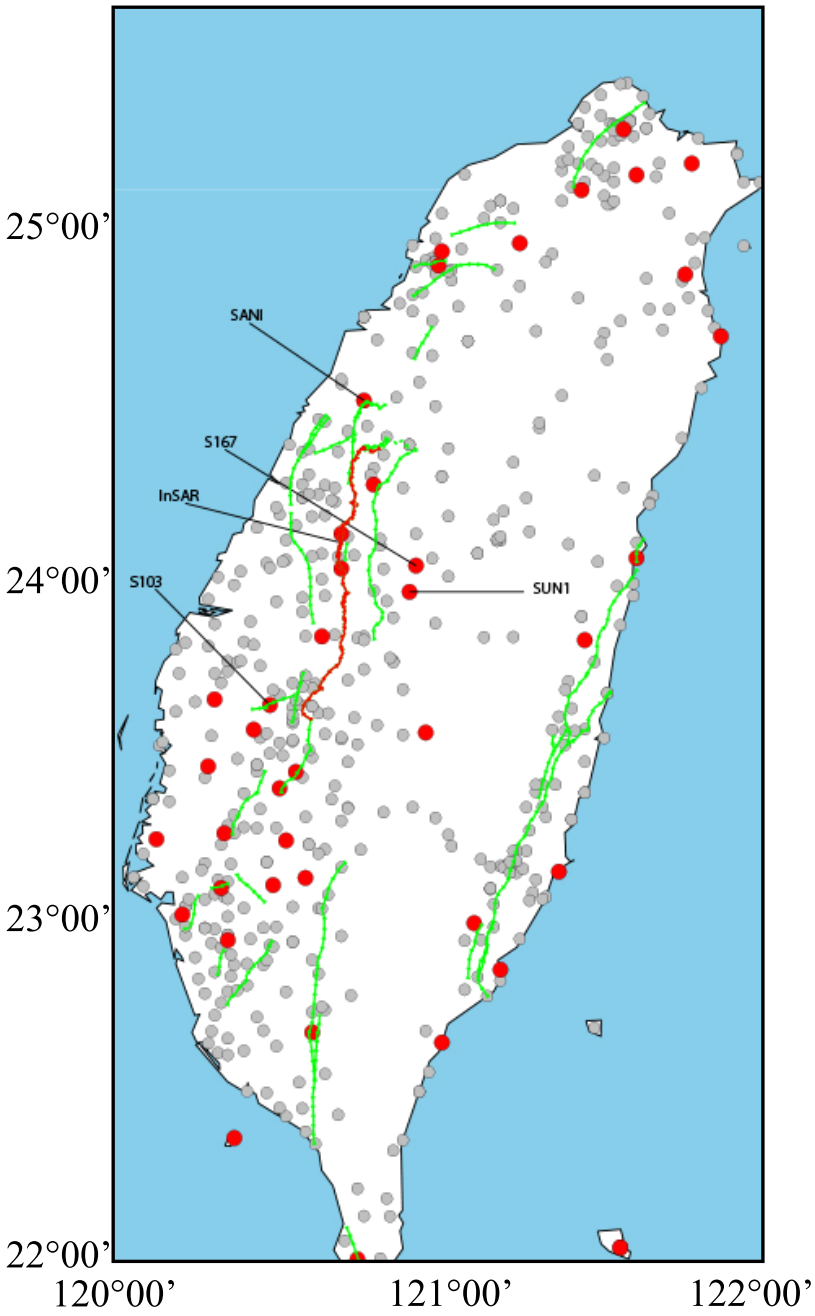

Figure 5.6: GPS stations available over Taiwan from 1993 to 2020 shown by the grey dots. Red dots correspond to stations recording from before the event until a few years of the postseismic period. Locations of the GPS and InSAR points mentioned in Section 5.4 are presented here.

station). Finally, TS and power-spectral density are plotted. Some results are presented in Figure 5.8.

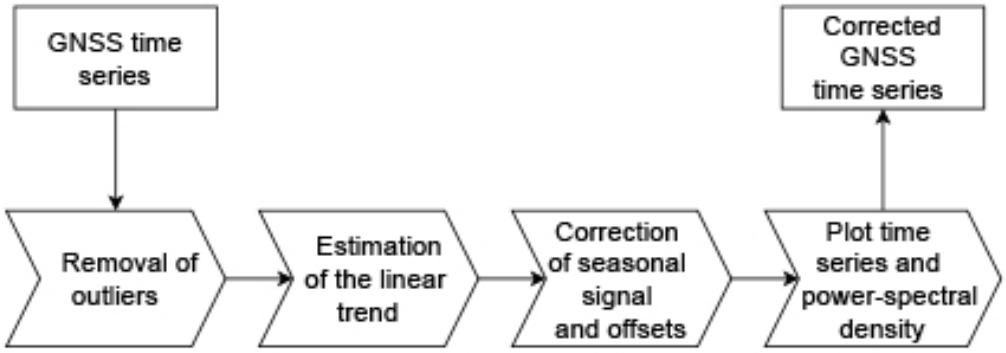

Figure 5.7: Hector's workflow to correct GPS time series.

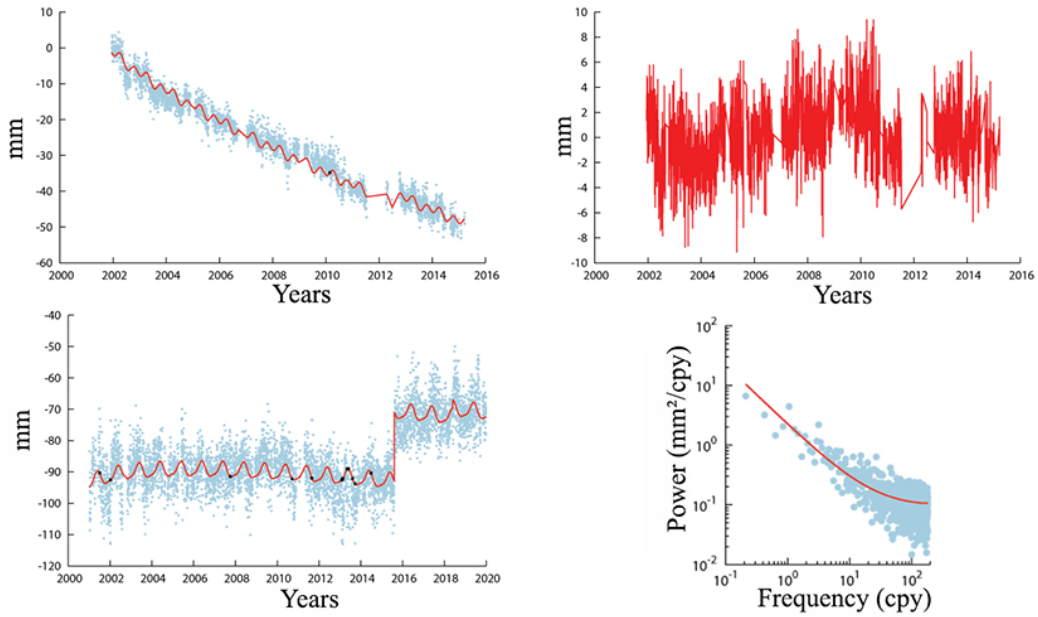

Figure 5.8: (Top) PLAN station (north component) and its residual on the right. (Bottom) S016 station (vertical component) and the fitted signal showed in red. On the right, the power-spectral density of its residuals is presented (the red line corresponds to the noise model). Blue dots are the original TS.

5.3.2 Levelling

National Taiwan University procured levelling data from 1998 to 2019. Several levelling campaigns take place each year. Figure 5.9.(A) presents levelling data following 6 lines in the middle of the Chelungpu fault that were recorded between 1998 and 2002. Figure 5.9.(B) presents 6 levelling lines covering the entire fault and recorded from 2002 to 2019. A large uplift was visible due to the rupture, up to 5 m.

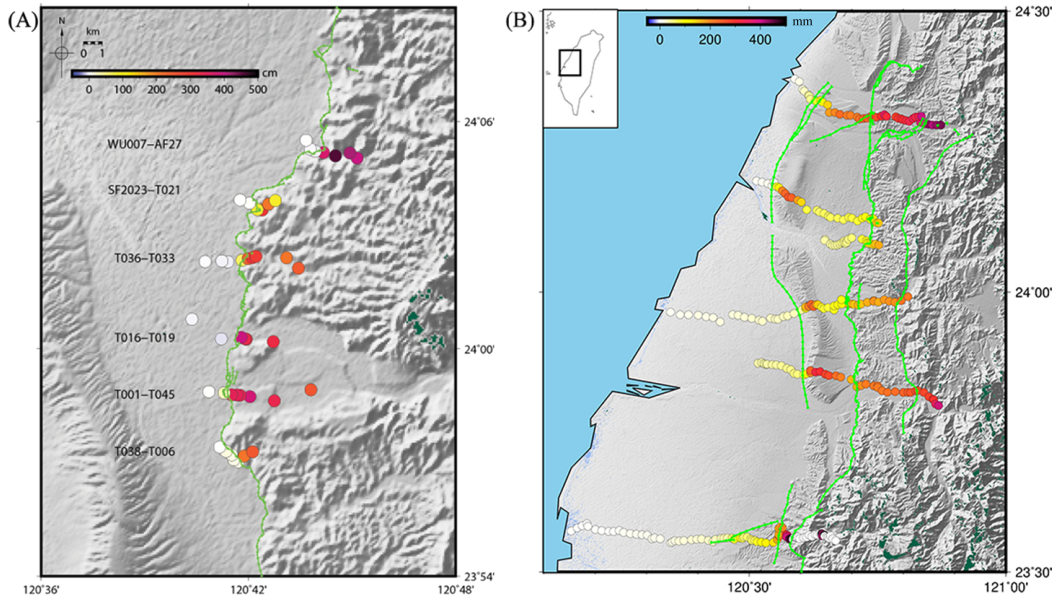

Figure 5.9: Levelling lines over Central Western Taiwan covering (A) 1998-2002 and (B) 2002-2019.

5.3.3 InSAR

InSAR is widely used to study fast and slow ground surface deformation with high spatial resolution. To monitor the postseismic deformation in Central Western Taiwan, a stack of SAR images will be utilized to generate InSAR time series analysis. Before processing, the data are automatically downloaded from the ASF (Alaska Satellite Facility) Alaska website (`https://search.asf.alaska.edu/`) and converted to SLC (Single Look Complex) files with GAMMA Remote sensing (Wegmüller *et al.* (2016); Werner *et al.* (2000)). To cover the 20 years since the earthquake struck the island, ERS, EnviSAT and Sentinel-1 images are combined (see Figure 5.10). Information on the downloaded images for each satellite and the number of interferograms created are presented in Table 5.1. The period covered by ERS satellite is of $\sim$ 11 years, $\sim$ 3.4 years for EnviSAT, $\sim$ 3 years for the ascending orbit (path 69 frame 75) of Sentinel-1A/B and $\sim$ 5.5 years for the descending orbit of Sentinel-1A/B (path 105 frame 510).

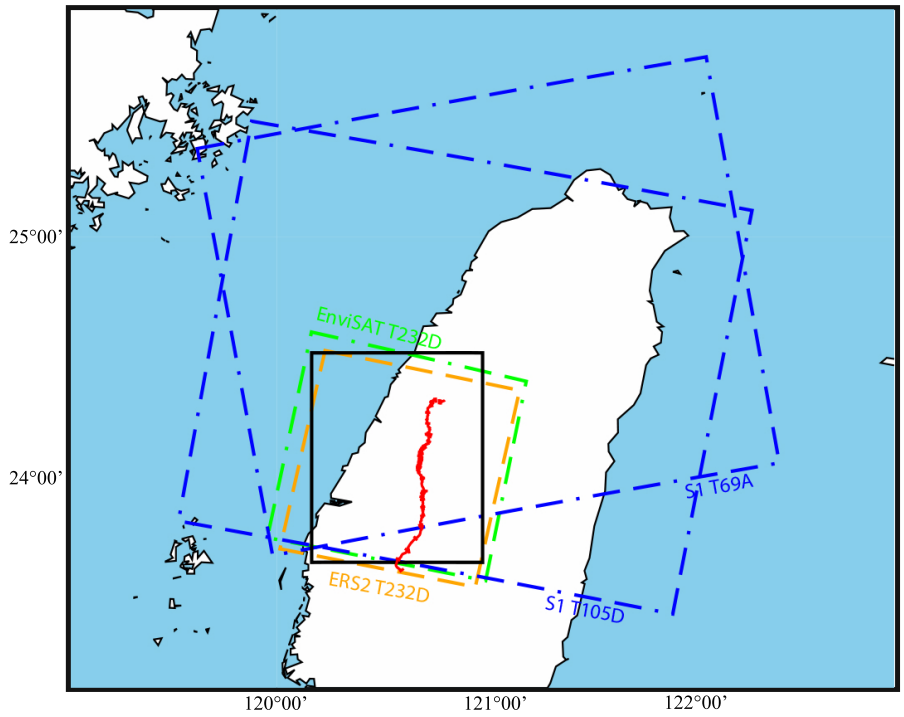

Figure 5.10: Map of Taiwan showing the location of the SAR track. The black rectangle represents the subset of images corresponding to the study area. Blue dashed rectangles represent Sentinel-1 ascending and descending tracks. The orange dashed rectangle represents ERS track and the green dashed rectangle, EnviSAT track.

Table 5.1: ERS, EnviSAT and Sentinel-1A/B used in this study ('ifgs' for interferograms, 'Nb' for number, 'Acq' for acquisition).

Satellite	**Track**	**Orbit**	**Start date**	**End date**	**Acq. time (UTC)**	**Nb of images**	**Nb of ifgs**
ERS	232	Desc.	20/04/2000	17/02/2011	02:31	61	254
EnviSAT	232	Desc.	19/05/2005	25/09/2008	02:01	23	65
Sentinel-1	69	Asc.	16/03/2017	23/05/2020	10:00	95	312
Sentinel-1	105	Desc.	05/11/2014	25/05/2020	21:51	115	387

To study the 20 years of postseismic deformation following the Chi-Chi earthquake, ERS, EnviSAT and Sentinel-1A/B are available as C-band satellites. Only descending track were used for ERS and EnviSAT from the track 232, too few acquisitions were available in ascending orbit. Figure 5.11 shows the spatial-temporal baselines for all satellites (maximum, minimum and standard deviation are specified). Interferograms were generated using GAMMA software following the steps presented in Chapter 3. Precise Delft orbits were used to reduce baseline errors

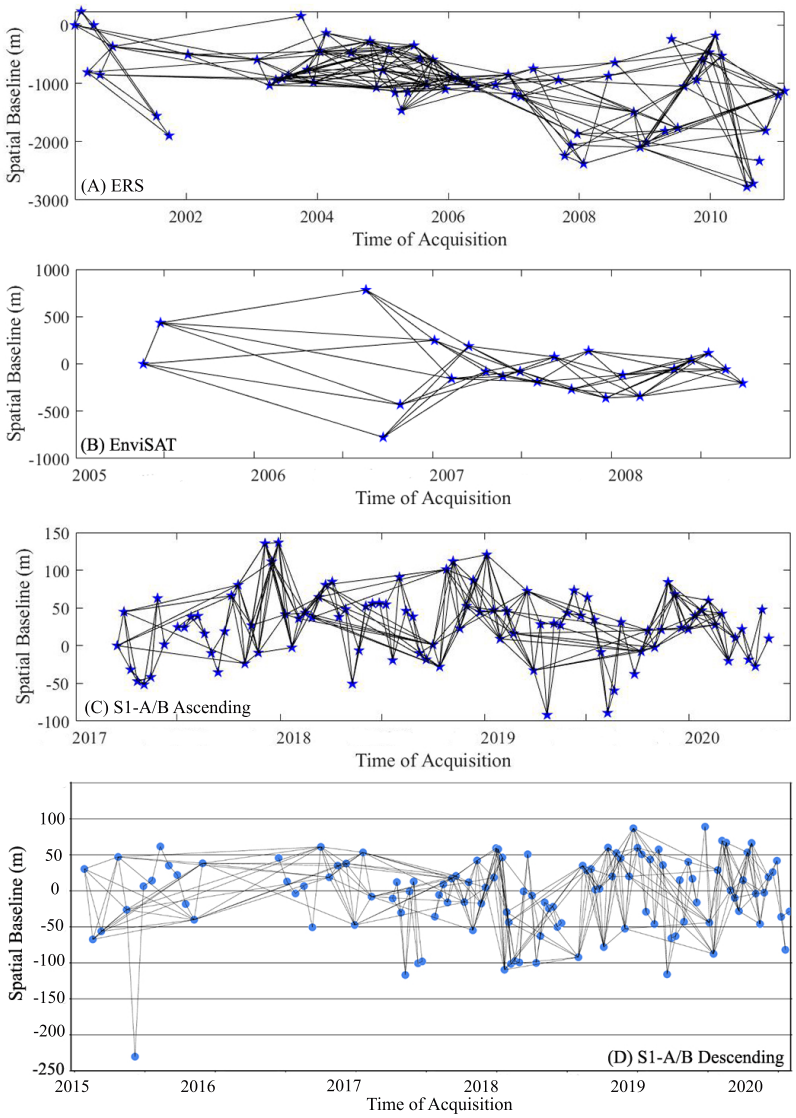

Figure 5.11: Spatio-temporal baselines for (A) ERS ([min max std (m)]=[0.47 2592.7 629.4]); (B) EnviSAT ([min max std (m)]=[4.0 962.8 380.6]); (C) Sentinel-1 ascending track ([min max std (m)]=[0.26 160.5 59.4]); (D) Sentinel-1 descending track ([min max std (m)]=[0.07 236.8 70.2]).

of ERS and EnviSAT satellites, and EOF for Sentinel-1A/B, and to assist the co-registration and flat-Earth removal steps as described in Chapter 3. SRTM DEM was used to remove the topographic phase contribution. A multi-looking of 4x20 m was applied to reduce the phase noise. The unwrapping was done using the MCF method with a coherence threshold of 0.3 (Goldstein & Werner (1998)). Finally, before running the TS analysis, the tropospheric effect impacting the interferograms (mainly in summer) was corrected using relative ZTD maps generated on GACOS platform (`http://www.gacos.net`).

5.3.4 Time series Analysis

The complete InSAR-TS workflow is presented in Figure 5.12 and will be detailed in this section from interferogram formation to validation of the TS and taking into account spatial and temporal variation of the atmosphere. A network of hundreds of interferograms is used with short temporal separation and small perpendicular baselines to minimize spatial decorrelation. All images are interferometrically processed and unwrapped, GACOS APS maps are applied to correct from the atmospheric impact and TS were then performed using SBAS technique: InSAR TS + AEM (InSAR time series Atmospheric Estimation Model).

Preparation of the stack of unwrapped and geocoded interferograms. Interferograms are automatically produced using GAMMA software. A Tandem-X or SRTM DEM is used throughout the process and downsampled to 90 m (mainly for processing time and space reasons). A single primary image is selected for each type of satellite, in the middle of the period and used to coregister the secondary images. A partial network-SBAS (all necessary pairs) is generated with a maximum temporal baseline of 1000 days. The strategy is to coregister by applying the nearest resampled SLC. The interferograms are multilooked, with a factor of 4x20 m in azimuth x range, respectively and spatially filtered to reduce noise using a GAMMA adaptative power spectrum filter (alpha value 0.7). The phase is then unwrapped in two dimensions using a statistical cost approach (MCF) with SNAPHU. An unwrapped threshold of 0.4 for Sentinel-1 (and 0.3 for ERS and EnviSAT) is applied to mask decorrelated pixels. Finally, the interferograms are geocoded.

Generic Atmospheric Correction Online Service for InSAR (GACOS): Tropospheric noise correction using GACOS (`www.gacos.net`)
To correct from the atmospheric impact, more specifically the tropospheric effect, GACOS (Yu *et al.* (2017*a*,*c*,*b*)) is used in this study. It is based on the Iterative Tropospheric Decomposition (ITD) model to separate stratified and turbulent signals from tropospheric total delays, and generate high spatial resolution zenith total delay maps. GACOS uses a High Resolution ECMWF weather model at 0.125° and 6-hour resolutions, SRTM DEM (90 m, S60-N60) and ASTER GDEM (90 m, N60-N83, S60-S83). The outputs are tropospheric delay maps given in a grid binary format.

Especially in summer, satellite images over Taiwan are highly impacted by the atmospheric error (up to 10 cm or more Morishita *et al.* (2020)). The tropospheric parameters (water vapor, temperature and pressure) vary with season and area, and are correlated with topography. To correct the spatial and temporal variation of the tropospheric layer of the atmosphere masking the geophysical signal, tropospheric delay maps generated by GACOS derived from the high-resolution European Centre for Medium-Range Weather Forecasts (HRES-ECMWF) data. Finally, a linear temporal interpolation is applied to coincide with the time of the SAR acquisition. The atmospheric delays are spatially densified to 90 m in accordance with the inter-

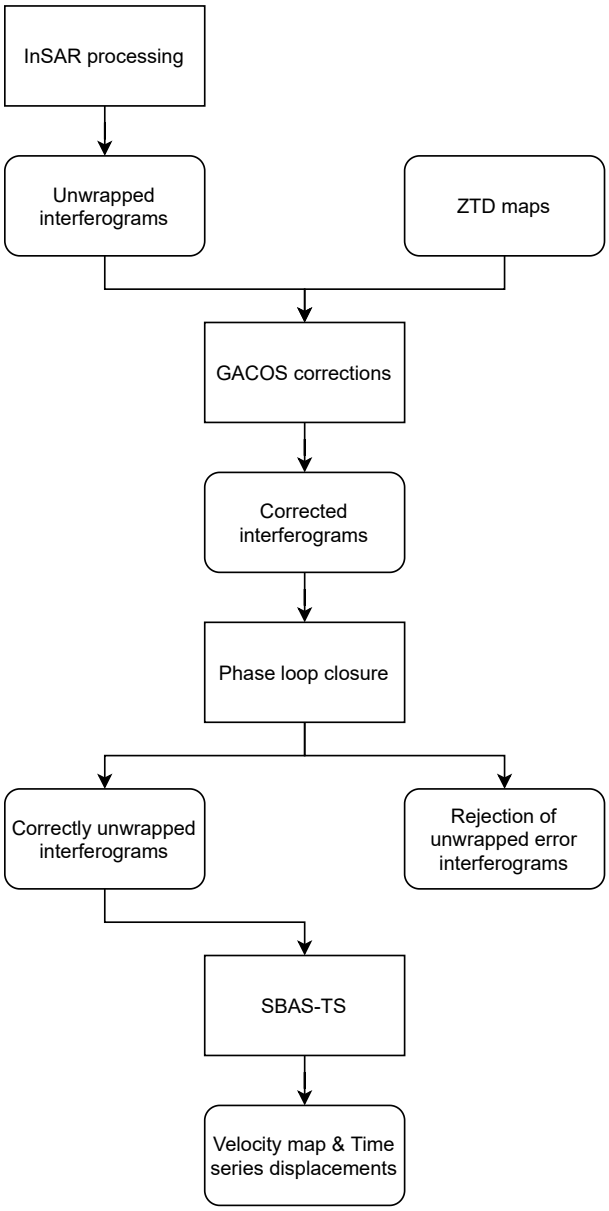

Figure 5.12: InSAR time series workflow.

ferogram spacing using an ITD spatial interpolator (Yu *et al.* (2017*b*)). A projection along the Line-Of-Sight (LOS) of the interpolated zenith tropospheric delays is done using the Global Mapping Function (Boehm *et al.* (2006)) and then subtracted from the unwrapped phases. GACOS corrections are globally available in near real-time. A simple procedure is required on the online platform to get the delay maps over the specific area and at the time of the acquisition of the SAR images. Figure 5.13 shows a reduction of atmospheric effect after applying GACOS corrections.

In this study, the impact of the ionosphere is not taken into account as usually the delay is low for short-wavelength as used by C-band SAR satellites in non-

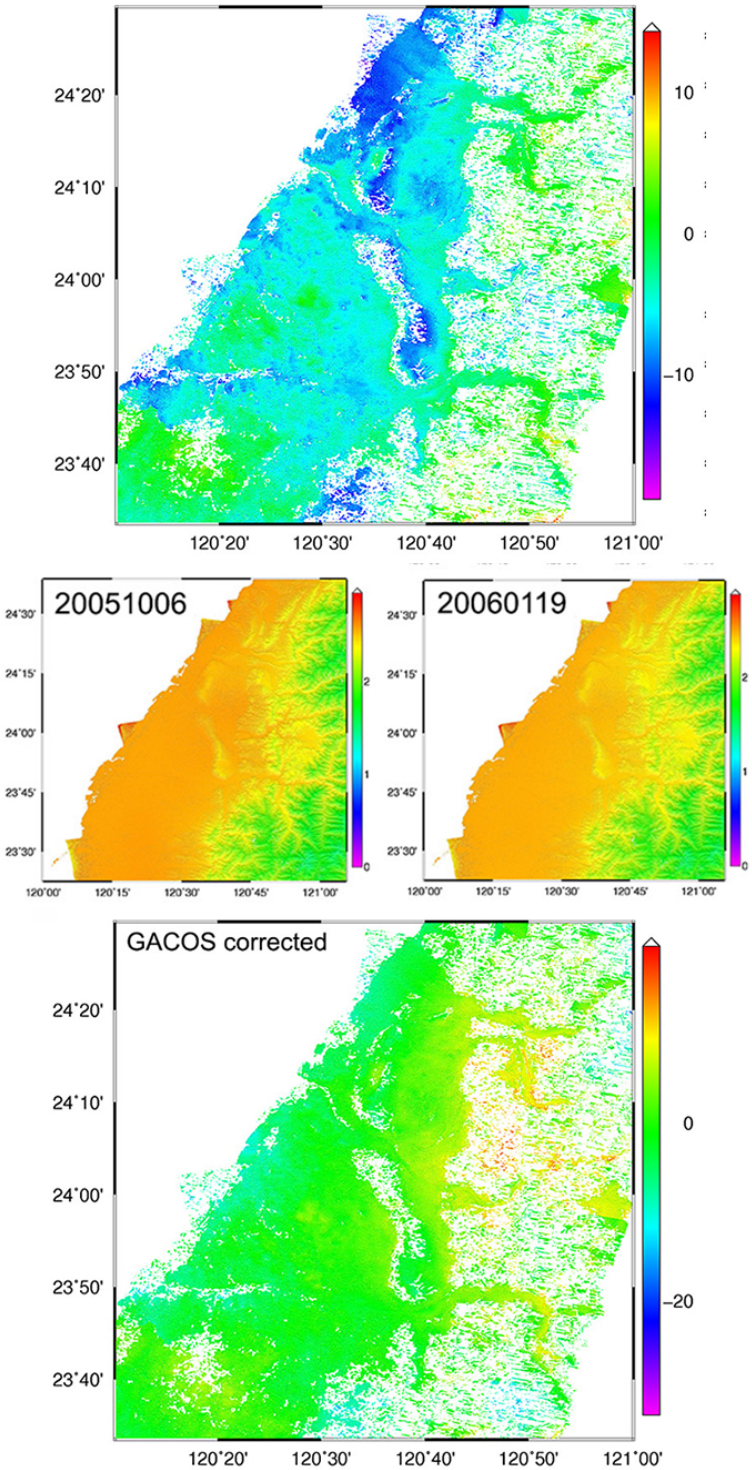

Figure 5.13: (Top) Interferogram before and after (bottom) atmospheric correction and the tropospheric delay maps (middle images) for the two days corresponding to the interferogram.

tropical or polar regions. Furthermore, the study area is quite small. However, in some studies of Taiwan, the correction of the ionospheric impact was necessary (for instance, Liao *et al.* (2020)).

Interferometric synthetic-aperture radar time series program
The in-house program is written in C++ enabling multiprocessing and based on Li *et al.* (2009) (`https://chenyublog.netlify.app/year-archive/`). The TS inversion is calculated by a general Gauss-Markov linear model (weighted least square) and then, filtered in the frequency domain by FFTW (a C-subroutine library for computing the discrete Fourier transform `http://www.fftw.org/`). The estimation is run on a pixel-by-pixel basis. Displacement TS and velocity map are the outputs. As tropospheric corrections were applied, orbital ramp corrections were switched off, but unwrapping error verification was applied.

Phase closure: Identification and masking of pixels incorrectly unwrapped by checking loop closure.
Unwrapping errors can be present in the stack of interferograms and significantly disturb the derived time series. A first manual check can be realised but it is highly time consuming depending on the number of interferograms generated. For more precision, phase closure methodology is applied to interferogram triples within an interferometric network. This methodology (Morishita *et al.* (2020)) uses the redundancy of the network and evaluated the loop phase closure. Pixels presenting errors are masked (the number of loops depends on the network).

The theory is the following: for three images (called 1,2 and 3) and a triplet of three unwrapped interferograms (12, 23, 13), the loop phase closure is estimated by (Biggs *et al.* (2007)):

$$\Phi_c = \phi_{12} + \phi_{23} - \phi_{13} \tag{5.25}$$

In the case of no unwrapping errors, Φ_c should approximately equal 0 (due to the filtering and multi-looking of the phase in the SAR processing steps). Otherwise, for unwrapping errors present in the loop, Φ_c will be close to an integer multiple of π called misclosure residual (usually π or 2π). A threshold of 3.14 for the misclosure residual is specified to delete interferograms presenting too many unwrapping errors or pixels that have failed too many loops (the ratio of failed loops amongst all possible loops is set to 0.5, knowing that at least 2 loops are required): the overall percentage of failed loops is considered as well as the standard deviation of the misclosure residual of a pixel on all loops. Finally, a minimum of 0.4 is set corresponding to a minimum of valid interferogram in function of all interferograms considered. This step is done on a pixel-by-pixel basis and mean statistics are calculated for each interferogram to remove bad candidates from the network.

Considering STD_i the phase closure standard deviation for the i^{th} interferogram, the threshold *th* is used to define a *confidence_level* to delete interferograms (the larger the value, the more confidence in deleting interferograms (by default set to

$2\sigma)$) :

$$th = \sum_{i=1}^{n} STD_i + \sqrt{\frac{1}{n}\sum_{i=1}^{n}(STD_i - \text{mean})^2} * \text{confidence\_level} \tag{5.26}$$

Parametrization of the TS
The first step of the time series program was to search for phase closure errors. Now, the actual TS inversion can be done. Different temporal constraints can be applied: no temporal constraint on displacement TS, linear (D=vt) or logarithmic constraint (D=vln(t)). Time series filtering parameters have to be selected: no filter, spatial or temporal only or a combination of both.

Due to the low coherence and the presence of large atmospheric signal, several tests of time series were realised, and the final result was compared with GPS TS.

GPS validation:
3D GPS displacements were converted to LOS displacements (Fialko *et al.* (2001)) in order to validate the processing of the InSAR TS. Figure 5.14 shows the displacement comparison between InSAR (ERS, EnviSAT and Sentinel-1) and GPS computed for each corresponding epochs using different techniques. Scatter plots for the linear TS and logarithm TS with or without applying GACOS corrections are showed for ERS. An RMS of 13.5 mm (EnviSAT), 14 mm (Sentinel-1) and 17.6 mm (ERS) and an overall correlation of 0.86 (ERS) to 0.95 (Sentinel-1 A/B) between TS InSAR and GPS is obtained with the final methodology: GACOS application and logarithm TS. A 25.5 mm RMS InSAR-GPS difference was obtained with a linear function and 38 mm with the logarithm TS without GACOS for ERS.

The final cumulative displacement maps for each satellite are presented in Figure 5.15.

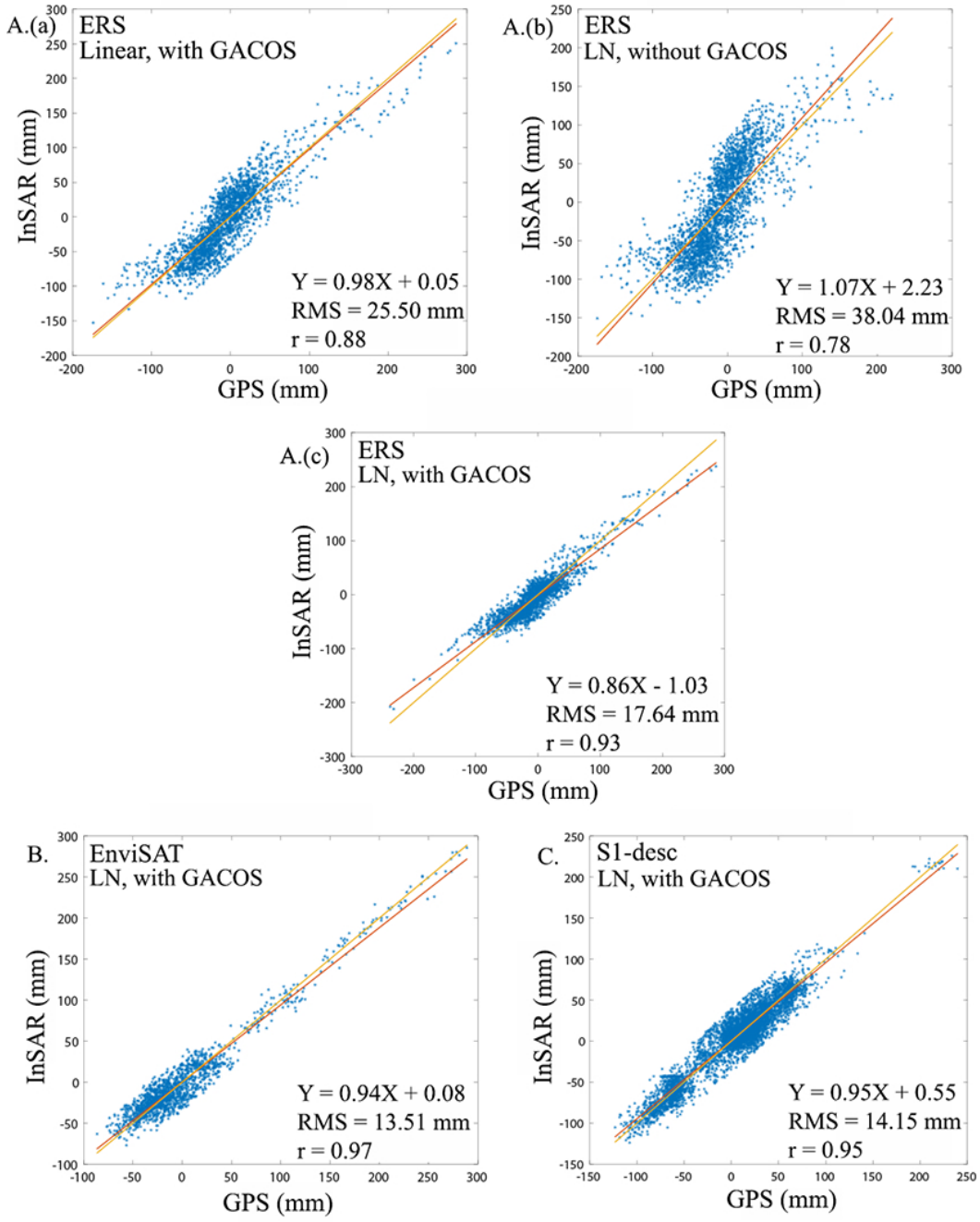

Figure 5.14: Validation InSAR TS against GPS TS: cumulative displacement comparisons with GPS stations for all InSAR acquisitions. Fits to points were made with: A. ERS (a) linear function; (b) ln(t) function: A + B × ln(t) with GACOS corrections; (c) ln(t) function without GACOS corrections applied. B. EnviSAT (ln function with GACOS corrections); C. Sentinel-1 descending (ln function with GACOS corrections). (Outliers larger than 2σ were removed.)

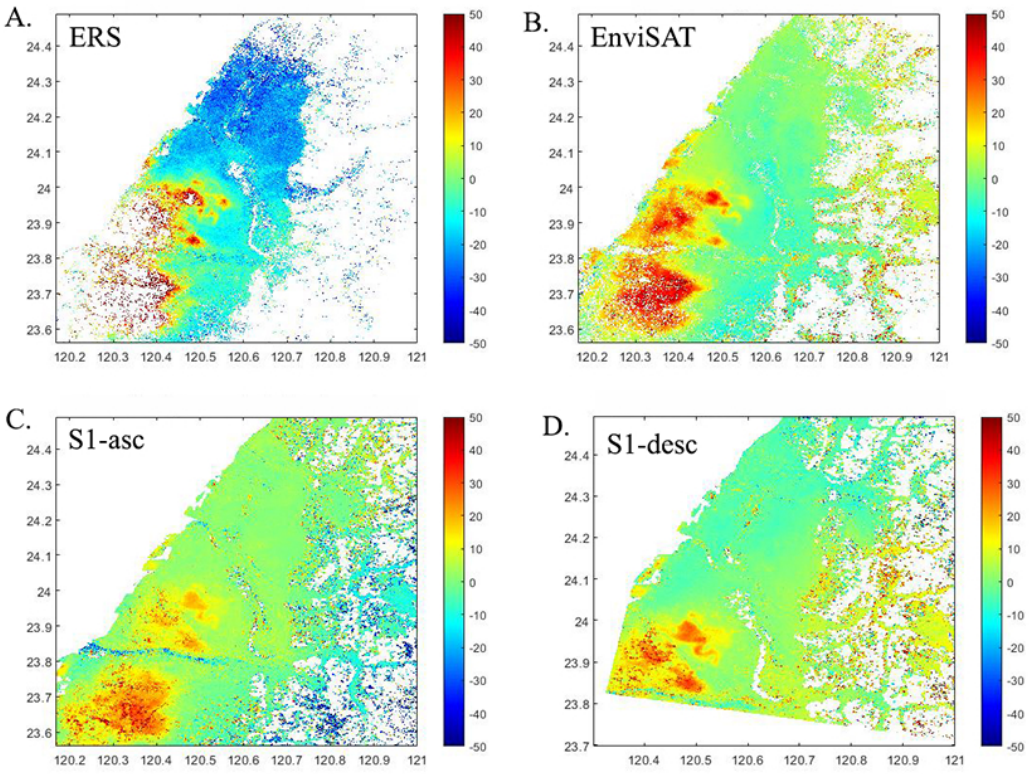

Figure 5.15: Cumulative displacements (legend in mm): A. ERS (2000-2011); B. EnviSAT (2005-2008); C. Sentinel-1 Ascending (2017-2020); D. Sentinel-1 Descending (2014-2020).

5.4 Postseismic deformation

Taiwan is an active seismic area struck frequently by earthquakes and composed of several active faults. Studying and analysing the postseismic deformation of major earthquakes and the current state of motion is a challenge, but it will bring useful information to better understand the earthquake cycle of the Chi-Chi earthquake and the behaviour of thrust faults in general.

All the data needed and available were collected and processed as presented in the previous section. In the following one, I will present the analysis done using time series of GPS and InSAR (ERS, EnviSAT and Sentinel-1A/B) as well as the forward approach used to analyse the afterslip and viscoelastic flow over the 20 years of postseismic deformation which theory was detailed in Section 5.2.

5.4.1 Analysis of 20 years of deformation of Central Western Taiwan

The GPS density in Taiwan has increased substantially the past decades, however stations covering the full 20 years period since the event are rare. A few stations over

the island were recording before the earthquake (such as SANI and S103) and kept recording until now. The coseismic jump and the postseismic transient deformation can be observed (see Figure 5.16). SANI station, situated at the north of the fault on the hanging-wall, shows a 14 cm jump (projecting in ERS LOS direction) while S103, situated on the footwall at the south end, shows a 3 cm jump.

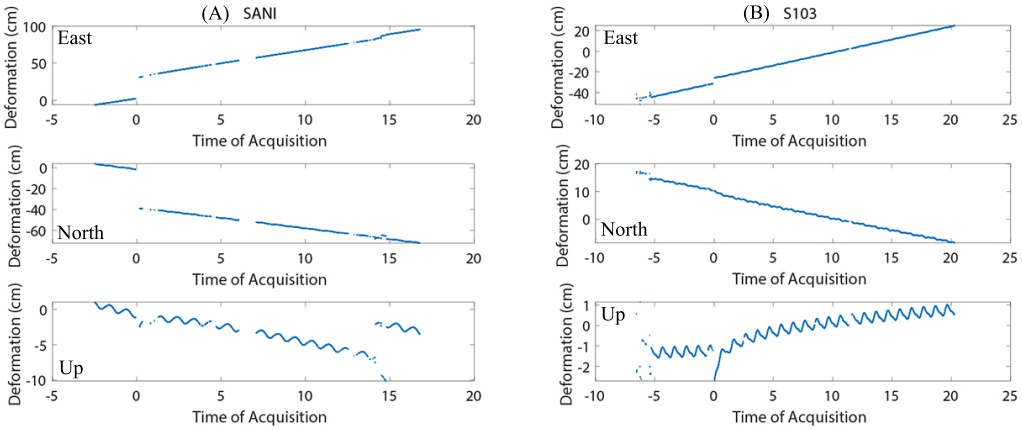

Figure 5.16: GPS time series (East-North-Vertical components) showing the coseismic jump due to the earthquake. (A) SANI station, (B) S103 station (legend in cm).

Zooming on the east component of SANI station (Figure 5.17) and after removing a linear trend (corresponding to the interseismic secular rate), the transient deformation following the earthquake can be observed. For about 3 years, transient displacement is visible. The curve is stabilising after about 1000 days as can be observed using ERS cumulative displacement (but at this stage the rate is still higher than the pre-earthquake one).

The use of InSAR is particularly attractive in such cases due to its high spatial resolution enabling to detect small deformation and study a large area. The earliest image acquisition for ERS is the 20^{th} of April 2000 (no images were available on ASF Alaska before this date). It is used as starting date for this study. Cumulative displacements were estimated from the TS for each satellite (Figure 5.15). Figure 5.18 shows a few ERS cumulative displacement outputs ([35, 140, 630, 1750, 3010, 3955] days), each output is referenced to the first date (20/04/2000) (the subsiding area described in Chapter 2 was hidden in order to detect more easily the postseismic deformation). Positive values represent motion towards the satellite in the LOS direction while negative values correspond to motion away from the satellite. Up to 40 mm of motion is visible after 3955 days on the footwall. Also, the main deformation is happening around the Changhua fault (fault on the west of the Chelungpu fault that is considered as locked in the literature), even though no large seismicity was recorded in this area. The deformation of the Changhua and Tachia faults is mainly aseismic. From the 630 days cumulative displacement map (Figure 5.18.(c)), the south part of the fault shows more deformation, up to 15 mm, while only a maximum of 5 mm is visible on the north part near the fault.

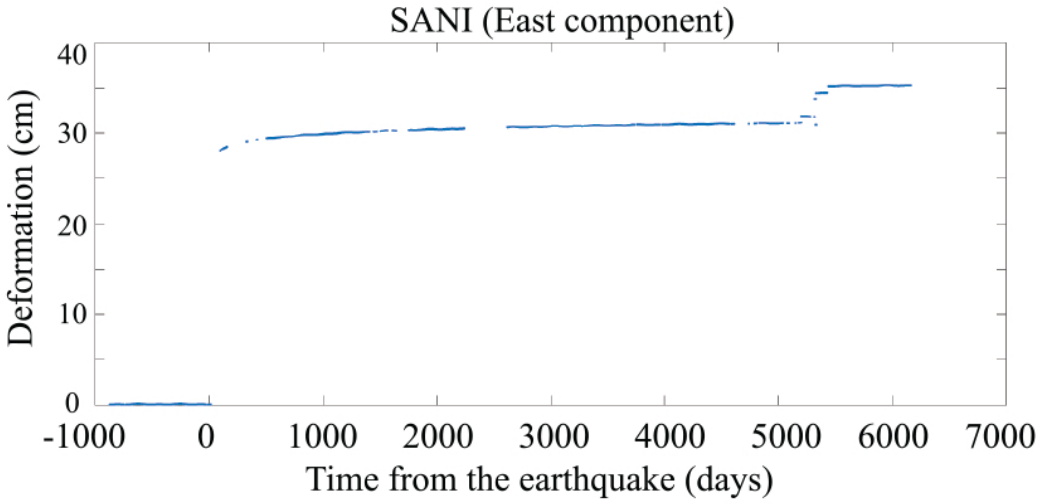

Figure 5.17: East component of SANI station without the interseismic contribution (legend in cm).

ERS TS were extracted at different positions (Figure 5.19) on both sides of the fault. With the exception of points along the coast where it is less obvious (i.e. in the far field), a change in the curve is visible around 2004 (Figure 5.20). After that, the deformation is stabilising or slowing down over most of the fault area. From the study of Sentinel-1 TS (Figure 5.21), an almost linear deformation is observed, no particular change of the deformation seems to be happening nowadays. However, some other events are disturbing the analysis of the Chi-Chi deformation as visible on the seismicity map (Figure 5.3).

5.4.2 Afterslip and viscoelastic flow numerical model

Large earthquakes generate large stress perturbations across a wide area in the crust and upper mantle. Determining the correct rheological behaviour of crust and upper mantle rocks is essential to model the relaxation of stress following an event. An ideal rheological structure will explain the mechanical response of lithospheric plates as well as the nature of convective flow in the upper mantle. However, they are still poorly understood due to the difficulty of modelling viscosity and strain rate at depth (it is not possible to observe in-situ) and several micromechanisms are deforming the crust and upper mantle; for instance, diffusion or dislocation creeps (Kohlstedt & Hansen (2015)).

The postseismic deformation results from the combination of transient non-linear deformation of the materials in the upper mantle and stress-driven afterslip on the fault. In the literature, the stress interactions between fault slip and viscoelastic flow does not always make a large difference while modelling postseismic deformation (Qiu *et al.* (2018)). The afterslip is due to the reversibility of the deformation of elastic materials in the lithosphere. Both mechanisms are redistributing stresses.

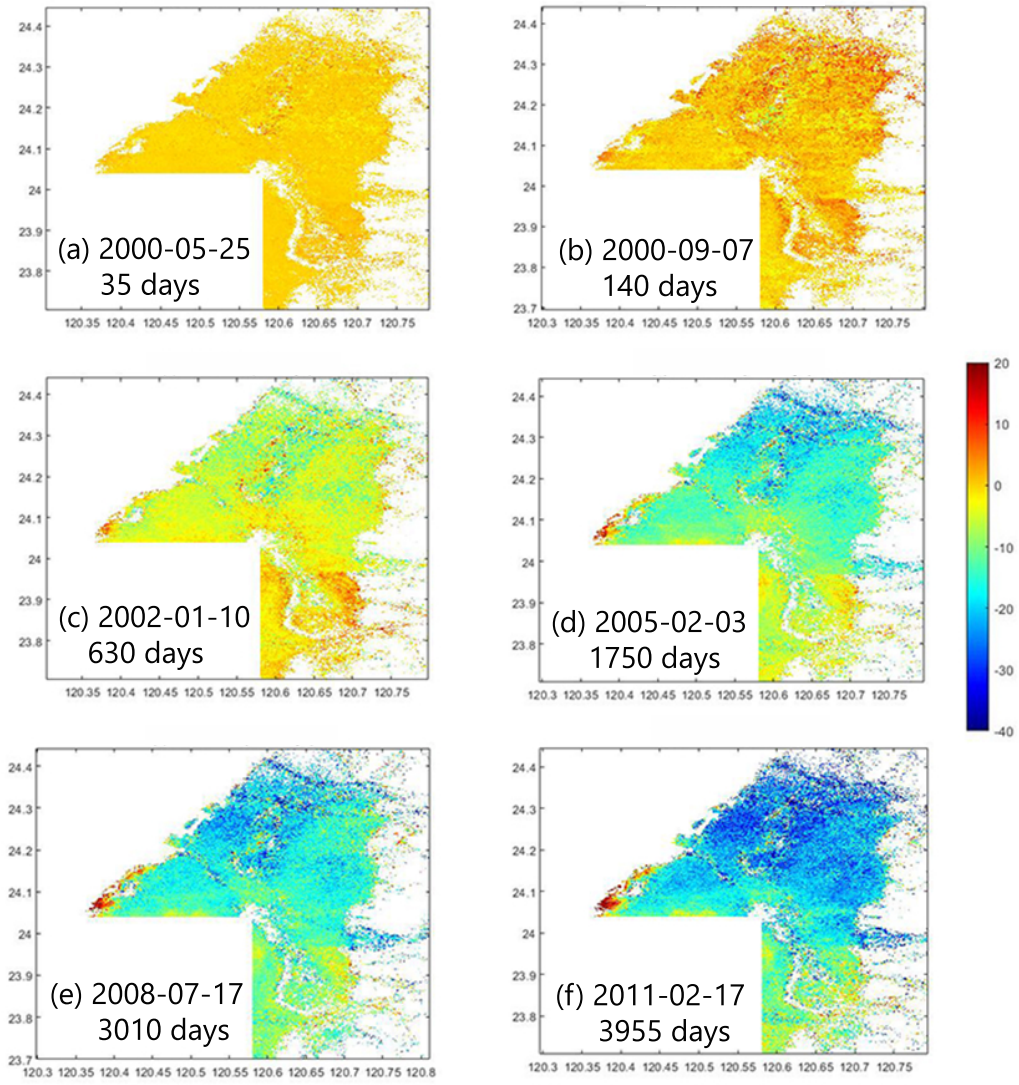

Figure 5.18: Cumulative displacements for different periods (legend in mm); Reference date 20/04/2000. (a) 35 days; (b) 140 days; (c) 630 days; (d) 1750 days; (e) 3010 days; (f) 3955 days.

Afterslip, mainly happening aseismically, increases the geodetic moment and acts on localised regions while viscoelastic flow redistributes stresses over a more distributed area and in deeper layers. In the case of the Chi-Chi earthquake, they are considered mechanically coupled (Tang *et al.* (2019)).

As explained in Section 5.2.3, rheological behaviours are approximated by spring-dashpot combinations. Tang *et al.* (2019) in their inverse model tested different rheologies to simulate the temporal evolution of stress and strain rate in the lower crust following the Chi-Chi rupture and concluded that a power-law Burgers rheology gives the best fit in this particular case.

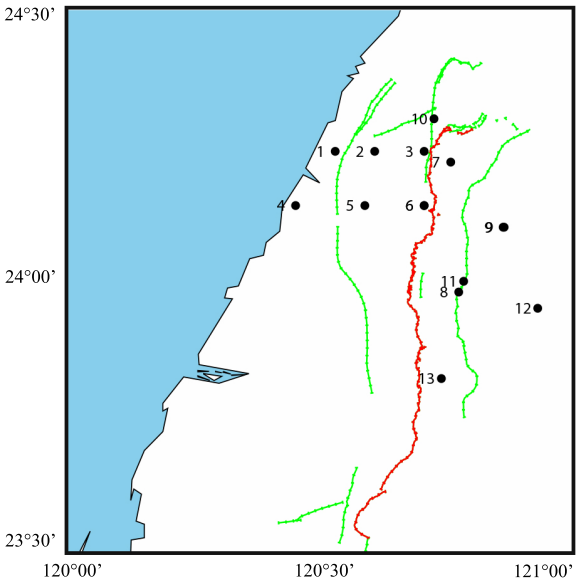

Figure 5.19: Map showing the location of the pixels extracted from the cumulative displacement maps to plot time series (Figure 5.20 & 5.21). The Chelungpu fault is represented in red and other active faults in green.

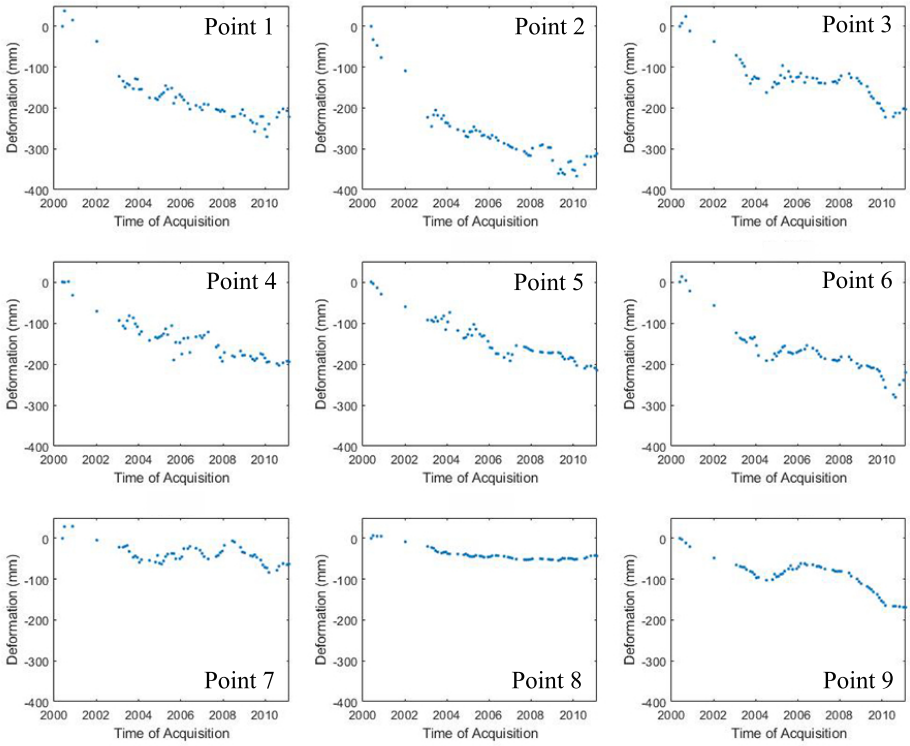

Figure 5.20: ERS time series corresponding to pixels presented on Figure 5.19. Points 1-6 & 10 are on the footwall, Points 7-9 & 11-13 are on the hanging-wall.

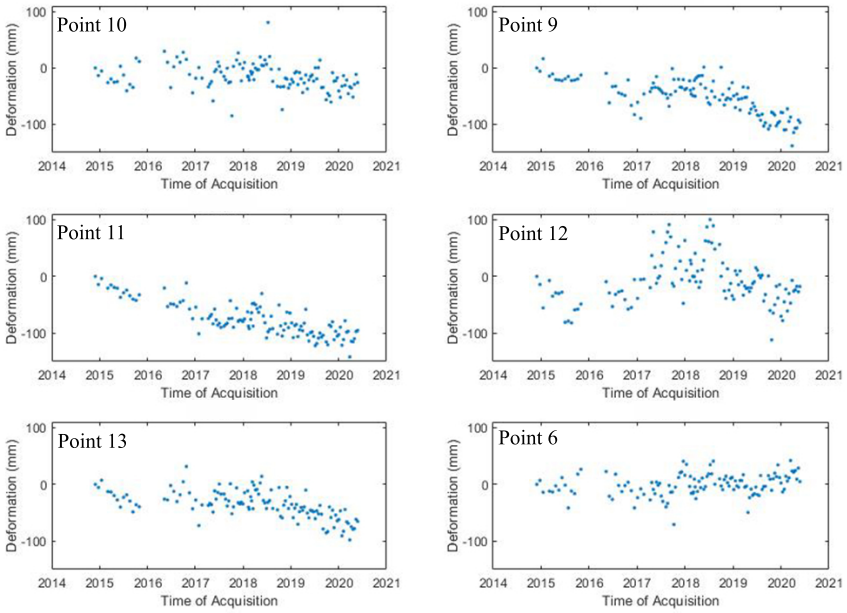

Figure 5.21: Sentinel-1 time series corresponding to pixels presented on Figure 5.19. Points 1-6 & 10 are on the footwall, Points 7-9 & 11-13 are on the hanging-wall.

Most studies about the Chi-Chi earthquake constrained the rheological properties using 15 months (Hsu *et al.* (2002)) of GPS data and seismicity after the mainshock to analyse the postseismic deformation. Tang *et al.* (2019) used 14 years of GPS data within an inverse model and included the impact of Pressure/Temperature to the study of the evolution of stress and strain rate in the lower crust of Central Western Taiwan. They first assumed that a Burgers rheology best fitted the data by extracting two time constants from GPS in the distributed viscoelastic deformation. Their best model is designed by a power-law Burgers rheology with rapid increases in effective viscosities from 10^{17} to 10^{19} Pa.s within a year. Their study suggests that a steady-state creep alone or accommodated by diffusion or dislocation creep cannot explain the deformation, suggesting that an initial transient creep is present within the viscoelastic relaxation. Furthermore, a linear Burgers rheology does not adequately explain the transition between transient and steady-state creep. Their best fit is obtained while using a power-law Burgers rheology with a stress exponent of $n \geq 3$, fitting the GPS data at both early and later stages of the 14 years of postseismic deformation. The early stages following the rupture are explained by a transient non-linear deformation of the material composing the upper mantle and a stress-driver afterslip. Steady-state rheologies underestimate the strain rate at the beginning of the viscoelastic transient and then overestimate it.

In this study, a forward approach based on a power-law Burgers rheology is used

to estimate the afterslip distribution and the lower-crustal strain over the 20 years following the earthquake. The goal of this model is to analyse the impact of the coupling between afterslip and viscoelastic flow, and also, through the analysis of the strain, to get an idea of the state of the current deformation by comparing the postseismic deformation with the pre-earthquake strain rate.

The different steps of the modelling will now be detailed. The postseismic model is realised through *Unicycle* (Unified cycles of earthquakes) (`https://github.com/jdpmoore/unicycle`, `https://zenodo.org/record/4471162#.YPP8N-gzZEY`) three-dimensional model (Muto *et al.* (2019)). The numerical modelling is realised within a 3D rheological structure using an embedded fault surface and volume elements. Stress interactions are evaluated among the embedded fault surface and volume elements with analytic solutions for both displacements and distributed strain caused by viscoelastic deformation of finite cuboids and rectangular dislocations.

- **Forward and Inverse approach**
  Before detailing the model strategy used in this chapter, I will differentiate in a few words forward and inverse approach for modelling.

  Geophysical methods are used to understand and model deformation of the Earth using geophysical data. The modelling can be realised using a forward or an inverse approach, but both depend on the physical properties of the crust and upper mantle. Both methods present challenges and advantages. The main issues, when using geophysical models, are to know how accurate the data are to base the model on and if all the physical mechanisms contributing significantly to the deformation are considered.

  A forward problem can be expressed by (in matrix form):

  $$\mathbf{d} = G\mathbf{m} \qquad (5.27)$$

  d: Geophysical data;
  m: Model parameters;
  G: Operator.

  The resolution of a forward problem enables to determine geophysical data from specific geological structures; however, an infinite quantity of models can be considered. An Earth model and earthquake source have to be known. For validation of the model, the predicted observations can be compared with the observations.

  An inverse problem can be expressed by:

  $$\mathbf{m} = G^{-1}\mathbf{d} \qquad (5.28)$$

  It enables to determine the physical properties of the subsurface based on data. Due to the complex internal structure of the Earth, multiple processes are contributing to the analysed deformation and a large range of rheological

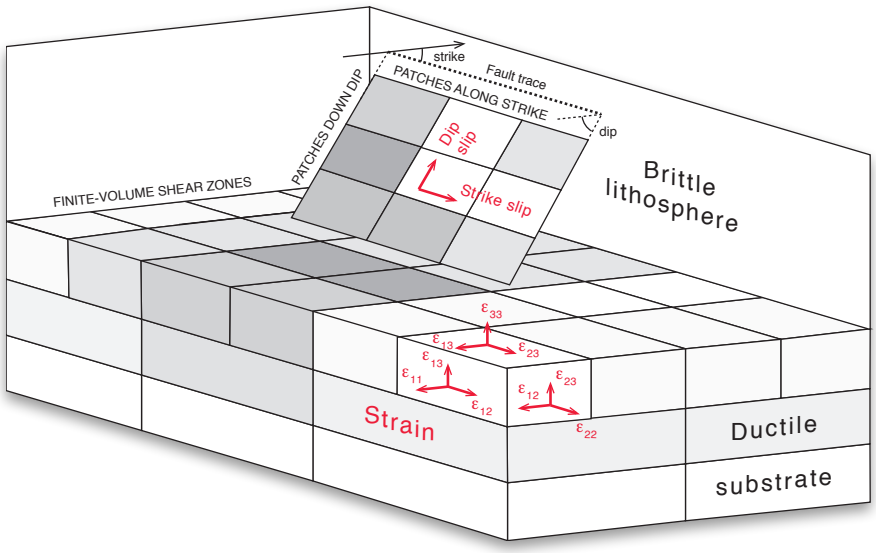

Figure 5.22: Schematic geometric of the upper-crustal fault and lower-crustal strain volumes used in the modelling (Moore *et al.* (2016)).

structures can be considered. Furthermore, to perform an inversion only a few parameters can be inverted at once and a grid-search is performed to find the best-fitting values of these parameters.

- **Definition of the fault and upper mantle geometries.**

  The fault plane is discretized into rectangular sub-patches following the coseismic fault geometry, with patches of 2-km by 2-km. The shear zone is represented by deformable cuboids (each cuboid volume is of $15\text{x}10^3$ m^3 with a thickness of 15 km) described by six independent components of strain (three axial and three shear strains). The shear zone composed of cuboid strain volumes is of 260 km by 45 km by 200 km in the mantle wedge.

  Due to physical reasons (i.e. gaps and overlapping), some pixels had to be pinned (see Figure 5.23), mainly for segments modelling the curved area in the north and the junction between the main segments in depth. According to (Okada (1992)), Green's functions contain singularities in the stress domain, intersecting patches are therefore numerically unstable and cannot be used in any numerical integration scheme which relies on stresses. Any patch with a negative coseismic stress change is pinned.

- **Definition of the afterslip and viscoelastic parameters.**

  The second step is to define the rheological parameters. The inferred rheological parameters determined in Rousset *et al.* (2012) & Tang *et al.* (2019) are

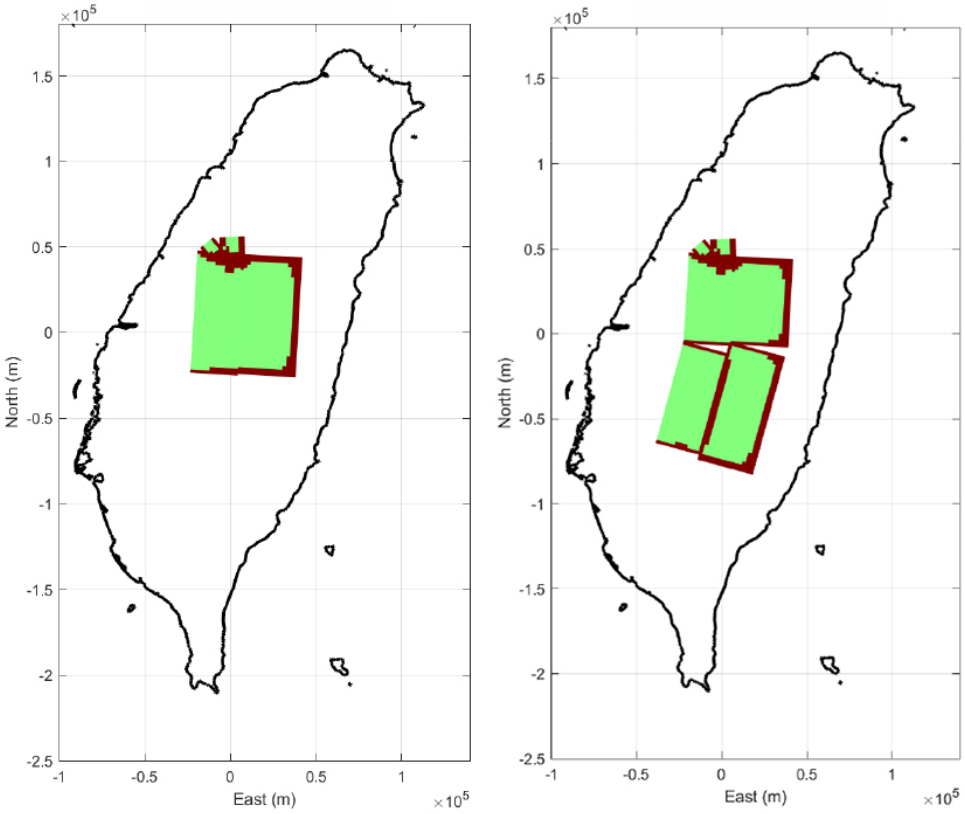

Figure 5.23: Geometry of the fault segments showing pinned pixels (in red) for both geometries tested.

used as a starting point for this model.

The framework enables us to specify heterogeneous rheological properties. The deep lower-crust viscosity is set to 1.5x10^{19} Pa.s and the ductile deformation in the shallower part of the lithosphere presents a viscosity of 1.7x10^{17} Pa.s. In addition, frictional parameters such as a, b and ν_0 were defined (these parameters were described in equation 5.24). In Table 5.2, the final parameter values are presented. In this study, the viscosity is only enabled to vary along depth. According to Tang *et al.* (2019), the variation of viscosity is small over this area and for this study, it can be neglected.

Table 5.2: Model parameters used in this study.

Parameters	**This study**
Steady-state viscosity η_S	1.5.10^{19} Pa.s
Transient viscosity η_T	1.7.10^{17} Pa.s
Frictional parameter a	0.006
Reference afterslip velocity ν_0	0.75 m/yr

Table 5.3: Initial model parameters tested.

Parameters	**Tang *et al.* (2019)**	**Rousset *et al.* (2012)**
Steady-state viscosity η_S	2.10^{19} Pa.s	$0.5–1.10^{19}$ Pa.s
Transient viscosity η_T	1.10^{17} Pa.s	5.10^{17} Pa.s
	Muto *et al.* (2019)	
	Hsu *et al.* (2009)	
Frictional parameter a	0.01	-
Reference afterslip velocity ν_0	8 m/yr	-

- **Test of the forward model and validation using GPS and InSAR TS.**

  Stress interactions are calculated between the fault and the shear zones (description in Figure 5.22) for both displacement and distributed strain due to the viscoelastic deformation of finite cuboids (Muto *et al.* (2019)). The kinematics of the postseismic deformation can be described by slip on fault to explain the afterslip movement, and distributed strain in finite volumes to take into account ductile flow in the lower crust. Then, the evolution of the slip is estimated.

  To obtain the best fit, modifications of the parameters detailed in the previous step had to be done. Several combinations of parameters (Maxwell and Kelvin viscosities, reference afterslip velocity, frictional parameters) were tested to find the best model explaining the postseismic deformation. Looking at the literature and comparing with GPS and InSAR, the values kept were the ones that gave the lower RMS comparing with the observations and respecting the rheology of the area as detailed in previous studies (Hsu *et al.* (2002); Rousset *et al.* (2012); Tang *et al.* (2019)).

  GPS TS and InSAR cumulative displacements are used to compare the predicted displacement outputs. SUN1 and S167 stations were selected for this study as they are positioned close to the fault and with time series covering all the post seismic period studied. Figures 5.25 & 5.26 show the observed and predicted postseismic deformation over 20 years at SUN1 station (situated on the hanging-wall) using model parameters from Tang *et al.* (2019) and then using the final parameters of this study. The initial values are presented in Table 5.3. The RMS (at 1 year, 5 years and 20 years) for this model are summarized in Table 5.4.

  The final parameters of this study are presented in Table 5.2. The RMS estimated at 1 year, 5 years and 20 years are summarized in Table 5.5. The offsets present on the observed GPS TS of SUN1 station were removed to enable the comparison with the predicted data. The first offset present in 2006 corresponds to the effect of a M_w 6 earthquake (offset of 30, -65 and -150 mm were corrected on the east, north and up component respectively) and the second offset corresponds to a 6.2 earthquake (50, -30, -80 mm in east, north,

Table 5.4: RMS for the model using initial parameters.

SUN1 East	**1 year**	**5 years**	**20 years**
	9.4 cm	4.9 cm	4.6 cm
SUN1 North	**1 year**	**5 years**	**20 years**
	1.8 cm	0.3 cm	1.7 cm
SUN1 Vertical	**1 year**	**5 years**	**20 years**
	6.2 cm	11.2 cm	2.8 cm

up respectively).

Figure 5.27 shows the observed and predicted postseismic deformation for S167 station (situated on the hanging-wall) using the final parameters of this study. The RMS estimated at 1 year, 5 years and 20 years are summarized in Table 5.5. An offset presents on the GPS TS in March 2013 was corrected. It corresponds to the effect of a M_w 4.4 earthquake (offset of 22, -36 and -34 mm were corrected on the east, north and up component respectively).

Figure 5.24 shows the observed and predicted postseismic deformation from a pixel localised (24.02N, 120.69E) on the footwall, it was extracted from ERS and Sentinel-1 cumulative displacements using the final parameters of this study (see RMS estimation in Table 5.5). An offset to Sentinel-1 time series was applied to be in the continuity of ERS time series determined thanks to GNSS time series.

On these figures, the component of surface deformation caused by afterslip is showed in green dashed lines, by viscoelastic relaxation in blue dashed lines and the total calculated displacement with mechanical coupling between viscoelastic relaxation and afterslip in solid black lines. An interseismic linear trend has been removed from the GPS data as well as a residual linear trend from the predicted displacement.

Afterslip alone can explain the short relaxation time and amplitude of the displacements. However, in the long-term and particularly for the vertical component, viscoelastic relaxation is needed to fit the data. Also, a mechanical coupling model better fits the data. This aspect will be detailed more in depth in the discussion section of this chapter. The imperfect fit can be attributed to several factors: uncertainties in the source model, geometry of the fault, effects of aftershocks not included in the model, poroelastic relaxation and errors in the removal of interseismic components due to absence of recordings before the event for some stations.

- **Prediction of ground displacements and strain over the viscoelastic layer.**

  Finally, using the integral method, the stress evolution over the 20 years, the slip and strain rates, and frictional state parameters are calculated. The model

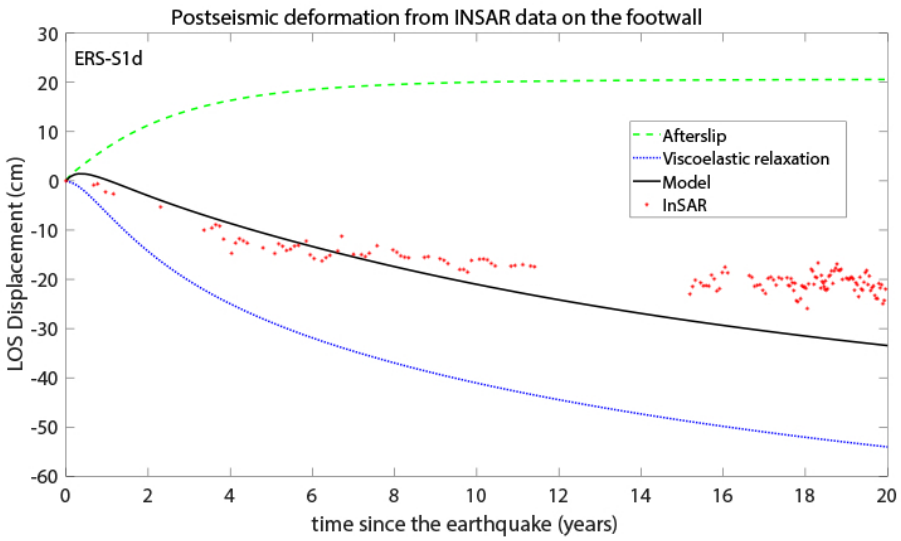

Figure 5.24: Observed and predicted postseismic deformation after the Chi-Chi earthquake from 1999 to 2019. Blue and green dashed lines show the component of surface deformation caused by the viscoelastic relaxation and afterslip, respectively. The black solid lines correspond to the total (afterslip and viscoelastic flow) of the modeled displacement. Red dots indicate InSAR data from ERS and S1-descending TS (location 24.02°N, 120.69°E).

used for the postseismic study of the Chi-Chi earthquake assesses the coupling between both processes, viscoelastic relaxation and afterslip, and estimates their impact in function of the analysed period (20 years of deformation). The outputs will be presented in the next section.

5.5 Discussion

5.5.1 Afterslip distribution

The rupture of the Chi-Chi earthquake was large and induced large afterslip displacements as well as redistribution of stresses in the area of the Chelungpu fault.

Figure 5.28 shows the afterslip distribution corresponding to postseismic deformation over 20 years using the same geometry as the one used for the coseismic study. Afterslip is almost absent in the region of maximum coseismic slip i.e. the curved section at the north of the fault and the main upper segment in shallow depth. Most of the afterslip is happening on the decollement from the middle to the southern part of the segment. These areas showed little deformation during the coseismic event, they were considered as still locked, as all the fault was during the interseismic phase. The maximum of slip of 1.4 m occurs at the junction between the decollement in depth and the main segment of the Chelungpu fault (25 cm of maximum slip was estimated by Hsu *et al.* (2002) after 3 months of deformation).

At first, the same fault geometry was used as for the coseismic study. Then, an

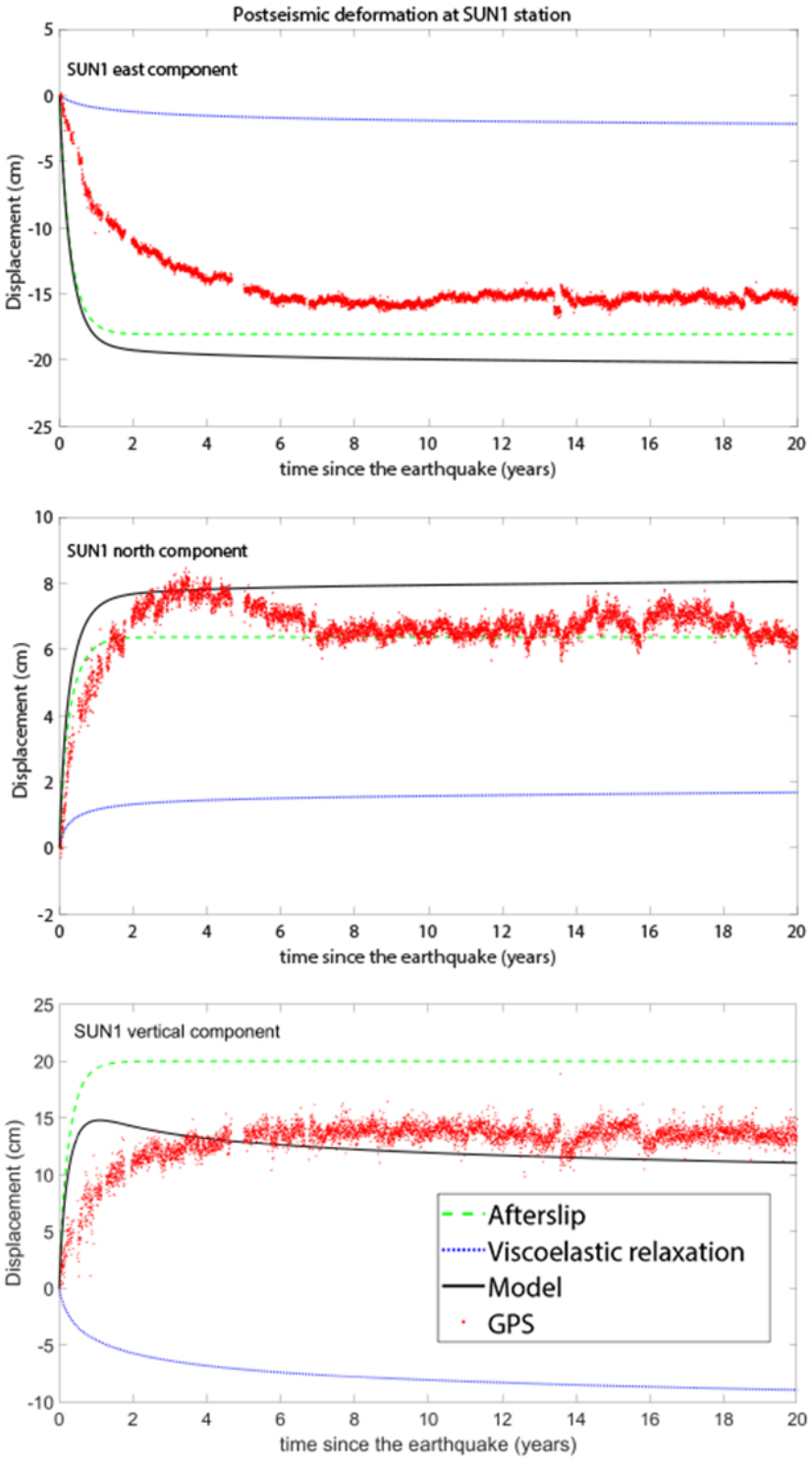

Figure 5.25: SUN1 station observed and predicted postseismic deformation after the Chi-Chi earthquake from 1999 to 2019. Red dots indicate GPS data. (Details in the caption of 5.24). This model was run using the initial values extracted from Tang *et al.* (2019); Hsu *et al.* (2009); Muto *et al.* (2019).

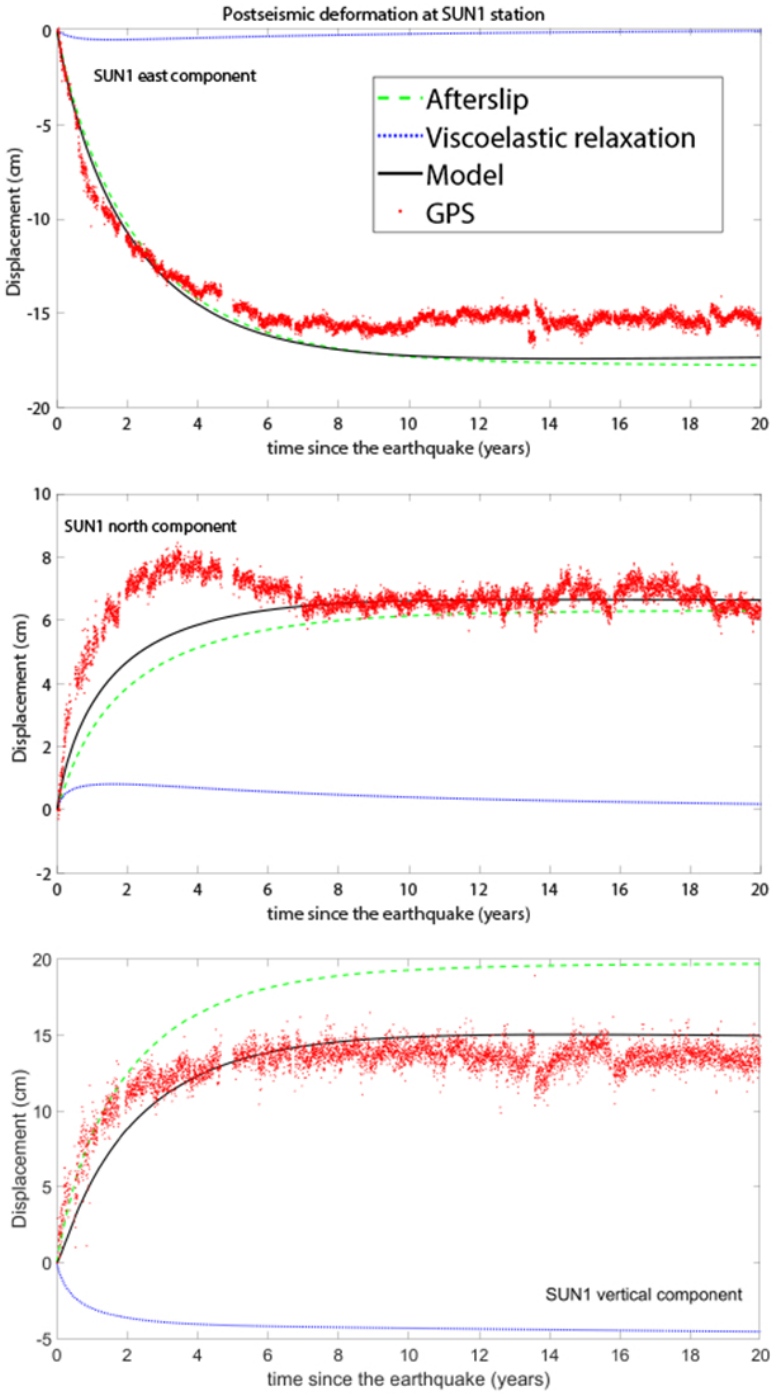

Figure 5.26: SUN1 station observed and predicted postseismic deformation after the Chi-Chi earthquake from 1999 to 2019. Parameters for this final model are presented in Table 5.2. (Details in the caption of 5.24)

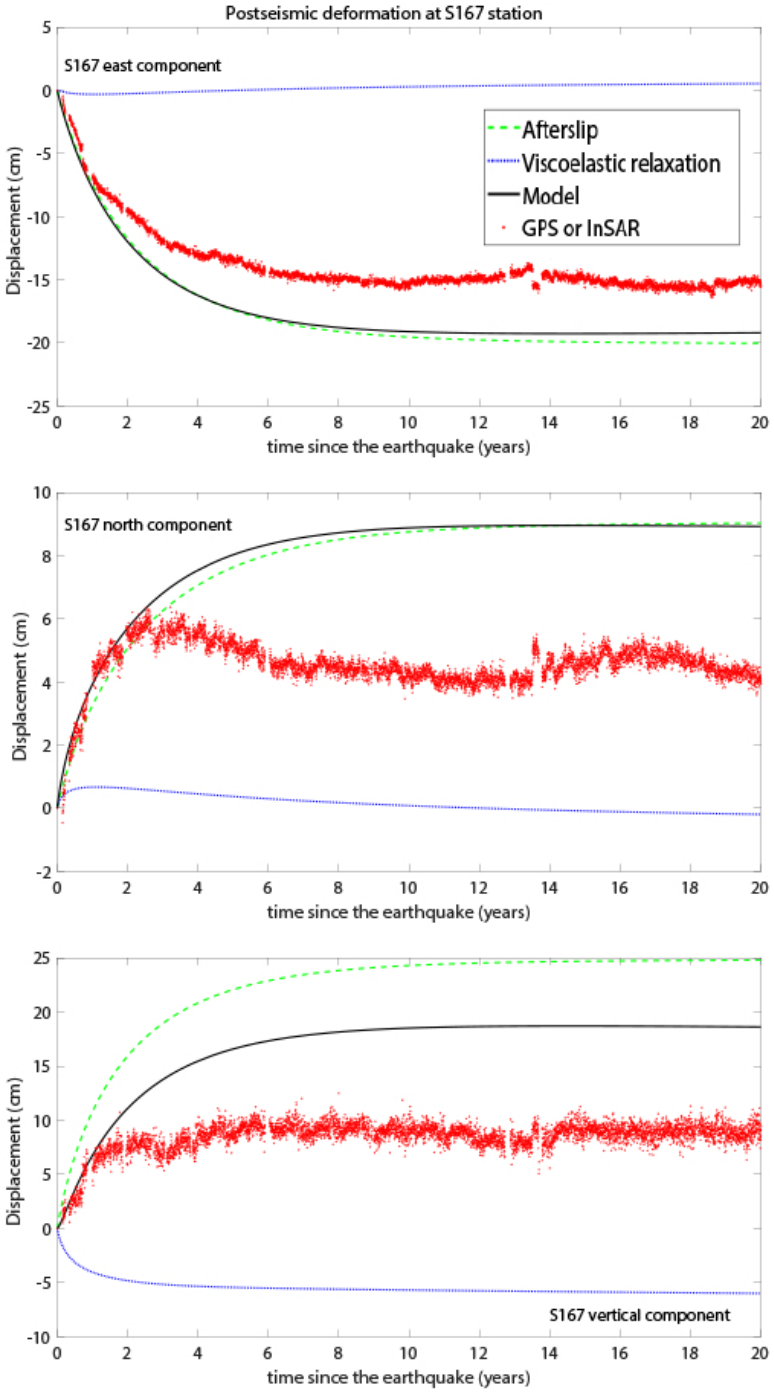

Figure 5.27: S167 station observed and predicted postseismic deformation after the Chi-Chi earthquake from 1999 to 2019. (Details in the caption of 5.24). Parameters for this final model are presented in Table 5.2.

extension of the fault was added to take into account the Tachienshan fault that is in the continuity of the Chelungpu fault in the south in order to detect if this fault was activated by the Chi-Chi earthquake. The larger aftershocks happened in the south part (Figure 5.3). To extend the fault, the assumption is made that the dip angle is the same along the fault strike and that the shallower segments is following the surface rupture. Figure 5.29 is the afterslip distribution including the Tachienshan fault in the geometry. However, small slip is observed on the added segment. This model is suggesting that most of the stress was transferred to the Luliao fault, on the south-east, which is in agreement with (**?**).

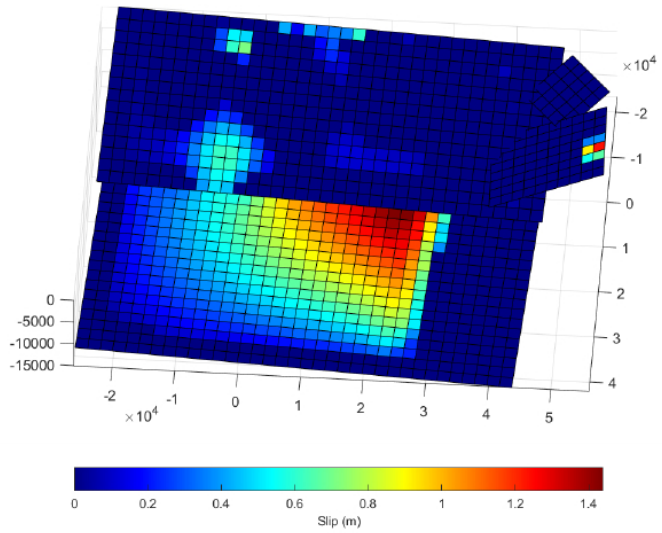

Figure 5.28: Afterslip distribution corresponding to postseismic deformation over 20 years. The same geometry as the coseismic study was used.

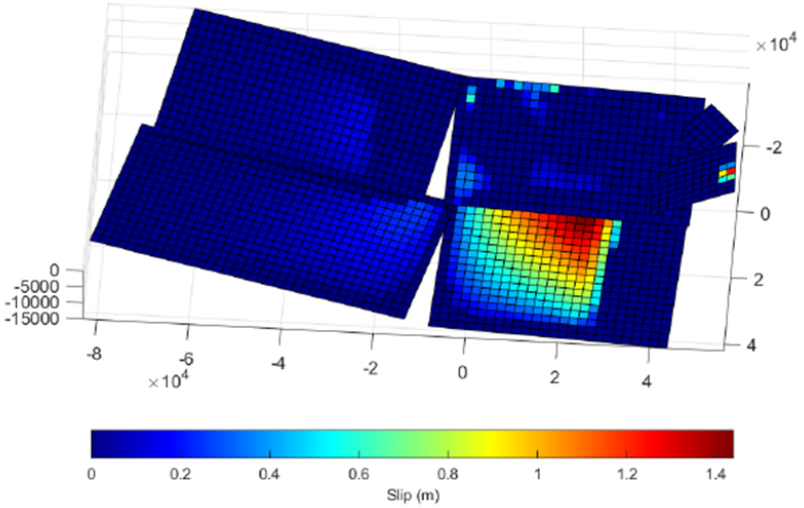

Figure 5.29: Afterslip distribution corresponding to postseismic deformation over 20 years. The geometry incorporating the extension with the Tachienshan fault in the south was used.

5.5.2 Mechanical coupling of afterslip and viscoelastic flow

An analysis was done to assess the importance and relevance of the coupling between afterslip and viscoelastic flow in the case of the Chi-Chi earthquake. In this model, the coupling of these two mechanisms enables two different interactions: viscoelastic relaxation triggered by the occurrence of afterslip and persistent afterslip influenced by viscoelastic flow.

The mechanical coupling contribution was analysed. The comparison of the total predicted displacement with and without coupling was estimated and is presented in Figure 5.30. The black dots correspond to observations, green dots to the model with coupling, blue dots to the model without coupling and red dots to the difference between both. In most cases, the predicted displacement using mechanical coupling gives a better fit to the model run without interactions between afterslip and viscoelastic flow.

Table 5.5 shows the RMS for each component at the three locations presented before (Figures 5.26, 5.27 & 5.24) using a model with coupling and without coupling between afterslip and viscoelastic flow. From these analysis, coupling does not have much impact on the model for the first months/years, the RMS are close. However, after about 3-4 years and after 20 years, coupling is needed to best fit the data. The importance of the coupling increases in the long-term.

Table 5.5: RMS for each model using or not mechanical coupling (values in cm).

S167 East	**1 year**	**5 years**	**20 years**
With coupling	0.7	4	4.2
Without coupling	1.065	5.7	6.7
S167 North	**1 year**	**5 years**	**20 year**
With coupling	0.4	2.7	4.8
Without coupling	0.23	3.6	6.3
S167 Vertical	**1 year**	**5 years**	**20 years**
With coupling	2.3	7.5	9.7
Without coupling	1.4	5.3	5.0
SUN1 East	**1 year**	**5 years**	**20 years**
With coupling	1.7	1.48	2.2
Without coupling	1.4	3	4.5
SUN1 North	**1 year**	**5 years**	**20 years**
With coupling	1.8	1.7	0.4
Without coupling	1.6	0.9	2
SUN1 Vertical	**1 year**	**5 years**	**20 years**
With coupling	1.6	0.4	1.6
Without coupling	2.3	2.2	2.2
InSAR	**1 year**	**5 years**	**20 years**
With coupling	2.2	3	11.5
Without coupling	6.7	11.7	1.7

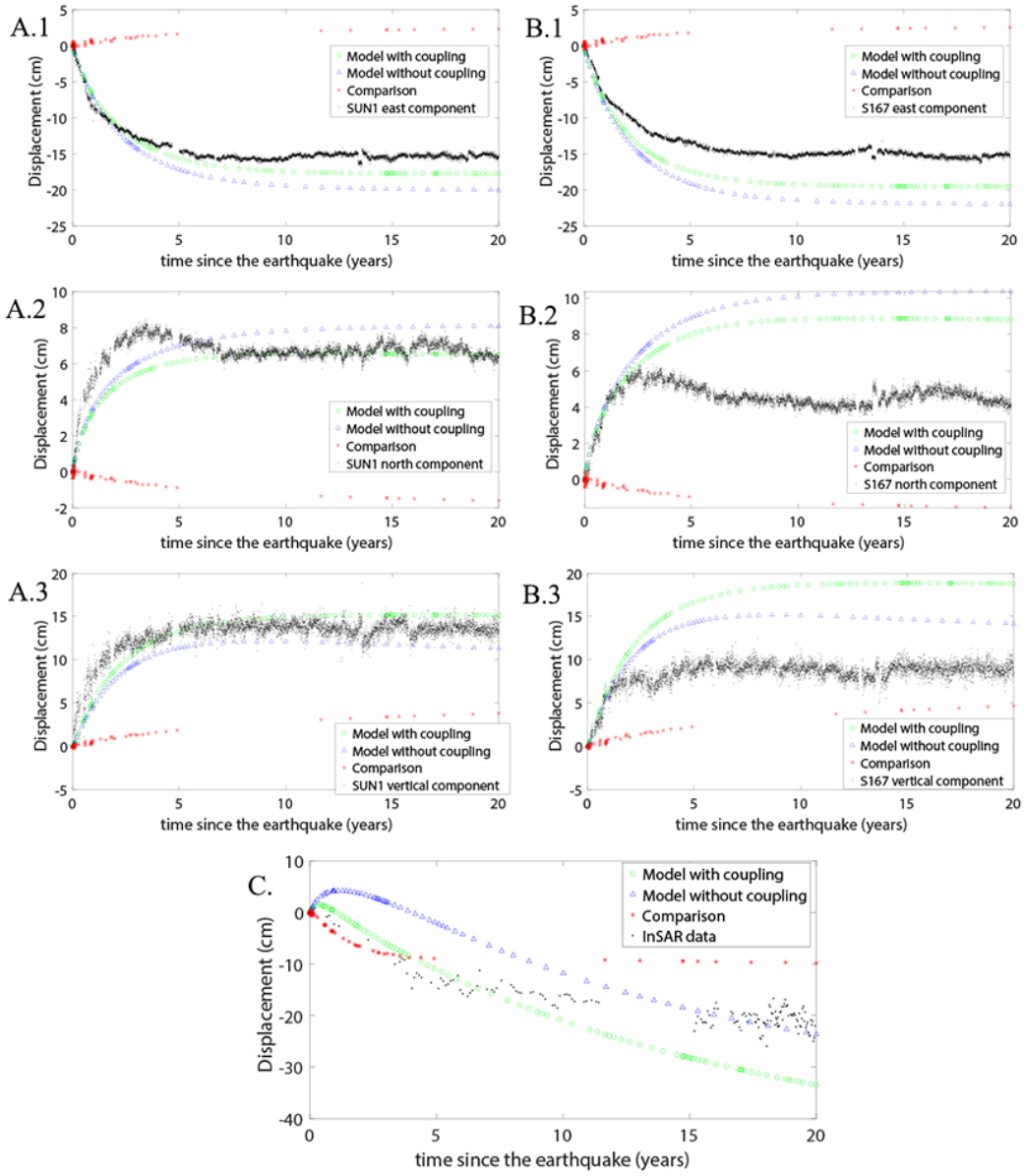

Figure 5.30: Comparison of the model outputs with and without coupling interactions. A. SUN1 station B. S167 station C. InSAR pixel (1. east, 2. north, 3. vertical component). The black dots correspond to observations, green dots to the model with coupling, blue dots to the model without coupling, red dots to the difference between both models.

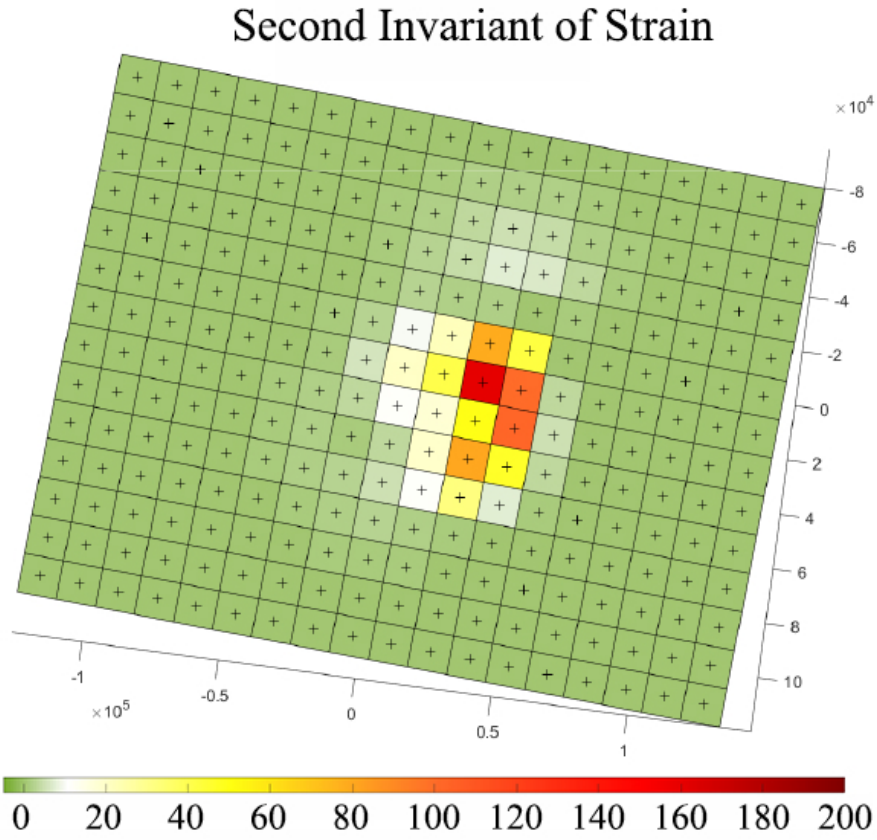

Figure 5.31: Second invariant of strain estimated from the accumulated strain over 20 years (in μ strain). This corresponds to the geometry of 5.28.A. at the top of the lower-crustal strain volumes.

5.5.3 State of the deformation

Figure 5.31 presents the second invariant of strain calculated from the accumulated strain estimated in our 20 year model and Figure 5.32 presents the dilation and shear strain. Accelerated strain is present below areas of maximum slip. No pre-earthquake stress was defined in the model to represent the interseismic loading, this is explaining the null values outside of the fault area. The comparison of the second invariant of strain with the slip distribution shows that the larger strain is below the larger afterslip area. The pre-strain rate was estimated at 4.1x10^{-7} μstrain.yr^{-1} (Tang *et al.* (2019)). 20 years after the earthquake, the maximum strain rate is of 2.5x10^{-7} μstrain.yr^{-1}. Hence, the transient period seems to be finishing, the Chelungpu fault is locking again, some parts, close to the fault in the south end, can still be adjusting. More data with long time span and a denser network would be needed to conclude on the non-linear or linear behaviour of specific areas. The analysis of the TS from Sentinel-1 shows a linear behaviour of the deformation.

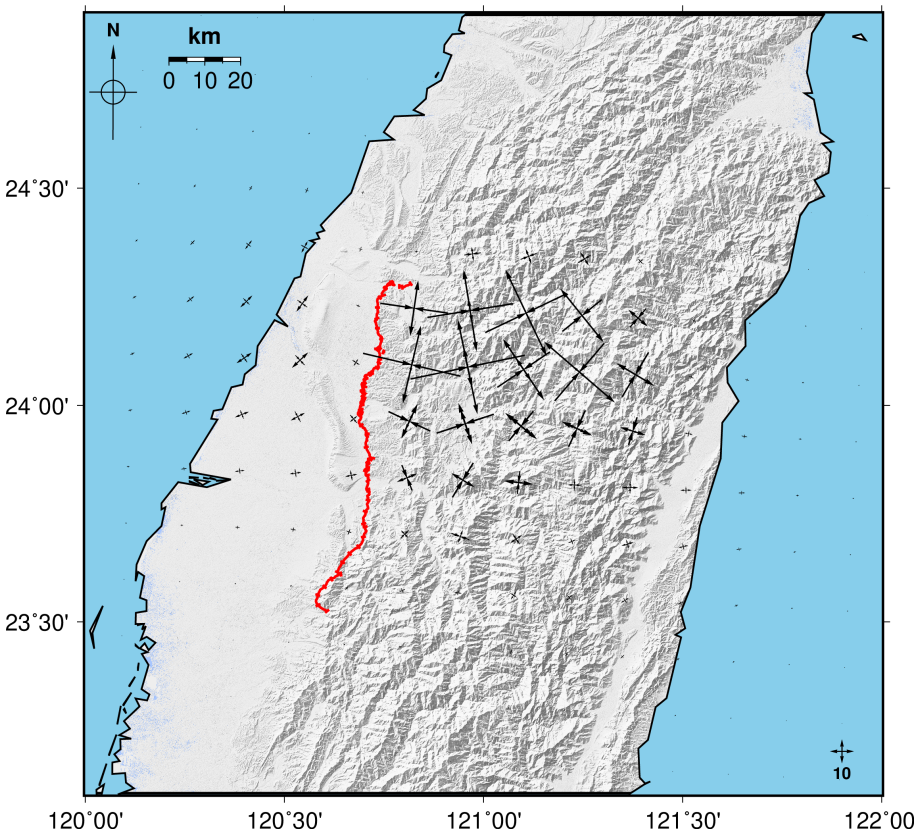

Figure 5.32: Dilation and shear strain along the 2nd invariant of the strain tensor (legend in /yr). This corresponds to the geometry of 5.28.A. at the top of the lower-crustal strain volumes.

5.6 Summary

InSAR and GPS data were used to obtain measurements of the postseismic deformation following the M_w 7.6 Chi-Chi earthquake in Taiwan. A similar deformation field was obtained in comparison with previous studies (Hsu *et al.* (2002); Rousset *et al.* (2012); Tang *et al.* (2019)) but over a longer period and using a forward approach. Furthermore, more precision was achieved thanks to powerful processing techniques enabling me to carefully correct for atmospheric and unwrapping errors, largely present during InSAR processing. Moreover, InSAR was not previously used to study the postseismic deformation of the Chi-Chi earthquake. In this postseismic study of the Chi-Chi earthquake, a TS analysis was done over the entire area to detect any change in the deformation over 20 years from GPS and InSAR. Then, a forward model was built to analyse the contribution of afterslip and viscoelastic flow to the postseismic displacement as well as the contribution of mechanical coupling to explain this specific case. The afterslip distribution was analysed using the same geometry as the coseismic study as well as including the Tachienshan fault in the south end of the Chelungpu fault. Finally, combining the analysis of the TS and the estimation of the strain rate, a conclusion concerning the state of the deformation of the Chelungpu fault was achieved.

ERS data was particularly useful to observe the displacement over the first 11 years of the postseismic deformation. ERS and GPS TS show a variation of the deformation in 2004 in the near field. In the far field of the footwall, it is more challenging to detect a variation of the deformation due to smaller displacement during the earthquake. The cumulative displacements over the last 5 years shown by Sentinel-1 data do not present any clear deformation. However, the linearity of the deformation suggests that most or all of the area is locked, as it was before the earthquake.

A forward model was run using Unicycle, and the geometry of the fault and slip distribution obtained in the coseismic joint inversion (see Chapter 4). The predicted deformation caused by afterslip and viscoelastic relaxation alone or with mechanical coupling was compared with GPS and InSAR observations. The first years of postseismic deformation are dominantly produced by afterslip on the hanging-wall. Then, the contribution from viscoelastic relaxation is more present, especially for the vertical component. On the footwall, I observed that the contributions from both mechanisms are needed to explain the deformation. This approach enabled me to conclude the importance of the mechanical coupling between afterslip and viscoelastic flow for this event especially to explain long-term of postseismic relaxation.

The coseismic slip distribution shows the maximum of slip on the north part of the fault, mainly on the curved section. In the case of the postseismic deformation, most of the slip is happening on the south part of the main segment, on the decollement at depth. However, several other seismic events with high magnitude, creeping and aseismic slip happened at neighbouring faults (Luliao, Changhua or Tachia faults) are disturbing the understanding of this specific event in addition to

postseismic mechanisms presenting complex and numerous processes with behaviour varying in time and space.

From the analysis of the strain accumulated during the 20 years of deformation, an insight on the status of the deformation can be achieved. The post strain rate ($2.5\text{x}10^{-7}\ yr^{-1}$) is close to the interseismic strain rate ($4.1\text{x}10^{-7}\ yr^{-1}$) estimated before the earthquake. After 20 years of transient deformation, the area of the Chelungpu fault is locking again which suggests that the interseismic period has started. Only some areas close to the rupture, on the south part of the fault, seems to be still adjusting. However, to validate this hypothesis, more data would be needed.

Full earthquake cycle processes are still quite unknown due to the complexity of each phase of deformation and the number of additional processes and micromechanisms that have to be taken into account as well as the knowledge of the rheology of the area studied. This study has once more shown the strength of geodetic observations especially InSAR as well as the necessity to build strong models of fault enabling to understand which part ruptured during the main event and which areas are locked or are deforming aseismically. This mechanically coupled model of afterslip and viscoelastic flow shows the interplay between those two mechanisms to explain complex events such as the Chi-Chi earthquake.

Chapter 6

Discussion and Conclusions

In this thesis, the coseismic and postseismic deformation of the M_w 7.6 1999 Chi-Chi earthquake have been investigated using several Earth observations (GPS, InSAR, optical sub-pixel correlation and levelling). I started by introducing the earthquake cycle principle and Earth Observations (EO) in Chapter 1 followed by the motivation and aims of this research work. The previous research analysing the different phases of earthquake cycle corresponding to the Chi-Chi event were detailed in Chapter 2 as well as the tectonic context of Taiwan. The principle of SAR and InSAR techniques were summarized in Chapter 3 followed by the principle of optical imagery and GNSS. The coseismic study was presented in Chapter 4. My research focused on building a methodology to combine five EO types to analyse more precisely the fault geometry and slip distribution of this well-known event by estimating relative weights and selecting EO in function of their strengths and weaknesses in regards to this study area. This methodology is particularly useful in areas presenting complex conditions (tropical climate, dense vegetation steep topography) or for past events (only covered by few data or with low coherence) which precise understanding would be useful. Then, the postseismic deformation study was performed in Chapter 5. The deformation of Central Western Taiwan during the 20 years since the earthquake happened was analysed using InSAR time series extracted from ERS, EnviSAT and Sentinel-1A/B, and GPS time series. The afterslip and viscoelastic relaxation mechanisms running the deformation following the rupture were modelled using a forward approach. In this final chapter, I will discuss the contributions of this thesis focusing on EO strengths and earthquake cycle deformation, as well as the implications of this work for future studies.

6.1 Contributions of this research

6.1.1 Research motivation

Earthquake cycle

Seismic hazard over continents is a challenge and most techniques commonly

used often fail to precisely assess the deformation, especially in areas struck rarely by earthquakes. Usually, earthquakes happen on any individual fault every several hundreds of years or even more. However, the observations recorded only cover a few years or decades. Hence, models of the deformation of fault zones in time and space are needed. In addition to the difference between observation times and earthquake repetition period, plate deformation zones are covering hundreds of km^2. On each plate, several active faults on different scales are deforming the area. Finally, tectonic structures are not all known, and the structure of the crust and upper mantle is still not fully understood. Using observations of the surface deformation over the rupture period and between events is an efficient solution to update hazard maps. Earth observations are hence used to measure tectonic deformation.

Fault zones deform following a quasi-cyclical behaviour composed of the interseismic, coseismic and postseismic phases. However, the inter- and post-seismic phases can be hard to differentiate. The coseismic deformation presents the most rapid deformation of the earthquake cycle (in space, the interseismic deformation is actually larger considering inelastic/aseismic deformations) and is getting easier to model thanks to EO used to constrain earthquake source geometry and slip distribution. This deformation happens on short-time scales (usually a few seconds or minutes) with structures deforming as an elastic solid. The postseismic deformation corresponds to an adjustment period of the crust and mantle due to the coseismic stress changes. The study of this transient phase is primordial to understand the rheology of the ground and detect in time and space the distribution of the deformation. This phase of earthquake cycle is the hardest to model due to the number of mechanisms which operate simultaneously or independently. The gradient of postseismic deformation can vary from event to event. In some cases, it is equivalent to the magnitude of the interseismic deformation while it can represent a small fraction of the coseismic rupture.

Three main mechanisms are responsible for the postseismic deformation: aseismic slip (afterslip controlled by friction) usually occurring on areas of the fault that did not rupture during the coseismic phase, viscous flow of the lower crust and upper mantle depending on several parameters such as viscosity, stress and grain size, and finally, poroelastic deformation (this contribution was neglected following Rousset *et al.* (2012) that estimating it at less than 10% of the deformation). Afterslip and viscoelastic models are needed to explain in depth the postseismic deformation. The interseismic deformation is the longest phase and occurs between earthquakes after the transient postseismic deformation. During this period, parts of the fault in the crust and upper mantle are locked. However, an accumulation of strain is happening due to tectonic plate motion moving steadily each side of the fault.

The earthquake rupture is defined by a release of strain energy that has built up during the interseismic phase. Considering this, earthquakes will occur where a maximum of strain energy has accumulated. Therefore, the earthquake cycle study is based on the development of models that can link the short-term observations of strain to the long-term fault deformation. In order to predict potential areas of

future rupture, precise knowledge of the location of active faults is essential as well as sections accumulating strain within the crust.

Earth Observations

EO have dramatically improved in the last decades and can measure the different phases of earthquake cycle and help constrain the potential sources of seismic hazard. The number of EO satellites is expanding and open data policies have helped greatly in the development of their applications. Furthermore, the variety of satellite characteristics (for instance, the variety of wavelengths) is opening the possibilities. The reduced revisit time increases also the level of interferometric coherence which highly improves measurements of surface deformation TS. EO enables us to measure and understand earthquakes and shallow crustal tectonics and improve the knowledge of active fault sources generating earthquake shaking hazards. In the majority of earthquake cases over the globe, the very dense sampling of InSAR with cm precision makes it the best strategy to follow. Only optical offset can compete with this technique but only for large horizontal offsets. Most models have been built only using GPS, however precise features of the earthquake cannot be achieved with GPS-only models due to the lack of dense observations in the near field. Even though GPS networks are getting denser all over the world, it is often not enough to properly constrain a model.

InSAR is a powerful tool to study earthquake linked deformation. It is becoming the most efficient way to detect earthquake and monitor the deformation. Sentinel-1 data has lifted the study of earthquakes and tectonics into a new era: images covering hundreds of kilometers wide are produced with pixel resolution of 5 m by 20 m and a revisit time as little as 6 days in most tectonic regions. This is improving the quantity and quality of observations. ERS and EnviSAT present 35 days revisit time, hence the coseismic deformation analysis can be disturbed by postseismic deformation (that cannot always be corrected precisely using GNSS). More phenomena and smaller deformation can be observed such as creeping. Long times series can be observed combining ERS launched in 1991, EnviSAT and Sentinel-1 data which is still recording but also thanks to GPS network expanding all over the globe. The constant improvement of the techniques for processing and corrections (atmosphere, orbit or unwrapping) are making the revisit of past events possible. However, decorrelation is a regular problem in non-urban environment for short-wavelength satellites.

However, other EO should not be neglected over InSAR and still present large advantages. GNSS permanent stations should keep being installed over seismic areas to densify networks. Its high temporal resolution is useful to analyse deformation (estimate velocity fields over continental ground or to estimate strain rate) but also to validate SAR and optical processing such as I did for the postseismic SAR TS. In contrary to seismic data, GNSS can detect and measure slow slip such as happening during the interseismic phase and which is not generating seismic shaking. Also, GNSS could be able to detect foreshocks or any pre-earthquake deformation.

Furthermore, while seismometers saturate in amplitude, GNSS can measure strong ground motion and can be efficient in real-time monitoring of a developing earthquake. However, its sparse distribution of stations is limiting its applications.

Furthermore, a large quantity of satellites with different wavelengths are freely accessible nowadays enabling different studies. For instance, longer wavelength satellites can record images over vegetated area (such as L-band SPOT or ALOS). Optical imagery possesses some advantages in comparison to InSAR. However, it requires cloud free daytime conditions of acquisition and it is predominantly useful over large offsets. Sub-pixel correlation technique can be used with radar amplitude and optical images, offsets measurements can be used to identify the location of an event, understand the rupture and constrain the fault geometry and slip distribution for coseismic rupture and in the case of afterslip and viscous relaxation.

Moreover, for the future research, insights for hazard assessment could be obtain thanks to the new generation of satellites such as Sentinel-1C or ROSE-L as well as the combinations of GNSS constellations (Galileo will be fully operating in 2024 and adding to GPS and GLONASS), enhancing capabilities and improving accuracy of velocities calculated.

Finally, the common advantages of EO is that it does not require a team onsite and it is not intrusive for the local population.

Taiwan seismic hazard

The Central Western part of Taiwan is rarely struck by large earthquakes as presented in Chapter 2. Contrary to the south and east sides of the island, only three major earthquakes struck the area in the last 100 years but with devastating impact for the population and infrastructures; the largest cities of the island being situated on the west side. 23.5 million people are currently living on the island. Furthermore, several active faults are present and interplay with each other complicating the deformation following one event. The quantity of active faults in addition to the two subductions present make Taiwan one of the most important tectonic area in the world to study.

Furthermore, only a few cases of earthquake cycle in the world could be studied entirely using EO (Chlieh *et al.* (2004); Remy *et al.* (2016)). The Chi-Chi earthquake represents a great opportunity to improve techniques of earthquake modelling and test methodologies. This specific event enables to get understanding of the strain accumulation over this area thanks to more than 20 years of observations. Even though the constrain of seismic hazard using short-term EO is challenging due to the number of unknowns, the large number of models build on the coseismic rupture enables to study the postseismic deformation based on solid fault geometry and rheology. Understanding each phase of the earthquake cycle for Taiwan is already a priority but also the knowledge that can be transferable to other areas of the globe has influenced the choice of this area as a study site.

I will summarize in the next sections, my work done on the co- and post-seismic phases of the Chi-Chi earthquake.

6.1.2 Coseismic modelling using EO

In Chapter 4, I used several EO to study the coseismic rupture of the Chi-Chi earthquake in Central Western Taiwan. Each EO data set was carefully selected to overcome difficulties of the ground (for instance, presence of dense vegetation and steep topography), limitations of the capabilities of one data set or to complement GPS and InSAR (the two main techniques used nowadays to study earthquake rupture). Three interferograms were processed, covering the footwall of the Chelungpu fault. However, the hanging-wall presenting the major deformation, largely covered by dense vegetation, was non-coherent. To get information on the hanging-wall, optical images from SPOT 1-2 satellites were processed. GPS, levelling and benchmarks data were used as presenting a high temporal resolution and bringing more constrain to the model on the complex segments of the fault. The Taiwan GPS network, even if not presenting a dense network in 1999, possesses stations over the full study area. Benchmarks were used to constrain the model in the curved part of the northern segment and levelling was constraining the model with precise vertical displacement in the central section of the fault.

Before the joint inversion realised with PSOKINV (Particle Swarm Optimization and OKada INVersion package), relative weights among the data sets and spatial constraint were estimated using gABIC (generalized Akaike's Bayesian Information Criterion). The geometry of the fault was based on the previous model of Johnson & Segall (2004) and adjusted with the selected data. The analysis of the slip distribution using the relative weights estimated by gABIC showed the necessity of running a similar step before any joint inversion using more than two data sets. The results of the inversion showed that the slip distribution is mainly determined by the GPS as presented in previous papers. This is mainly due, in this specific case, to the non-coherence of InSAR over the hanging-wall (area of major coseismic displacement) and the large uncertainties present in the SPOT offsets. However, the incorporation of other geodetic observations constrain the model, especially on the curved part at the north of the fault. The final model using all the data sets and the gABIC relative weights shows that the maximum slip was of 12.6 m on the north curved part of the fault with a seismic moment of 3.9 x 10^{20} N $\cdot$ m, corresponding to a magnitude of M_w 7.6. The study of the moment and Coulomb stress changes show that most of the slip happened on the north part of the fault at shallow depths (less than 4 km) and that most of the energy released by the event was transferred to the faults at the north of the area, which is the most probable location of a future event.

The study of the Chi-Chi coseismic rupture was a challenge, as the precision and coverage of the data sets available are quite poor as well as the complexity of the topography and atmospheric conditions. A few improvements could still be realised on the slip distribution analysis as well as the establishment of a methodology for joint inversion of EO. However, some limitations of the data sets and tools put to my disposition could not be overcome. First, concerning the representation of the fault, the rectangular division of the fault into four segments of rectangular patches

was debated concerning the large gaps that it is leaving as well as overlapping areas. Second, concerning the optical images processing, large uncertainties were present in the final optical offsets. Several softwares were tested as well as GPS data used to precisely coregister the images but still uncertainties remained. The relative weighing used in the model was then low in comparison to the GPS one. However, even though in this case the strength of optical images was not particularly shown, it is easy to see their advantages as a complement to InSAR or replacement when dense vegetation is present.

I showed in this work that it is feasible to combine several data sets and the advantages that it is bringing to constrain the model. This workflow can be followed while revisiting events modelled using GPS only or in complicated areas similar to Taiwan's. It can also be useful in areas that have a high resolution and coverage. Even with the increase for SAR revisit time, several days are still needed to obtain an image before and after an event. In a large number of cases, the earthquake community still encounter issue in understanding the rupture and the strain accumulation using only GPS or InSAR.

6.1.3 Postseismic study using InSAR and GPS

In Chapter 5, I used GPS and InSAR data to study 20 years of postseismic deformation following the Chi-Chi earthquake of 1999. Several GPS stations were recording before or since the earthquake until now, enabling to obtain the horizontal and vertical displacement during the last 20 years and to validate the postseismic model. InSAR TS were generated in order to obtain a better spatial coverage than GPS. ERS, EnviSAT and Sentinel-1 satellites images were processed. However, only descending tracks could be used (very few images were available from the ascending tracks). GACOS atmospheric corrections were applied as well as a phase closure analysis to detect unwrapping errors, increasing the precision of the outputs. Finally, GPS was used to validate the InSAR time series and the model. I also analysed seismicity and levelling data over the area.

First, an analysis based on Earth observations time series was realised to obtain the deformation over Central Western Taiwan and in neighboring areas of the Chelungpu fault since the Chi-Chi earthquake. From both InSAR and GPS, a transient period is observed until about 2004 (depending of the location of the pixel analysed in comparison to the fault, in the far field or near field).

Second, a forward model was used to study both the afterslip and viscoelastic flow using a non-linear Burgers rheology and the coseismic stress. The predicted displacements were compared with GPS and InSAR time series to validate the model and rheology used. At first, on the hanging wall, the deformation is mainly explained by afterslip. Then, the contribution of viscoelastic flow is needed. On the footwall, both mechanisms are needed from the beginning of the postseismic deformation to fit the data.

While the coseismic rupture mainly happened in the north section of the fault and

at shallow depth, the majority of postseismic deformation is happening on the south segment at depth, on the decollement. The maximum slip of 1.4 m happened on the central part of the decollement. From the afterslip distribution, the Tachienshan fault does not seem to have been reactivated by the rupture, most of the stress was transferred to the Luliao fault, on the southern end of the Chelungpu fault but to the east as discussed in the literature.

Third, the contribution of mechanical coupling was studied. Two interactions are allowed in Unicycle: viscoelastic relaxation triggered by the occurrence of afterslip and persistent afterslip influenced by viscoelastic flow. The analysis showed that mechanical coupling is needed to explain long-term deformation. However, the first years can be as well explained with and without it. Finally, from the analysis of the strain and the comparison with studies of the interseismic period before the event, it seems that the interseismic deformation started in the far field and for most of the near field. Only areas close to the fault in the southern section, might still be adjusting. A more complex rheological model could be tested to better model Taiwan lithosphere considering poroelastic relaxation and micromechanisms such as creeping (diffusion and dislocation creep).

6.1.4 Research aims and objectives revisited

I will now return to the aims and objectives stated in the introduction of this thesis and evaluate progress against each of them. The main aim was to improve the understanding of the deformation of Central Western Taiwan using Earth observations focusing on the deformation of the Chelungpu fault. It is an active fault situated in a densely populated area and whose rupture had a devastating impact on the population and infrastructures.

O1. Develop a methodology for coseismic modelling integrating multiple data sets.

I have processed and analysed five types of EO (GPS, SAR images, optical images, benchmarks and levelling) and built a methodology to run a joint inversion of these data sets in order to interpret the coseismic event of the Chi-Chi earthquake. Each data set overcomes a difficulty link to atmospheric conditions, characteristics of the data set or constrain to the model. The complexity of the ground, steep topography and dense vegetation, made the InSAR processing difficult especially for the unwrapping step and required to find solutions to obtain an overview of the entire fault, in this case using optical images. The main improvement of this model is the addition of the weight determination. The joint inversion using relative weights showed to be essential to the model. It enables to consider the uncertainties of each data set (for instance, the weight of the SPOT offset was reduced due to large uncertainties) but also to constrain the model accordingly.

The main outputs of this objective are: first, a joint study of the different types of EO which show clearly that it is important to analyse and select carefully the

data. Second, that, in many cases, combining radar and optical gives a lot more information and enable to study vegetated and urban area at the same time. Furthermore, using GPS with high temporal resolution and InSAR with high spatial resolution is complementary.

O2. Model afterslip and viscoelastic relaxation induced by the Chi-Chi earthquake.

I have processed InSAR time series from ERS, EnviSAT and Sentinel-1 data correcting tropospheric errors and carefully checking for unwrapping errors. GPS time series were also analysed to study the 20 years of postseismic deformation following the Chi-Chi earthquake. From time series, a decrease of the displacement is observed around 2004. A forward model was run to analyse the afterslip and viscoelastic flow mechanisms running the deformation following the rupture. The model showed that both afterslip and viscoelastic relaxation are needed to explain the postseismic response to this rupture and that mechanical coupling between those two mechanisms is necessary for long-term study of the Chi-Chi postseismic deformation. From these observations and the estimation of the strain rate, the interseismic phase has started over most of the area.

O3. Analysis of the deformation of Central Western Taiwan during the Chi-Chi event of 1999 and since using Earth Observations.

Taiwan has complex geological settings and presents a high seismic risk. Similarly to other areas in the world frequently struck by large earthquakes, a precise monitoring is required as well as a precise knowledge of active faults and their rheology. In this purpose, an analysis of the different stages of earthquake cycle is required as well as linking each phase together.

The collocation of information from previous studies, the analysis of each phase of the earthquake cycle using EO as well as the extraction of additional information from seismicity enable to obtain a clear and large view of the situation of Central Western Taiwan and to study in its continuity the deformation. Furthermore, the movements of the Eurasian and Philippine Sea plates deforming Central Western Taiwan complicate the specific study of the Chelungpu fault deformation. Furthermore, some of the neighboring faults seem to have been reactivated during the coseismic rupture in the north, or that part of the stress was transferred during the large aftershocks on the south east side of the Chelungpu fault.

The analysis of interseismic, coseismic and postseismic geodetic data provides an overview of the earthquake cycle in Taiwan. The coseismic rupture happened mainly in the north part of the fault with shallow slip while the postseismic deformation is happening mainly at depth on the decollement and in the south segment of the fault. The motion is returning to an interseismic state.

This work showed the potential for GPS and InSAR to provide a thorough picture of the deformation in both time and space. However, interseismic deformation close

to the fault remains uncertain and longer observation time span will be required to better constrain this aspect of the seismic cycle. I have shown how InSAR can be used as a useful tool in earthquake deformation analysis, but also that other measurements are necessary to add further constraints to models. Interdisciplinary research teams would have been useful to generate the most appropriate model.

From the resolution of these objectives, the following research innovations can be extracted.

RI1. Development of a methodology for joint inversion using relative weight estimation.

RI2. Combination of several Earth Observation data and improvement of their precision thanks to precise correction of errors.

RI3. Analysis of two decades time span of postseismic deformation to access the state of the deformation.

RI4. Evidenced mechanical coupling between afterslip and viscoelastic relaxation.

6.2 Implications and Future work

Taiwan is a particularly interesting study site for active tectonics and it is essential to gather information about the deformation due to the highly populated cities in neighbouring areas of active faults. However, the island presents a steep topography, areas of dense vegetation and a tropical climate that complicates the use of satellite data.

Due to these complications, InSAR was not particularly used in Taiwan at the time of the Chi-Chi earthquake or during the decade that followed. Thanks to the improvements of the techniques in the last years, I was able to use InSAR over this specific area. Several other study sites over the globe could benefit from a similar study.

Furthermore, the large offset of displacements created by the Chi-Chi earthquake enable to build methodologies for EO processing and modelling. Precisely understanding each phase of the earthquake cycle by characterizing the time evolution of slip is essential in the purpose of understanding the factors controlling the repetition of events. A precise understanding of past events is essential to analyse the distribution and accumulation of stress in the lithosphere. Studying large earthquakes with precise data and efficient techniques enable to model the geometry of fault (an improvement of the model could be achieved using a triangular dislocation) and to estimate the distribution of slip. Only a few large events happen each decade, hence their study is essential to build hazard assessment.

To conclude this thesis, the study of the coseismic deformation for the Chi-Chi earthquake enabled to build a methodology for the processing and the joint inversion of several EO. Each EO has a specificity that enable to obtain precision on the

deformation. This study enabled to better see what impact each data set has on the model, how and in which condition to use each type and especially how we can join them to use their strengths and overpass their limitations. Information concerning the geometry of the fault was obtained as well as the slip distribution. The quantity of stress released by the rupture could be analysed. This technique could be used for the study of several other events or for earthquake situated in area not covered by GNSS or where InSAR is not coherent over the entire area. Concerning the postseismic study, using a forward approach, based on coseismic stress and previous studies defining the rheology of the lithosphere, enabled to detect modification in ground displacement over the 20 years, analyse the strain rate and determine that the interseismic phase has started. Also, this entire study combining phases of the earthquake cycle, allowed us to see that the Chi-Chi earthquake and its aftershocks transferred stress to neighbouring faults that should be closely monitored such as the Luliao fault. Longer time series will be needed to detect more precisely the locking of the entire Chelungpu fault.

Chapter 7

RGS-IBG Hong Kong research grant 2019 Report

Seismic Hazard Assessment of the Chelungpu Fault and its Surroundings Since the 1999 Chi-Chi Earthquake

Thanks to RGS-IBG Hong Kong research grant 2019 (`www.rgs.org/in-the-field/in-the-field-grants/students/phd/hong-kong-research-grant/`) that I obtained, I had the chance to organise a fieldtrip to Taiwan for 2 weeks in December 2019. This project was composed of two main parts: a fieldtrip and, the analysis of the work done so far in the PhD and discuss the remaining to do with experts of Taiwan Geology and Geomatics.
First, I will present the team with which I spent these two weeks, knowing that the inviting professor was Pr. Jyr-Ching Hu.

Several times a year Taiwan is struck by damaging earthquakes. A similar monitoring as the one in California should be done to precisely monitor the faults and deformation of the island. It was obviously not a discovery to see the impact of the earthquake on the ground and the damages on buildings but being able to see with our own eyes the consequences, how the land got modified in a few seconds/minutes, how many buildings got damaged/destroyed and how much the population is aware of this event and still shocked 20 years after is motivating us to keep working in this field in order to help preventing the loss of human life and human structures. As my work is only based on satellite data to study the deformation of the ground, the main goal of going on the field is to understand the geology in order to more precisely define the structure of the model and assess the deformation.

The field trip along the Chelungpu fault was about the observation of the deformation still visible of the ground in the company of Taiwan experts. Several sites were visited: along the main fault, uplift from 1 m (Figure 7.6) in the south part to 15 m in the north, complex area where the fault is curved towards east, were

Figure 7.1: Pr Hu and others researchers met during Taiwan stay.

Figure 7.2: (left) Pr Hu and his students planning the field trip at National Taiwan University. (right) Itinerary of the field trip (source Google Map).

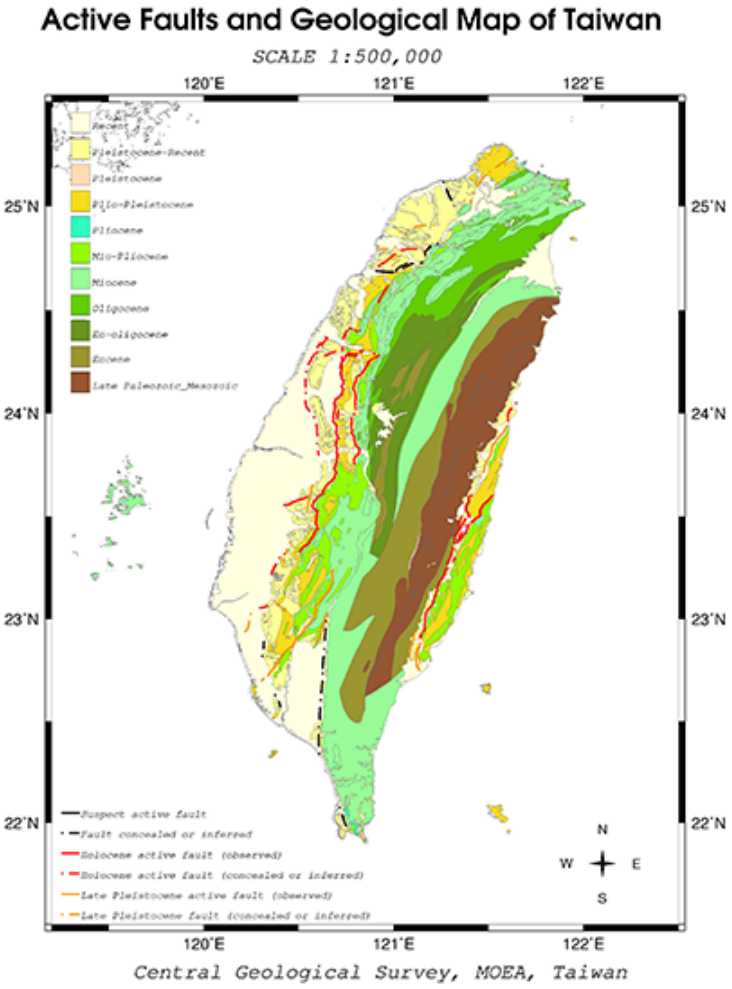

Figure 7.3: Active Faults and Geological map of Taiwan.

observed ; a trench realised 3 years after the earthquake to observe the geological structures moved by the event (Figure 7.8), visit of three museums explaining in details the event and preserving some sites, one being the Kwang-Fu Junior High School that got partially destroyed by the event (Figure 7.5). We went in the area where a large landslide that was triggered by this event happened and still showing the chaotic ground and a slanted house, and several others sites (Figures 7.4 & 7.6) as well as measurements (GNSS, levelling and benchmarks) sites (Figure 7.7).

The main goal of this project was to manage to get a better understanding of the interaction between the different segments of faults, understand the geology and tectonics of the area and restrain the model built using only earth observations. Visualising the main deformation areas in regards with the position of cities and main constructions give a better determination of the areas to focus on to prevent

Figure 7.4: (left) Tilted tower moved by the event. (middle) Over the Dajia river, the Pifeng bridge got broken and the river bed got moved up of 6 m creating a waterfall (not visible anymore). (right) The northern end of the Shihgang dam truncated from the rest of the dam, the main part was uplifted by 9.8 m.

Figure 7.5: A school building damaged and the athletic field uplifted by 2 m in Kwang-Fu Junior High School.

damages and losses during a next similar event. Also, until now the study of the earthquake has been mainly focused on the main segment of the Chelungpu fault. However, by analysing the geological map and the observations got on the field, several neighboring faults were triggered by this event around the Chelungpu fault and creating large events sometimes after the mainshock, more focus should be on the neighboring area of the fault and not only the fault itself (All pictures presented before were taken by myself during the trip).

The second part of the time in Taiwan was in majority composed of meetings with professors at NTU, CCU and Academia Sinica to discuss the preliminary results obtained in my PhD and which work would be better to focus on until the end of it.

Regarding the work that is lacking knowledge, the north part has been quite closely

Figure 7.6: (left) Railway torned and uplifted. (middle) Parallel segment in the north showing 1 m uplift. (right) Fault scarp showing geological structures.

Figure 7.7: (left) Two benchmarks and a levelling reference. (middle) A continuous GNSS station in Wuguang Elementary School. (right) Continuous GNSS station.

studied in comparison with the south part. The link between the Tachienshan and Chelungpu faults should be modelled and the faults triggered, such as the Luliao fault, properly understood. Getting more understanding about the way the earthquake happened and its consequences is a priority to understand this area. Looking at the deformation since the earthquake happened as well as the fault interactions are essential to try to understand where and in approximately how much time the next event will happen. Before the Chi-Chi earthquake, the main attention was on the south west part of Taiwan, where the main deformation and some important faults are present. An understanding of the impact of this deformation and the state

Figure 7.8: Chushan Fault trench dug in 2002 showing the geological structures linked to the earthquake.

of this area is essential. Also, during the event, twice more energy was released in the north part than in the south while the south, geologically speaking, is older. Finally, collaborations with experts of the field started during this two-week project. For instance with Mong-Han Huang to follow up his work on an update of the geometry of the Chelungpu fault using Poly3d.

Bibliography

Akaike, H. 1973 Information theory and an extension of the maximum likelihood principle. *In Second Int. Symp. Info. Theory, Ed. B.N. Petrox and F. Caski* pp. 267–281.

Angelier, J., Lee, J.-C., Chu, H.-T., Hu, J.-C., Lu, C.-Y., Chan, Y.-C., Tin-Jai, L., Font, Y., Deffontaines, B. & Yi-Ben, T. 2001 Le séisme de Chi-Chi (1999) et sa place dans l'orogène de Taiwan. *Comptes Rendus de l'Academie de Sciences - Serie IIa: Sciences de la Terre et des Planetes* **333**, 5–21.

Ayoub, F., Leprince, S. & Avouac, J.-P. 2009 Co-registration and correlation of aerial photographs for ground deformation measurements. *ISPRS Journal of Photogrammetry and Remote Sensing* **64**, 551–560.

Barbot, S. & Moore, J. 2019 Lithosphere dynamics .

Bell, M. A. 2013 The earthquake cycle of the manyi fault, tibet. PhD thesis, University of Oxford.

Berardino, P., Fornaro, G., Lanari, R. & Sansosti, E. 2002 A new algorithm for surface deformation monitoring based on small baseline differential SAR interferograms. *IEEE Transactions on Geoscience and Remote Sensing* **40** (11), 2375–2383.

Bhattacharya, A., Arora, M. K. & Sharma, M. 2012 Usefulness of synthetic aperture radar (SAR) interferometry for digital elevation model (DEM) generation and estimation of land surface displacement in jharia coal field area. *Geocarto International* **27** (1), 57–77.

Biggs, J., Wright, T., Lu, Z. & Parsons, B. 2007 Multi-interferogram method for measuring interseismic deformation: Denali Fault, Alaska. *Geophysical Journal International* **170** (3), 1165–1179.

Boehm, J., Niell, A., Tregoning, P. & Schuh, H. 2006 Global mapping function (GMF): A new empirical mapping function based on numerical weather model data. *Geophysical Research Letters* **33** (7).

Bos, M. S. & Fernandes, R. M. S. 2019 Hector user manual version 1.7.2 .

Bos, M. S., Fernandes, R. M. S., Williams, S. D. P. & Bastos, L. 2013 Fast error analysis of continuous gnss observations with missing data. *Journal of Geodesy* **87**, 351–360.

Bürgmann, R. & Dresen, G. 2008 Rheology of the lower crust and upper mantle: Evidence from rock mechanics, geodesy, and field observations. *Annual Review of Earth and Planetary Sciences* **36**, 531–567.

Bürgmann, R., Ergintav, S., Segall, P., Hearn, E., McClusky, S., Reilinger, R., Woith, H. & Zschau, J. 2002 Time-dependent distributed afterslip on and deep below the İzmit earthquake rupture. *Bulletin of the Seismological Society of America* **92**, 126–137.

Bürgmann, R. 2018 The geophysics, geology and mechanics of slow fault slip. *Earth and Planetary Science Letters* **495**, 112–134.

Chamot-Rooke, N. & Le Pichon, X. 1999 GPS determined eastward sundaland motion with respect to Eurasia confirmed by earthquakes slip vectors at Sunda and Philippine trenches. *Earth and Planetary Science Letters* **173**, 439–455.

Chan, C.-H. & Stein, R. S. 2009 Stress evolution following the 1999 Chi-Chi, Taiwan, earthquake: Consequences for afterslip, relaxation, aftershocks and departures from Omori decay. *Geophysical Journal International* **177** (1), 179–192.

Chen, C. W. & Zebker, H. A. 2000 Network approaches to two-dimensional phase unwrapping: intractability and two new algorithms. *Journal of the Optical Society of America* **17**, 401–414.

Chen, C. W. & Zebker, H. A. 2001 Two-dimensional phase unwrapping with use of statistical models for cost functions in nonlinear optimization. *Journal of the Optical Society of America* **18**, 338–351.

Chen, C. W. & Zebker, H. A. 2002 Phase unwrapping for large SAR interferograms: Statistical segmentation and generalized network models. *IEEE Transactions on Geoscience and Remote Sensing* **40**, 1709–1719.

Chen, K., Yang, M., Huang, Y.-T., Ching, K.-E. & Rau, R.-J. 2011 Vertical displacement rate field of Taiwan from geodetic levelling data 2000-2008. *Survey review* (43:321), 296–302.

Chen, S., Wu, Y., Hsu, Y. & Chan, Y. 2017 Current crustal deformation of the Taiwan orogen reassessed by cGPS strain-rate estimation and focal mechanism stress inversion. *Geophysical journal international* **210** (3), 1472–1473.

Ching, K.-E., Hsieh, M.-L., Johnson, K., Chen, K., Rau, R.-J. & Yang, M. 2011 Modern vertical deformation rates and mountain building in Taiwan from precise leveling and continuous GPS observations, 2000–2008. *Journal of Geophysical research* **116** (B08406).

Chlieh, M., De Chabalier, J. B., Ruegg, J. C., Armijo, R., Dmowska, R., Campos, J. & Feigl, K. L. 2004 Crustal deformation and fault slip during the seismic cycle in the North Chile subduction zone, from GPS and InSAR observations. *Geophysical Journal International* **158** (2), 695–711.

Cornwall, M.-G., Lewes & Sussex, E. 2008 Where on Earth Am I?: Global Navigation Satellite Systems. *Sage journals* **Measurement and Control:41**, 174–178.

Crosetto, M., Monserrat, O., Cuevas-González, M., Devanthéry, N. & Crippa, B. 2016 Persistent scatterer interferometry: A review. *ISPRS Journal of Photogrammetry and Remote Sensing* **115**, 78 – 89.

Ding, X., Li, Z., Zhu, J., Feng, G. & Long, J. 2008 Atmospheric effects on InSAR measurements and their mitigation. *Sensors* **8**, 5426–5448.

Dominguez, S., Avouac, J.-P. & Michel, R. 2003 Horizontal coseismic deformation of the 1999 Chi-Chi earthquake measured from SPOT satellite images: Implications for the seismic cycle along the western foothills of central Taiwan. *Journal of geophysical research* **108** (B2).

El-Rabbany, A. 2002 *Introduction to GPS: the Global Positioning System*. Artech House Inc.

Elliott, J., de Michele, M. & Gupta, H. K. 2020 Earthobservation for crustal tectonics and earthquake hazards. *Surveys in Geophysics* **41**, 1355–1389.

Feng, W. & Li, Z. 2010 A novel hybrid PSO/simplex algorithm for determining earthquake source parameters using InSAR observations. *Diqiu Wulixue Jinzhan [Progress in Geophysics]* **25**, 1550–1559.

Feng, W., Li, Z., Elliott, J., Fukushima, Y., Hoey, T., Singleton, A., Cook, R. & Xu, Z. 2013 The 2011 Mw 6.8 Burma earthquake: fault constraints provided by multiple SAR techniques. *Geophysical Journal International* **195** (1), 650–660.

Ferretti, A., Monti-Guarnieri, A., Prati, C. & Rocca, F. 2007 InSAR principles: Guidelines for SAR interferometry processing and interpretation. *ESA publications* .

Ferretti, A., Prati, C. & Rocca, F. 2000 Nonlinear subsidence rate estimation using permanent scatterers in differential SAR interferometry. *IEEE Transactions on Geoscience and Remote Sensing* **38** (5), 2202–2212.

Ferretti, A., Prati, C. & Rocca, F. 2001 Permanent scatterers in SAR interferometry. *IEEE Transactions on Geoscience and Remote Sensing* **39** (1), 8–20.

Fialko, Y. 2004 Evidence of fluid-filled upper crust from observations of postseismic deformation due to the 1992 Mw7.3 Landers earthquake. *Journal of Geophysical Research: Solid Earth* **109** (B8).

Fialko, Y., Simons, M. & Agnew, D. 2001 The complete (3-d) surface displacement field in the epicentral area of the 1999 Mw7.1 hector mine earthquake, california, from space geodetic observations. *Geophysical Research Letters* **28** (16), 3063–3066.

Funning, G., Fukahata, Y., Yagi, Y. & Parsons, B. 2014 A method for the joint inversion of geodetic and seismic waveform data using ABIC: application to the 1997 Manyi, Tibet, earthquake. *Geophysical Journal International* **196**, 1564–1579.

Goldstein, R. & Werner, C. 1998 Radar interferogram filtering for geophysical applications. *Geophysical Research Letters* **25**, 4035–4038.

Gourmelen, N., Amelung, F. & Lanari, R. 2010 Interferometric synthetic aperture radar–GPS integration: Interseismic strain accumulation across the Hunter mountain fault in the eastern california shear zone. *Journal of Geophysical Research: Solid Earth* **115** (B9).

Graham, S. E., DeMets, C., Cabral-Cano, E., Kostoglodov, V., Walpersdorf, A., Cotte, N., Brudzinski, M., McCaffrey, R. & Salazar-Tlaczani, L. 2014 GPS constraints on the Mw = 7.5 Ometepec earthquake sequence, southern Mexico: coseismic and post-seismic deformation. *Geophysical Journal International* **199** (1), 200–218.

Hanssen, R. F. 2002 *Radar Interferometry, Data Interpretation and Error Analysis*, , vol. 2: Remote sensing and Digital Image Processing.

Hsu, W.-C., Chang, H.-C., Chang, K.-T., Lin, E.-K., Liu, J.-K. & Liou, Y.-A. 2015 Observing land subsidence and revealing the factors that influence it using a multi-sensor approach in Yunlin County, Taiwan. *Remote Sensing* **7** (6), 8202–8223.

Hsu, Y.-J., Avouac, J.-P., Yu, S.-B., Chang, C.-H., Wu, Y.-M. & Woessner, J. 2009 Spatio-temporal slip, and stress level on the faults within the western foothills of Taiwan: Implications for fault frictional properties. *Pure appl. geophys.* **166**, 1853–1884.

Hsu, Y.-J., Bechor, N., Segall, P., Yu, S.-B., Kuo, L.-C. & Ma, K.-F. 2002 Rapid afterslip following the 1999 Chi-Chi, Taiwan earthquake. *Geophysical Research Letters* **29** (16), 1–4.

Hsu, Y.-J., Segall, P., Yu, S.-B., Kuo, L.-C. & Williams, C. A. 2007 Temporal and spatial variations of post-seismic deformation following the 1999 Chi-Chi, Taiwan earthquake. *Geophysical Journal* **169**, 367–379.

Huang, C., Chan, Y.-C., Hu, J.-C., Angelier, J. & Lee, J.-C. 2008 Detailed surface co-seismic displacement of the 1999 Chi-Chi earthquake in western Taiwan and implication of fault geometry in the shallow subsurface. *Journal of Structural Geology* **30**, 1167–1176.

Huang, M.-H., Bürgmann, R. & Hu, J.-C. 2016 Fifteen years of surface deformation in western Taiwan: Insight from SAR interferometry. *Tectonophysics* **692**, 252–264, geodynamics and Environment in East Asia, GEEA 2014.

Hung, W.-C., Hwang, C., Liou, J.-C., Lin, Y.-S. & Yang, H.-L. 2012 Modeling aquifer-system compaction and predicting land subsidence in central Taiwan. *Engineering Geology* **147-148**, 78 – 90.

Hussain, E., Wright, T., Walters, R., Bekaert, D. P. S., Lloyd, R. & Hooper, A. 2018 Constant strain accumulation rate between major earthquakes on the north anatolian fault. *Nature Communications* (1392).

Ji, C., Helmberger, D.-V., Wald, D.-J. & Ma, K.-F. 2003 Slip history and dynamic implications of the 1999 Chi-Chi, Taiwan, earthquake. *Journal of Geophysical Research: Solid Earth* **108**.

Jiang, J., Bock, Y. & Klein, E. 2021 Coevolving early afterslip and aftershock signatures of a san andreas fault rupture. *Science Advances* **7** (15).

Johnson, K. & Segall, P. 2004 Imaging the ramp–decollement geometry of the Chelungpu fault using coseismic GPS displacements from the 1999 Chi-Chi, Taiwan earthquake. *Tectonophysics* **378**, 123– 139.

Johnson, K. M., Hsu, Y.-J., Segall, P. & Yu, S.-B. 2001 Fault geometry and slip distribution of the 1999 Chi-Chi Taiwan earthquake imaged from inversion of GPS data. *Geophysical research letters* **28** (11), 2285–2288.

Jolivet, R., Grandin, R., Lasserre, C., Doin, M.-P. & Peltzer, G. 2011 Systematic InSAR tropospheric phase delay corrections from global meteorological reanalysis data. *Geophysical Research Letters, American Geophysical Union* **38**, L17311.

Jonsson, S., Zebker, H., Segall, P. & Amelung, F. 2002 Fault slip distribution of the 1999 Mw 7.1 Hector Mine, California, Earthquake, estimated from satellite radar and GPS measurements. *Bulletin of the Seismological Society of America* **92** (4), 1377–1389.

Kelley, M. 2009 *The Earth's Ionosphere: Plasma physics and electrodynamics*, , vol. Second Edition. Academic Press.

Klein, E., Fleitout, L., Vigny, C. & Garaud, J. 2016 Afterslip and viscoelastic relaxation model inferred from the large-scale post-seismic deformation following the 2010 Mw 8.8 Maule earthquake (Chile). *Geophysical Journal International* **205** (3), 1455–1472.

Kohlstedt, D. & Hansen, L. 2015 2.18 - constitutive equations, rheological behavior, and viscosity of rocks. In *Treatise on Geophysics (Second Edition)*, Second edition edn. (ed. G. Schubert), pp. 441–472. Oxford: Elsevier.

Kovalevsky, J. & Mueller, I. 1981 *Reference Coordinate Systems for Earth Dynamics*, , vol. 86.

Kuo, Y., Ayoub, F., Leprince, S., Chen, Y., Avouac, J., Shyu, J., Lai, K. & Kuo, Y. 2014 Coseismic thrusting and folding in the 1999 Mw 7.6 Chi-Chi earthquake: a high-resolution approach by aerial photos taken from Tsaotun, central Taiwan. *Journal of Geophysical research – solid earth* **119** (1), 645–660.

Lee, J.-C. & Chan, Y.-C. 2007 Structure of the 1999 Chi-Chi earthquake rupture and interaction of thrust faults in the active fold belt of western Taiwan. *Journal of Asian Earth Sciences* **31**, 226–239.

Lee, J.-C., Chen, Y.-G., Sieh, K., Mueller, K., Chen, W.-S., Chu, H.-T., Chan, Y.-C., Rubin, C. & Yeats, R. 2001 A vertical exposure of the 1999 surface rupture of the chelungpu fault at Wufeng, western Taiwan: Structural and paleoseismic implications for an active thrust fault. *Bulletin of the Seismological Society of America* **91**, 914–929.

Lee, T. T.-Y., Chan, C.-H., Shyu, J. B. H., Wu, Y.-M. & Huang, H.-H. 2014 Induced transtensional earthquakes after the 1999 Chi-Chi earthquake in the compressional collision belt of western Taiwan. *Geophysical Journal International* **200** (1), 638–651.

Lee, Y.-H. & Y-X., S. 2011 Coseismic displacement, bilateral rupture, and structural characteristics at the southern end of the 1999 Chi-Chi earthquake rupture, central Taiwan. *Journal of Geophysical research* **116**.

Lee, Y. R., Cheng, C. T., Shao, K. S., Chuang, Y. R., Hu, J. C., Lai, T. H. & Lu, S. T. 2016 Earthquake probability assessment for the active faults in central Taiwan: A case study. *Terr. Atmos. Ocean. Sci.* **27**, 341–357.

Leprince, S., Barbot, S., Ayoub, F. & Avouac, J. 2007 Automatic and precise ortho-rectification, coregistration, and subpixel correlation of satellite images, application to ground deformation measurements. *IEEE Transactions. Goesciences. Rmote sensing* **45** (6), 1529–1558.

Li, Z., Fielding, E. J. & Cross, P. 2009 Integration of InSAR time-series analysis and water-vapor correction for mapping postseismic motion after the 2003 bam (iran) earthquake. *IEEE Transactions on Geoscience and Remote Sensing* **47** (9), 3220–3230.

Liao, B.-Y., Sheu, T.-W., Yeh, Y.-T., Huang, H.-C. & Yang, L.-S. 2013 A rupture model for the 1999 Chi-Chi earthquake from inversion of teleseismic data using the hybrid homomorphic deconvolution method. *Pure and Applied Geophysics* **170**, 391–407.

Liao, W.-T., Tseng, K.-H., Lee, I.-T., Liibusk, A., Lee, J.-C., Liu, J., Chang, C.-P. & Lin, Y.-C. 2020 Sentinel-1 interferometry with ionospheric correction from global and local tec maps for land displacement detection in taiwan. *Advances in Space Research* **65**, 1447–1465.

Lin, J. & Stein, R. 2004 Stress triggering in thrust and subduction earthquakes, and stress interaction between the southern san andreas and nearby thrust and strike-slip faults. *Journal of Geophysical Research* **109**.

Liu, G., Ding, X., Li, Z., Li, Z., Chen, Y. & Yu, S. 2004 Pre- and co-seismic ground deformations of the 1999 Chi-Chi, Taiwan earthquake, measured with SAR interferometry. *Computers & Geosciences* **30** (4), 333–343.

Loevenbruck, A., Cattin, R., Le Pichon, X., Courty, M. & Yu, S. 2001 Seismic cycle in Taiwan derived from GPS measurements. *Comptes rendus de l'Académie des Sciences serie II, Fascicule A-Sciences de la terre et des planètes* **333**, 57–64.

Ma, K.-F., Mori, J., Lee, S.-J. & Yu, S.-B. 2001 Spatial and temporal distribution of slip for the 1999 Chi-Chi, Taiwan, earthquake. *Bulletin of the Seismological Society of America* pp. 1069–1087.

Maerten, F., Maerten, L. & Pollard, D. 2014 iBem3D, a three-dimensional iterative boundary element method using angular dislocations for modeling geologic structures. *Computers Geosciences* **72**, 1–17.

Massonnet, D. & Feigl, K. 1998 Radar interferometry and its application to changes in the earth's surface. *Rev. Geophys.* **36**, 441–500.

Michel, R., Avouac, J. & Taboury, J. 1999 Measuring near field coseismic displacements from SAR images: Application to the Landers earthquake. *Geophysical research letters* **26** (19), 3017–3020.

Moore, J. D. & Parsons, B. 2015 Scaling of viscous shear zones with depth-dependent viscosity and power-law stress–strain-rate dependence. *Geophysical Journal International* **202** (1), 242–260.

Moore, J. D. P., Barbot, S., Lambert, V., Tang, C. H., Peng, D., Masuti, S. S., Dauwels, J., Wu, S., Yu, H., Hsu, Y. J., Nanjundiah, P., Wei, S., Lindsey, E., Feng, L., Shibazaki, B. & Wang, T. 2016 Kinematic inversion of postseismic deformation following the 2016 Mw 7.0 Kumamoto earthquake for the distribution of brittle and ductile crustal processes. In *AGU Fall Meeting Abstracts*, , vol. 2016, pp. S52C–08.

Mora, O., Lanari, R., Mallorqui, J. J., Berardino, P. & Sansosti, E. 2002 A new algorithm for monitoring localized deformation phenomena based on small baseline differential SAR interferograms. In *IEEE International Geoscience and Remote Sensing Symposium*, , vol. 2, pp. 1237–1239 vol.2.

Morishita, Y., Lazecký, M., Wright, T., Weiss, J. R., Elliott, J. R. & Hooper, A. 2020 LiCSBAS: An open-source InSAR time series analysis package integrated with the LiCSAR automated Sentinel-1 InSAR processor. *Remote. Sens.* **12**, 424.

Muto, J., Moore, J. D. P., Barbot, S., Iinuma, T., Ohta, Y. & Iwamori, H. 2019 Coupled afterslip and transient mantle flow after the 2011 tohoku earthquake. *Science Advances* **5** (9).

Ng, S. M., Angelier, J. & Chang, C.-P. 2009 Earthquake cycle in Western Taiwan: Insights from historical seismicity. *Geophysical Journal International* **178** (2), 753–774.

Okada, Y. 1985 Surface deformation due to shear and tensile faults in a half-space. *Bulletin of the seismological society of America* **75** (4), 1135–1154.

Okada, Y. 1992 Internal deformation due to shear and tensile faults in a half-space. *Bulletin of the seismological society of America* **82** (2), 1018–1040.

Pathier, E., Fruneau, B., Deffontaines, B., Angelier, J., Chang, C., Yu, S. & Lee, C. 2003 Coseismic displacements of the footwall of the Chelungpu fault caused by the 1999, Taiwan, Chi-Chi earthquake from InSAR and GPS data. *Earth and planetary science letters* **212** (1-2), 73–88.

Peyret, M., Dominguez, S., Cattin, R., Champenois, J., Leroy, M. & Zajac, A. 2011 Present-day interseismic surface deformation along the longitudinal valley, eastern Taiwan, from a PS-InSAR analysis of the ERS satellite archives. *Journal of Geophysical Research: Solid Earth* **116** (B3).

Pierrot-Deseilligny, M. & Paparoditis, N. 2006 A multiresolution and optimization-based image matching approach: An application to surface reconstruction from SPOT 5-HRS stereo imagery.

Pollitz, F. F., Bürgmann, R. & Banerjee, P. 2006 Post-seismic relaxation following the great 2004 sumatra-andaman earthquake on a compressible self-gravitating earth. *Geophysical Journal International* **167** (1), 397–420.

Qiu, Q., Moore, J., Barbot, S., Feng, L. & Hill, E. 2018 Transient rheology of the sumatran mantle wedge revealed by a decade of great earthquakes. *Nature Communications* **9**.

Reid, H. 1910 *The Mechanics of the Earthquake, The California Earthquake of April 18, 1906, Report of the State Investigation Commission*, , vol. 2. Carnegie Institution of Washington, Washington, D.C.

Reiter, L. 1991 Earthquake hazard analysis: Issues and insights.

Remy, D., Perfettini, H., Cotte, N., Avouac, J. P., Chlieh, M., Bondoux, F., Sladen, A., Tavera, H. & Socquet, A. 2016 Postseismic relocking of the subduction megathrust following the 2007 pisco, peru, earthquake. *Journal of Geophysical Research: Solid Earth* **121** (5), 3978–3995.

Roger, M., Li, Z., Clarke, P., Song, C., Hu, J.-C., Feng, W. & Yi, L. 2020 Joint inversion of geodetic observations and relative weighting — the 1999 Mw 7.6 Chi-Chi earthquake revisited. *Remote Sensing* **12** (19).

Roselli, P., Marzocchi, W., Mariucci, M. T. & Montone, P. 2017 Earthquake focal mechanism forecasting in Italy for PSHA purposes. *Geophysical Journal International* **212** (1), 491–508.

Rosu, A.-M., Pierrot-Deseilligny, M., Delorme, A., Binet, R. & Klinger, Y. 2015 Measurement of ground displacement from optical satellite image correlation using the free open-source software MicMac. *ISPRS Journal of Photogrammetry and Remote Sensing* **100**, 48–59, high-Resolution Earth Imaging for Geospatial Information.

Rousset, B., Barbot, S., Avouac, J.-P. & Hsu, Y.-J. 2012 Postseismic deformation following the 1999 Chi-Chi earthquake, Taiwan: Implication for lower-crust rheology. *Journal of Geophysical Research: Solid Earth* **117** (B12).

Ryder, I., Wang, H., Bie, L. & Rietbrock, A. 2014 Geodetic imaging of late postseismic lower crustal flow in Tibet. *Earth and Planetary Science Letters* **404**, 136–143.

Scholz, C. 1990 The mechanics of earthquakes and faulting.

Segall, P. 2010 *Earthquake and Volcano Deformation*, stu - student edition edn. Princeton University Press.

Sheu, S.-Y. & Shieh, C.-F. 2004 Viscoelastic-afterslip concurrence: a possible mechanism in the early post-seismic deformation of the Mw 7.6, 1999 Chi-Chi (Taiwan) earthquake. *Geophysical Journal* **159**, 1112–1124.

Shyu, J. B. H., Sieh, K., Chen, Y.-G. & Liu, C.-S. 2005 Neotectonic architecture of Taiwan and its implications for future large earthquakes. *Journal of Geophysical Research B: Solid Earth* **110**, 1–33.

Suppe, J. 1984 Kinematics of arc-continent collision, flipping of subduction, and back-arc spreading near Taiwan. *Mem. Geol. Soc. China* pp. 21–34.

Takada, Y., Sagiya, T. & Nishimura, T. 2018 Interseismic crustal deformation in and around the atotsugawa fault system, central japan, detected by InSAR and gnss. *Earth Planets Space* **70**.

Tang, C.-H., Hsu, Y.-J., Barbot, S., Moore, J. D. P. & Chang, W.-L. 2019 Lower-crustal rheology and thermal gradient in the Taiwan orogenic belt illuminated by the 1999 Chi-Chi earthquake. *Science Advances* **5** (2).

Teunissen, P. & Montenbruck, O. 2017 *Springer Handbook of Global Navigation Satellite Systems*. Springer.

Toda, S., Stein, R. S.and Richards-Dinger, K. & Bozkurt, S. 2005 Forecasting the evolution of seismicity in southern California: Animations built on earthquake stress transfer. *Journal of Geophysical Research* **110**.

Tong, X., Sandwell, D. T. & Smith-Konter, B. 2013 High-resolution interseismic velocity data along the san andreas fault from GPS and InSAR. *Journal of Geophysical Research: Solid Earth* **118** (1), 369–389.

Tung, H. & Hu, J.-C. 2012 Assessments of serious anthropogenic land subsidence in Yunlin county of central Taiwan from 1996 to 1999 by persistent scatterers InSAR. *Tectonophysics* **578**, 126 – 135, geodynamics and Environment in East Asia.

Van Puymbroeck, N., Michel, R., Binet, R., Avouac, J. & Taboury, J. 2000 Measuring earthquakes from optical satellite images. *Applied Optics* **39** (20), 3486–3494.

Wang, J., Chen, K., Leu, P. & Chang, C. 2016 Studies on aftershocks in Taiwan: A review. *Terrestrial atmospheric and oceanic sciences* **27** (6), 769–789.

Wang, J.-H. 2016 Studies of earthquake energies in Taiwan: A review. *Terrestrial atmospheric and oceanic sciences* **27** (1), 1–19.

Wang, K. & Fialko, Y. 2014 Space geodetic observations and models of post-seismic deformation due to the 2005m7.6 kashmir (pakistan) earthquake. *Journal of Geophysical Research: Solid Earth* **119** (9), 7306–7318.

Wang, K., Hu, Y. & He, J. 2012 Deformation cycles of subduction earthquakes in a viscoelastic earth. *Nature* **484**, 327–332.

Wegmüller, U., Werner, C., Strozzi, T., Wiesmann, A., Frey, O. & Santoro, M. 2016 Sentinel-1 support in the gamma software. *rocedia Comput. Sci.* **100**, 1305–1312.

Werner, C., Wegmüller, U., Strozzi, T. & Wiesmann, A. 2000 GAMMA SAR and interferometric processing software. *Proceedings of the ERS-Envisat Symposium, Gothenburg, Sweden* .

Wright, T., Parsons, B. & Fielding, E. 2001 Measurement of interseismic strain accumulation across the north anatolian fault by satellite radar interferometry. *Geophysical Research Letters* **28** (10), 2117–2120.

Yabuki, T. & Matu'ura, M. 1992 Geodetic data inversion using a bayesian information criterion for spatial distribution of fault slip. *Geophys. J. Int.* **109**, 363–375.

Yang, Y.-J., Hwang, C., Hung, W.-C., Fuhrmann, T., Chen, Y.-A. & Wei, S.-H. 2019 Surface deformation from Sentinel-1A InSAR: Relation to seasonal groundwater extraction and rainfall in central Taiwan. *Remote Sensing* **11** (23).

Yen, J. Y., Chen, K. S., Chang, C. P. & Ng, S. M. 2006 Deformation and "deformation quiescence" prior to the Chi-Chi earthquake evidenced by DInSAR and groundwater records during 1995-2002 in central Taiwan. *Earth, Planets and Space* **58**, 805–813.

Yi, L., Xu, C., Wen, Y., Zhang, X. & Jiang, G. 2018 Rupture process of the 2016 Mw 7.8 Ecuador earthquake from joint inversion of InSAR data and teleseismic P waveforms. *Tectonophysics* **722**, 163–174.

Yi, L., Xu, C., Zhang, X., Wen, Y., Jiang, G., Li, M. & Wang, Y. 2017 Joint inversion of GPS, InSAR and teleseismic data sets for the rupture process of the 2015 Gorkha, Nepal, earthquake using a generalized ABIC method. *Journal of Asian Earth Sciences* **148**, 121 – 130.

Yu, C., Li, Z. & Penna, N. 2017*a* Interferometric synthetic aperture radar atmospheric correction using a GPS-based iterative tropospheric decomposition model. *Remote Sensing of Environment* **204**, 109–121.

Yu, C., Li, Z. & Penna, N. 2020 Triggered afterslip on the southern Hikurangi subduction interface following the 2016 Kaikōura earthquake from InSAR time series with atmospheric corrections. *Remote Sensing of Environment* **251**, 112097.

Yu, C., Li, Z., Penna, N. T. & Crippa, P. 2017*b* Generic atmospheric correction model for interferometric synthetic aperture radar observations. *Journal of Geophysical Research: Solid Earth* **123** (10), 9202–9222.

Yu, C., Penna, N. & Li, Z. 2017*c* Generation of real-time mode high-resolution water vapor fields from GPS observations. *Journal of Geophysical Research: Atmospheres* **122**, 2008–2025.

Yu, S.-B., Chen, H.-Y. & Kuo, L.-C. 1997 Velocity field of GPS stations in the Taiwan area. *Tectonophysics* **274**, 41–59.

Yu, S.-B., Kuo, L.-C., Hsu, Y.-J., Su, H.-H., Liu, C.-C., Hou, C.-S., Lee, J.-F., Lai, T.-C., Liu, C.-C., Liu, C.-L., Tseng, T.-F., Tsai, C.-S. & Shin, T.-C. 2001 Preseismic deformation and coseismic displacements associated with the 1999 Chi-Chi, Taiwan, earthquake. *Bulletin of the Seismological Society of America* **91**, 995–1012.

Yu, S.-B., Kuo, L.-C., Punongbayan, R. S. & Ramos, E. G. 1999 GPS observation of crustal deformation in the Taiwan-Luzon region. *Geophysical research letters* **26**, 923–926.

Yue, L.-F., Suppe, J. & Hung, J.-H. 2005 Structural geology of a classic thrust belt earthquake: the 1999 Chi-Chi earthquake Taiwan (Mw=7.6). *Journal of Structural Geology* **27** (11), 2058–2083.

Zhang, L., Wu, J.-C., Ge, L.-L., Ding, X.-L. & Chen, Y.-L. 2008 Determining fault slip distribution of the Chi-Chi Taiwan earthquake with GPS and InSAR data using triangular dislocation elements. *Journal of Geodynamics* **45**, 163–168.